

Jahresbericht des Physikalischen Instituts

Annual Report

2009

PHYSIKALISCHES INSTITUT

Prof. Dr. Hilbert v. Löhneysen

Prof. Dr. Alexey Ustinov

Prof. Dr. Georg Weiß

Prof. Dr. Wulf Wulfhekel

Apl. Prof. Dr. Gernot Goll

Apl. Prof. Dr. Bernd Pilawa

Editors: G. Fischer, W. Wulfhekel



Dear Colleagues and Friends,

with the Annual Report 2009 of our Institute, we present an overview over our last year's research activities ranging from fundamental properties of solids to more materials-related aspects. Our research interests cover electronic transport in nano-structured metallic systems, superconductivity, quantum coherence in solids, magnetism, physics of strongly correlated electrons, metal-insulator transitions, atomic dynamics of disordered solids, and chemical physics. This report cannot cover all our activities, but you are welcome to contact us for further information.

The year 2009 brought many changes to our university. Universität Karlsruhe (TH) and Forschungszentrum Karlsruhe (FZK) fused to form the Karlsruhe Institute of Technology (KIT) which became a legal entity as of October 1, 2009. This fusion brought a lot of new impetus to both institutions and will lead to stronger collaborative research efforts and better visibility of the research carried out in Karlsruhe. As with all change, this radical change has caused some friction. Luckily, this did not affect matters of research but occurred mostly on the administrative level of KIT. Hopefully, this friction will disappear in the near future so that there the positive aspects will dominate as well. Hilbert v. Löhneysen and Wulf Wulfhekel were elected as the spokespersons of the KIT Competence Field Condensed Matter Physics. The already strong links between our Institute and the Institute for Solid State Physics (IFP) of Campus North (the former FZK), established long before KIT came into being, as manifested for the last decades not only by regular joint seminars but also by a large number of joint Ph.D. students, have been strengthened further.

In 2009, Gernot Goll was awarded the title of "außerplanmäßiger Professor" in recognition of his achievements in low-temperature solid state physics and Regina Hoffmann-Vogel was awarded one of the few prestigious ERC Young Investigator Grants of the European Union.

The year 2009 also brought the International Conference on Magnetism (ICM 2009) to Karlsruhe. Starting in 2003 when the bid to host ICM 2009 was given to Karlsruhe, the preparation of this large-scale event was shaped into reality step by step. Hilbert v. Löhneysen acted as chair of the conference and many of our senior scientists served on the local committee. Without the enthusiastic commitment of Gernot Goll, Christoph Sürgers, and our secretaries Steffi Baatz and Birgit Schelske, the conference with over 1500 participants would not have been possible to master. Also, our young researchers such as diploma students, Ph.D. students, and postdocs, contributed largely to the success of the conference with their technical assistance for more than 2000 presentations at ICM 2009. The site of the conference was the Stadthalle Karlsruhe, and we are grateful to KMK Karlsruhe for efficiently organizing the technical details of running ICM 2009.

All research groups of the Physikalische Institut participate in the "Center for Functional Nanostructures" (CFN) funded by the DFG. This center provides substantial support for our research activities in the field of electronic transport in sub-micron structures down to single molecules and atoms as well as in superconducting circuits. Numerous further projects were funded by the Landesstiftung Baden-Württemberg, the DFG, the Ministerium für Wissenschaft, Forschung und Kunst in Baden-Württemberg, the Alexander von Humboldt Foundation, the German Academic Exchange Service, and the European Science Foundation.

Our research activities would not have been possible without the dedicated and hard work of all scientific and technical staff, as well as the doctorate and diploma students. After several years of large fluctuations in our electronic workshop, we are now back to stable conditions under the new head of the workshop, Roland Jehle. As always, Reinhold Dehm and his team of the mechanical workshop and Franz Hartlieb who runs the He liquefaction facilities, provided indispensable support. We thank Steffi Baatz and Birgit Schelske for their help and support in book-keeping and secretarial services. The administrative burden of the KIT process, including the introduction of SAP software demanded tedious work, flexibility and high frustration threshold. Lars Behrens takes care very skillfully of all our graphic work, runs our internet page, and manages the PC network.

The scientific results presented in this report have largely profited from the expert work of apl. Prof. Dr. Gernot Goll and apl. Prof. Dr. Bernd Pilawa, the post-doc scientists Dr. Pavel Bushev, Dr. Veronika Fritsch, Dr. Regina Hoffmann-Vogel, Dr. Oleksandre Lukashenko, Dr. Carmen Pérez León, Dr. Michael Marz, Dr. Stefano Poletto, Dr. Hannes Rotzinger, Dr. Toyo Kazu Yamadas, and –last but certainly not least– of our permanent scientific staff Dr. Gerda Fischer and Dr. Christoph Sürgers.

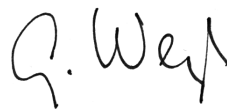
Karlsruhe, February 2010



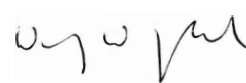
Hilbert v. Löhneysen



Alexey Ustinov



Georg Weiß



Wulf Wulfhekel



Prof. Dr. rer. nat. Friedhold Baumann
8. 4. 1927* – 24. 3. 2009[†]

The members of the Physikalische Institut mourn for Professor Friedhold Baumann who passed away unexpectedly on March 24th, 2009, after a short but severe illness.

Friedhold Baumann, shortly after having finished his doctorate at Universität Göttingen, came to Karlsruhe in 1960 together with Prof. Werner Buckel who had been appointed director of the Physikalische Institut. In the following years, Friedhold Baumann contributed largely to setting up low temperature physics at Universität Karlsruhe and we still profit of many of his achievements and decisions as acting director ranging from science to our technical infrastructure. In 1973, he was appointed Professor of Physics.

In science, Friedhold Baumann devoted his main interest to disordered solids particularly the transport properties of amorphous metals. He was a gifted teacher and acted to many of his students as a paragon for integrity and guidance. His passionate and emphatic personality influenced the general atmosphere in our institute. He was also highly respected in the Physics Faculty and served as its dean from 1986 to 1988.

For many years after his retirement, he regularly joined the Institut's Monday evening seminar and showed his closeness in numerous informal meetings, which he filled with warmth and deep personal interest. His friends and colleagues, his students and the members of the Physikalische Institut will not forget him.

International Conference on Magnetism ICM 2009

Stadthalle Karlsruhe, July 26 - 31, 2009

The International Conference on Magnetism 2009 (ICM 2009) was held in Karlsruhe, Germany, from July 26 to 31, 2009. The conference was hosted by Universität Karlsruhe and Forschungszentrum Karlsruhe, with Hilbert v. Löhneysen acting as Chairman. Previous conferences in this series were held in Edinburgh (1991), Warsaw (1994), Cairns (1997), Recife (2000), Rome (2003), and Kyoto (2006). As with previous ICM conferences, the annual Conference on Strongly Correlated Electron Systems (SCES) was integrated into ICM 2009.



Participants of ICM 2009 in front of the Stadthalle Karlsruhe.

Topics of ICM 2009 were: Strongly Correlated Electron Systems; Quantum and Classical Spin Systems; Magnetic Structures and Interactions; Magnetization Dynamics and Micromagnetics; Spin-Dependent Transport; Spin Electronics; Magnetic Thin Films, Particles, and Nanostructures; Soft and Hard Magnetic Materials and their Applications; Novel Materials and Device Applications; Magnetic Recording and Memories; Measuring Techniques and Instrumentation, as well as Interdisciplinary Topics. We are grateful to the International Advisory Committee for their help in putting up an attractive program encompassing practically all aspects of magnetism, both experimentally and theoretically. The Program Committee comprised A. Loidl, Germany (Chair), M. A. Continentino, Brazil, D. E. Dahlberg, USA, D. Givord, France, G. Güntherodt, Germany, H. Mikeska, Germany, D. Kaczorowski, Poland, Ching-Ray Chang, South Korea, I. Mertig, Germany, D. Vollhardt, Germany, and E. F. Wassermann, Germany. E. F. Wassermann was also head of the National Organizing Committee. His help is gratefully acknowledged.

The scientific program started on Monday, July 27, 2009 with opening addresses by the Conference Chairman, the Deputy Mayor of Karlsruhe, Ms. M. Mergen, and the Chairman of the Executive Board of Forschungszentrum Karlsruhe, E. Umbach. ICM 2009 was attended by three Nobel Laureates. P. W. Anderson gave a plenary talk on "Hidden Fermi Liquid". A. Fert and P. Grünberg presented plenary talks on "Generation of Microwave Oscillations by Spin Transfer, Synchronization of Spin Transfer Oscillators" and "Spintronics and its Applications", respectively. A special highlight was the presentation of the Magnetism Award and Néel Medal to S. S. P. Parkin who presented his newest results in a plenary talk "The Spin on Electronics". The IUPAP Young Scientist Award on Magnetism was given to S. O. Valenzuela, E. Saitoh, and T. Kimura. The conference came to a close on Friday, July 31, with two plenary talks given by Y. Tokura



Courtesy of Karlsruher Messe- und Kongress-GmbH



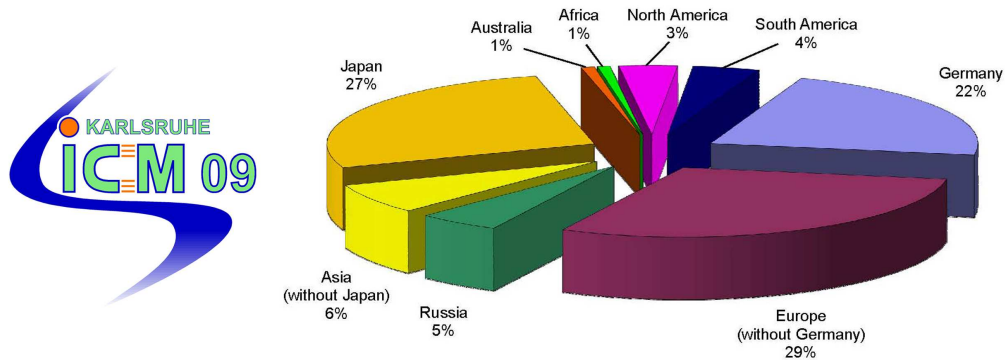
Courtesy of Karlsruher Messe- und Kongress-GmbH



Left: Poster session in the Stadthalle Karlsruhe. Upper right: H. v. Löhneysen (Conference Chairman), Nobel Laureates A. Fert and P. Grünberg, E. Umbach (Chairman of the Executive Board of Forschungszentrum Karlsruhe) (left to right). Lower right: Nobel Laureate P. W. Anderson.

on “Dynamical Magnetoelectric Effects” and M. Wegener on “Photonic Metamaterials: Magnetism Enters Photonics”.

The conference was attended by 1552 participants from 48 countries, with about 50 percent from overseas (see Figure). The program entailed six plenary talks (40 min each), with 16 half-plenary and 41 invited talks (30 min) and 298 contributed talks (15 min). Extended lunch breaks and evenings were devoted to the poster sessions, with a total of 1632 posters presented.



All submitted papers were reviewed in order to meet the standards of Journal of Physics: Condensed Matter and Journal of Physics: Conference Series. The referees made every effort possible to ensure that the manuscripts submitted for publication in the proceedings reach a high standard. The tremendous work in organizing the paper classification and refereeing procedures was carried out by the Publication Committee which was headed by J. Wosnitza, and comprised, in addition, Th. Pruschke, M. Richter, and L. Schultz.

We are grateful for financial support to Universität Karlsruhe (TH) and Forschungszentrum Karlsruhe [both institutions merged to form the Karlsruhe Institute of Technology (KIT) as of October 1, 2009], International Union of Pure and Applied Physics (IUPAP), the City of Karlsruhe, Deutsche Forschungsgemeinschaft (German National Science Foundation), and the European Commission through COST MPNS Action P16.

Contents

Magnetic materials and heavy-fermion systems	1
Magnetic flux penetration into a Pt/Co/Pt triple layer on Nb(110)	1
Dispersion and life times of magnetic excitations in thin Ni films	3
Quantum phase transitions	5
Pronounced enhancement of the thermoelectric power of $\text{CeCu}_{6-x}\text{Au}_x$ in the vicinity of the quantum critical point	5
Sample preparation, magnetization and resistivity of CeTiGe_3	7
Pressure dependence of the magnetic ordering wave vector in $\text{CeCu}_{5.5}\text{Au}_{0.5}$	9
Specific heat and magnetocaloric effect at the field-induced quantum critical point of $\text{CeCu}_{5.7}\text{Au}_{0.3}$	11
Concentration tuning in $\text{CePd}_{1-x}\text{Ni}_x\text{Al}$ heavy-fermion compounds	13
Superconductors	15
Resistivity and magnetization measurements on doped and undoped barium iron pnictide	15
Point-contact spectroscopy on doped and undoped 122 iron pnictides in the normal state	16
Point-contact spectroscopy on K-doped BaFe_2As_2 in the superconducting state	18
High-pressure magnetization measurements on Co-doped BaFe_2As_2	20
Superconducting qubits and Josephson devices	22
Rabi spectroscopy of a strongly driven qubit-fluctuator system	22
Implementation of superconductor-ferromagnet-superconductor π -shifters in superconducting quantum circuits	24
Two-photon spectroscopy of the hybrid quantum system	26
Observation of a dissipative dynamics in a strongly coupled TLS-qubit system	27
Noise measurements of cryogenic amplifiers for qubit experiments	28
Depinning of fluxons in Josephson arrays with magnetic inhomogeneities	30
Microwave fluxon readout for superconducting qubits	32
Search for charge solitons in small-capacitance Josephson junction arrays	33
Searching for “Münchhausen Effect” in an asymmetric dc-squid	34
A tunable rf squid manipulated as flux and phase qubit	36
Investigation of dielectric losses in amorphous thin-films used in Josephson junction fabrication . .	38
Nanostructures on surfaces	40
Lifetimes of magnetic excitations in Fe and Co atoms and clusters on Pt(111)	40
Giant magneto resistance of single molecules	42
STM and STS on Ag islands and Co/Ag on Nb(110)	44
Pulse injection of air onto Cu(111) surfaces: copper oxide surface structures	46
Disordered solids	48
Low temperature dielectric properties of $^{88}\text{Sr}^{48}\text{TiO}_3$	48
Low frequency acoustic measurements of amorphous $\text{Zr}_{59}\text{Ti}_3\text{Cu}_{20}\text{Ni}_8\text{Al}_{10}$	51
Miscellaneous	53
Test of a ultra-high vacuum sub-Kelvin scanning tunneling microscope with high energy resolution	53
Imaging the resistive states in thin NbN narrow strips using a low temperature laser scanning microscope	55
Photon count imaging of NbN single photon detectors	57
Diploma theses	59
Doctoral dissertations	59
Long-term guests	60
Teaching activities	60

Seminar talks at Physikalisches Institut	63
Publications	65
Scientific and technical staff	67

Effect of magnetic flux penetration on the magnetic hysteresis loops of a Pt/Co/Pt triple layer on Nb(110)

N. Joshi¹, C. Sürgers, H. v. Löhneysen

The magnetic interaction between a ferromagnet (F) and a superconductor (S) has been studied intensely in recent years [1]. In F/S systems with metallic contact the superconductor might modify the domain structure and/or the domain-wall width by the proximity effect [1]. Besides the proximity effect, the purely orbital contribution, i.e., the electromagnetic coupling between S and F plays an additional role. For a F/S bilayer in a perpendicular magnetic field, which is often considered by theory, demagnetization effects are strong, leading to an immediate penetration of vortices even in very weak magnetic fields. In order to study the effect of diamagnetic screening currents on the domain structure in F, thick superconducting substrates are more suitable. A drawback when using a thin F film on a thick S substrate is the fact that the magnetic response measured by standard magnetometry is dominated by the screening behavior of S for $T < T_c$. However, the magnetization curve $M(H)$ of the thin F film can be studied without a contribution from S by means of the magneto-optical Kerr effect (MOKE) where the polarization axis of linearly polarized light is slightly rotated after reflection from a metallic ferromagnetic film. During the last decades magneto-optic techniques (Faraday rotation) have been employed to investigate the magnetic flux structure of superconductors [2] and special care was taken to avoid ferromagnetic ordering of the magneto-optically active layer that would distort the magneto-optic image of the flux structure. On the other hand, in the present case, where interest is focused on the effect of a bulk superconductor on the magnetic properties of a thin F layer, MOKE is a perfect tool to measure the magnetization loop $M(H)$ of F on S via the Kerr rotation $\phi(H) \sim M(H)$.

We have investigated a thin ferromagnetic (20 Å Pt/15 Å Co/20 Å Pt) triple layer with perpendicular magnetic anisotropy, deposited on a superconducting Nb(110) single crystal. The Nb(110) disk (6.4 mm diameter, 1.35 mm height) was mechanically polished followed by electrochemical etching. The substrate was cleaned by several cycles of 2-keV Ar⁺ ion bombardment and subsequent heating to 1000 °C in ultrahigh vacuum. A buffer layer of 200 Å Nb was deposited by electron-beam evaporation at a substrate temperature $T_S = 650$ °C. After cooling to $T_S = 300$ °C, a triple layer of 20 Å Pt/15 Å Co/20 Å Pt was deposited with growth rates of 0.2 Å/s.

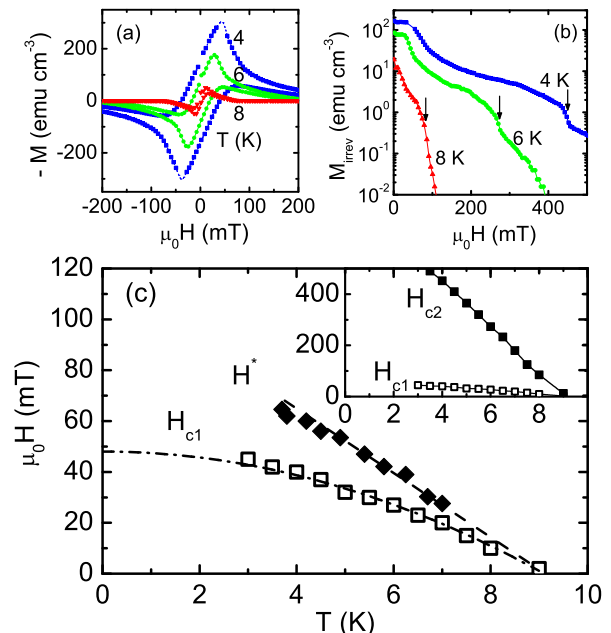


Figure 1: (a) Magnetization loops $M(H)$ of Nb(110)/Pt/Co/Pt in perpendicular magnetic field H at various temperatures T measured by VSM. (b) Irreversible magnetization $M_{irrev}(H)$ calculated from $M(H)$. Arrows indicate H_{c2} . (c) Critical fields H_{c1} and H_{c2} and penetration field H^* vs. temperature T . Dashed-dotted line shows a $[1 - (T/T_c)^2]$ behavior, see text. Dashed line indicates a linear behavior and the solid lines (inset) serve as guides to the eye.

Fig. 1(a) shows the magnetization curves $-M$ vs. H of the sample measured by vibrating sample magnetometry (VSM). Due to the dominant diamagnetic signal of S a contribution from the Pt/Co/Pt is not observed. In the mixed state of the superconductor, M is composed of the equilibrium magnetization and the irreversible magnetization M_{irrev} arising from the surface (Bean-Livingston) barrier as well as from bulk pinning of magnetic vortices at various defects in S. The lower critical field H_{c1} above which flux starts to enter the superconductor from the outer boundary is directly obtained as the field where $M(H)$ has a maximum in Fig. 1(a). $H_{c1}(T)$ can be reasonably described by a square-root behavior $H_{c1}(T) = H_{c1}(0)[1 - (T/T_c)^2]$ with $H_{c1}(0) = 49$ mT and $T_c = 9.1$ K, see Fig. 1(c). The upper critical field H_{c2} is obtained from the sudden drop of the

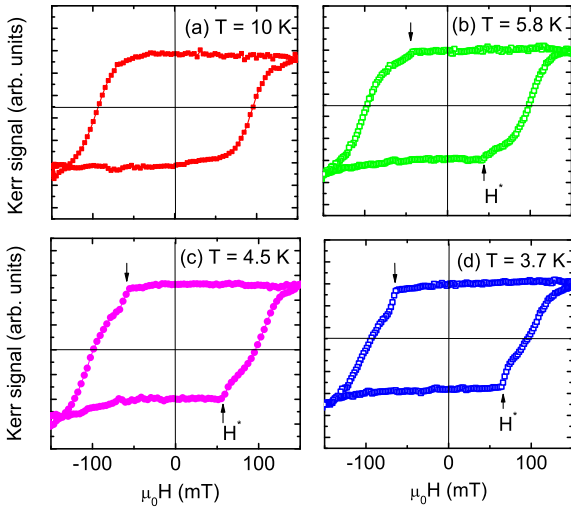


Figure 2: Polar Kerr loops recorded in the normal state at $T = 10$ K (a) and in the superconducting state below $T_c = 9.1$ K (b-d). Arrows indicate the field H^* where magnetic flux penetrates into the center of the superconducting disk with a concomitant sudden jump of the Kerr signal.

$M_{irrev} = (M^+ - M^-)/2$ (M^+ , M^- correspond to the ascending and descending branch of the $M(H)$ loop, respectively) plotted in Fig. 1(b). The temperature dependence of the critical fields is plotted in Fig. 1(c). We estimate $H_{c2}(0) = 660$ mT assuming the same $H_{c2}(T)$ dependence as found for $H_{c1}(T)$. Within Ginzburg-Landau theory the following superconductive parameters are estimated [3]: Ginzburg-Landau parameter $\kappa(0) = H_{c2}(0)/\sqrt{2}H_c(0) = 2.3$ with $H_c(0) = 200$ mT for bulk Nb, coherence length $\xi_S(0) = \sqrt{\hbar/2e\mu_0 H_{c2}(0)} = 223$ Å, penetration depth $\lambda(0) = \kappa(0)\xi_S(0) = 513$ Å.

Figure 2 shows polar MOKE loops recorded in the normal state ($T = 10$ K) and in the superconducting state ($T < 9.1$ K) of the Nb(110) substrate. In the normal state, the loop shows the $M(H)$ behavior characteristic of the ferromagnetic Pt/Co/Pt triple layer with strong out-of-plane anisotropy and large coercivity due to strongly pinned magnetic domains. Similar loops have been obtained for Co/Pt multilayers on Nb(110) films by VSM for $T > T_c$ [4]. After magnetic saturation and reversing the field direction, $M(H)$ of the F triple layer starts to decrease for fields $|H| > 75$ mT and is reduced to zero at a coercive field $H_{coerc} \approx 100$ mT.

In the superconducting state a sudden change of the magnetization appears at fields H^* smaller than H_{coerc} for both sweep directions, indicating a partial reversal of the sample's magnetization. H^* increases with decreasing temperature and is larger than the lower critical field H_{c1} determined from the VSM

measurements, see Fig. 1(c). We mention that H^* is lower in measurements with the light spot positioned near the edge compared to the center of the circular sample. This suggests that H^* can be identified as the field for which magnetic flux penetrates into the center of S in the form of quanta $\phi_0 = h/2e$. H^* usually exceeds the lower critical field due to the pinning force characterized by a critical current density j_c . This flux penetration into the Nb disk locally reverses the magnetization of magnetic domains in the Pt/Co/Pt film and gives rise to a change of the Kerr signal. Hence, this demonstrates a local modification of the Pt/Co/Pt magnetization by the vortex pattern of the superconducting Nb substrate. The fact that $M(H)$ suddenly changes at a field H^* smaller than the coercive field of the Pt/Co/Pt triple layer is attributed to the local compression of magnetic flux in the vortex core with respect to the normal field to values that are higher than the applied magnetic field H . For magnetic fields slightly above H_{c1} the local magnetic field H_{loc} in the vortex core is estimated to $H_{loc}(\xi) = \phi_0(\ln\kappa + 0.12)/2\pi\lambda^2 = 115$ mT [3]. Hence, the local magnetic field in the vortex core at the S/F interface is larger than H_{coerc} even for applied fields $H < H_{coerc}$ and can locally flip the magnetic domains in the triple layer. This effect is stronger at lower temperatures due to the higher H^* approaching H_{coerc} , c.f. Figs. 2 (b-d).

In conclusion, our measurements demonstrate that in F/S systems with perpendicular anisotropy the flux variation in the immediate vicinity of the superconducting crystal in the mixed state can locally change the magnetization of the F layer on the scale of $2\lambda(0) \simeq 100$ nm. The effect is due to the enhanced local field in the vortex core compared to the applied field. In the present experiments, H_{coerc} of F is larger than H_{c1} and H^* . Clearly, in order to investigate the change of the magnetic domain structure by screening currents in the Meissner state of S, future experiments have to be performed on F/S systems with H_{coerc} of F lower than H_{c1} .

- [1] For a recent review see A. I. Buzdin, Rev. Mod. Phys. **77**, 935 (2005)
- [2] R. P. Huebener: *Magnetic Flux Structures in Superconductors* (Springer, Berlin 2001)
- [3] M. Tinkham: *Introduction to Superconductivity* (McGraw-Hill, New York, 1996)
- [4] A. Singh, C. Sürgers, H. v. Löhneysen, Phys. Rev. B **75**, 024513 (2007)

¹ Department of Physics, University of Basel, 4056 Basel, Switzerland

Dispersion and life times of magnetic excitations in thin Ni films

T. Balashov, A. Ernst¹, P. Buczek¹, L. Sandratskii¹, W. Wulfhekel

Magnetic excitations are the basis for the description of magnetization dynamics of ferromagnets. Simple Heisenberg ferromagnets, in which neighboring magnetic moments couple via the exchange interaction, have an excitation spectrum in form of magnons. These are collective excitations of total spin $1\hbar$ distributed over all magnetic moments in form of a propagating precessional wave. Most ferromagnets of technical relevance, i.e. iron, nickel and cobalt, are itinerant ferromagnets, in which the d-electrons carry the magnetic moment. These also form the conduction bands and are delocalized. As a consequence, a second type of magnetic excitations, i.e. Stoner excitations, exist. These are created when lifting a majority electron from below the Fermi level to an unoccupied minority state above and have the same quantum numbers as magnons. Further, most of the magnetic moment of itinerant ferromagnets stems from the d-electron spins such that a clear distinction of magnons and Stoner excitations becomes difficult. As has been shown by Slater, magnons can be written as coherent superpositions of localized Stoner excitations [1].

Thus, the magnetic excitation spectrum of itinerant ferromagnets needs a more sophisticated description. Magnons are collective excitations which show up as sharp poles in the imaginary part of the transverse susceptibility $\chi(q, \omega)$ of the ferromagnet while localized Stoner excitations appear as a diffuse background [2]. In some areas of the Brillouin zone, e.g. near the zone center, clear magnon dispersion branches can be found. Far out in the Brillouin zone, however, the magnon dispersion enters the Stoner continuum. In this case, magnons may decay into Stoner excitations and thus have a limited life time. In other words, the sharp peaks in the susceptibility are smeared due to hybridization with the Stoner continuum.

A notoriously difficult system is nickel. Neutron diffraction showed only broad peaks indicating the fast decay of magnons into Stoner excitations and the magnon dispersion deviates significantly from the usual $\cos(q/\pi a)$ form, even displaying an acoustic and optic branch [3]. In this work, we prepared thin Ni films on a non-magnetic Cu(100) surface. In the thin films, the magnetic excitations are quantized regarding their wave vector perpendicular to the film plane q_{\perp} such that standing modes are formed. The wave vector q_n of the n th standing mode is given by:

$$q_n = \frac{n}{N} Q_{\max}, n = 0, \dots, N - 1 \quad (1)$$

where Q_{\max} is the Brillouin zone boundary in bulk for the z axis direction and n is the thickness of the film in atomic layers (ML). In the film plane the excitations can travel freely and the wave vector q_{\parallel} is not quantized.

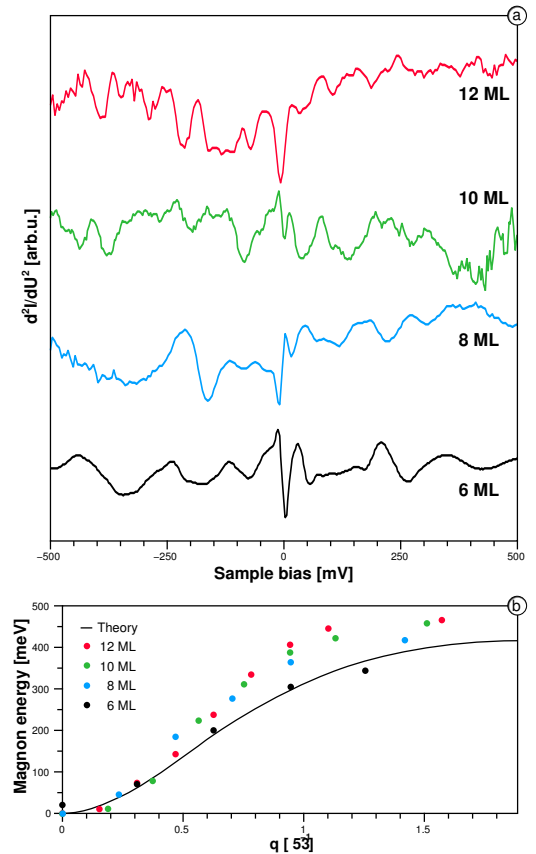


Figure 1: (a) d^2I/dU^2 measured on Ni films of indicated thickness on Cu(100) (b) The dispersion obtained from the experimental curves by matching peaks and dips for Ni/Cu(100). The solid line is the dispersion obtained by Pajda *et al.* for bulk fcc Ni [6].

Inelastic tunneling spectroscopy (ITS) [4], is a new method developed in Karlsruhe that allows to detect magnetic excitations in nanostructures by the energy loss of electrons in inelastic scattering events. Magnetic excitation caused by tunneling electrons emitted from the tip of a scanning tunneling microscope (STM) lead to peaks and dips in the second derivative of the tunneling current I with respect to the bias voltage U . A peak in d^2I/dU^2 is produced when the energy of the tunneling electron (eU) reaches the

energy of an inelastic excitation. Selection rules for the electron-magnon scattering imply that only low- q_{\parallel} magnons contribute to the spectra [5].

All the experiments were performed in ultra-high vacuum at 4.2 K. Ni films were deposited on Cu(100) at room temperature followed by cool down in the STM. The d^2I/dU^2 spectra were obtained using a lock-in operated at 16 kHz and 5 meV modulation. Figure 1a shows the d^2I/dU^2 spectra recorded on Ni films of different thicknesses. The spectra show peaks and dips due to magnon excitation. The number of peaks scales with film thickness as expected for standing modes. The width of the peaks, however, shows a rich dependence on energy. This can well be attributed to the complex magnon dispersion and the coupling to Stoner excitations. A strong damping of magnons in the region around 120 meV is seen in agreement with neutron scattering. Notably, spectra for 6 and 8 ML miss a peak in this region, that would be expected from the standing magnon model, but instead a plateau is visible. For 10 ML the plateau appears to be shifted to higher energies, and then disappears for 12 ML. However, the overall number of visible peaks is smaller than the number of layers. This can be either due to some modes overlapping in energy or due to so strong damping, that the modes cannot be detected as clear peaks.

To check for the reason and to understand more about the structure of the inelastic spectra, we have compared our spectra to theoretical calculations done in the non-adiabatic approach, which in contrast to the Heisenberg picture allows to see the interaction of magnons with the Stoner continuum.

The calculated transverse susceptibility in the (100) direction in bulk Ni, taken at the appropriate q_{\perp} , were compared to the positive side of the spectra as shown on Fig. 2. We see that the calculations reproduce the experimental results quite well, in what concerns peak positions and widths. The theoretical spectra had to be slightly scaled to lower energies to obtain a better match (the used local density approximation overestimates the exchange). One notices that the agreement between theory and experiment becomes worse for thinner films. This is also expected, as the theoretical calculations correspond to modes in bulk fcc Ni, and do not take finite size effects into account.

The calculations show that the small number of peaks, observed in the spectra, is mostly related to a flat top of the band, such that the last two to three modes are indistinguishable within the experimental resolution. The calculations also indicate that some of the double peak structures are related to lower modes having two maxima, one for the acoustic and one for the optical branch. Now, that we know

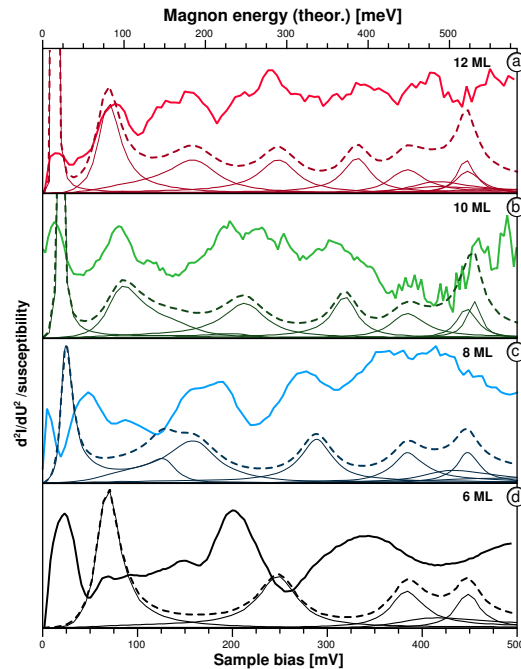


Figure 2: Comparison between experimental curves (solid) and the calculated transverse susceptibility for Ni/Cu(100). The thin lines are the individual theoretically calculated magnon modes.

the correspondence between peak and wave vector, the dispersion can be derived from the inelastic spectra. The results, presented in Fig. 1b, show that Ni thickness has a pronounced influence on the dispersion. The top of the band seems to be lower by about 100 meV in 6 ML of Ni as compared to 10 ML. The observed magnon dispersion agrees well with earlier adiabatic calculation for bulk fcc Ni by Pajda *et al.* [6]. At higher energies and in thinner films, however, a large discrepancy is observed indicating both deviations from the simple Heisenberg model as well as finite size effects.

- [1] J.C. Slater, *Phys. Rev.* **52** 198 (1937)
- [2] A.T. Costa *et al.* *Phys Rev B* **70** 54406 (2004)
- [3] M.A. Mook, D.M. Paul, *Phys. Rev. Lett.* **54** 227 (1985)
- [4] T. Balashov *et al.* *Phys. Rev. Lett.* **97** 187201 (2007)
- [5] T. Balashov *et al.* *Phys. Rev. B* **78** 174404 (2008)
- [6] M. Pajda *et al.* *Phys. Rev. B* **64** 174402 (2001)

¹MPI für Mikrostrukturphysik, Halle, Germany

Pronounced enhancement of the thermoelectric power of $\text{CeCu}_{6-x}\text{Au}_x$ in the vicinity of the quantum critical point

H. v. Löhneysen, J. Benz, T. Tomanic, C. Pfleiderer¹, O. Stockert²

The thermoelectric power is a fundamental transport property complementary to the electrical conductivity, as it involves transport of entropy and not just transport of electrical charge (or particle density). This property makes it a very interesting quantity to investigate near quantum critical points (QCP) of metallic systems, where the entropy at finite, albeit very low temperatures is shown to be strongly enhanced with respect to the Fermi-liquid value [1–3]. In a given material the excitations are governed by a single characteristic energy scale E^* , e.g., for itinerant electrons $E^* = E_F$ (Fermi energy), or for phonons $E^* = k_B\theta_D$ (Debye temperature), then S can be written as $S = f_0(T/E^*)$. A QCP is characterized by the vanishing of one (or possibly several [4]) characteristic energy scales. In the free-electron model, the thermoelectric power S is simply given by $S = \pm(\pi^2/\delta)(k_B/e)(k_B T/E_F) = \pm C_V/3N_A e$ where C_V is the electronic specific heat (per mole) and N_A is the Avogadro number [5]. The positive (negative) sign corresponds to hole (electron) transport. This simple relation approximately holds [6,7] even for heavy-fermion systems (HFS) where the heavy fermions are composite objects consisting - in the case of Ce compounds - of an f electron strongly coupled to conduction electrons by virtue of the Kondo effect. One might therefore naively expect that, if C_V diverges upon approach to a QCP, this divergence will also show up in the thermoelectric power. It is therefore surprising that only few experimental reports on S near a QCP have appeared [8–11]. On the theoretical side, it has been shown that within a spin density-wave (SDW) scenario of a magnetic QCP, S does indeed diverge for $T \rightarrow 0$ similarly to the specific heat [1]. During the last few years, a number of quantum critical systems have been found whose $T \rightarrow 0$ properties defy an explanation in terms of the SDW scenario, see Ref. 13 [13] for a review. Among these, $\text{CeCu}_{6-x}\text{Au}_x$ takes on a special role because thermodynamic, transport [14,15], as well as elastic [16] and inelastic neutron scattering [17–19] are available, the latter probing directly the critical fluctuations. The ω/T scaling of the dynamic susceptibility is incompatible with the SDW scenario, and has prompted various alternative approaches, one of the most prominent ones being the "local QCP"-scenario by Si et al. [20]. The issue of $S(T)$ for $T \rightarrow 0$ near such an unconventional QCP has been addressed recently [12]. Here, we report on

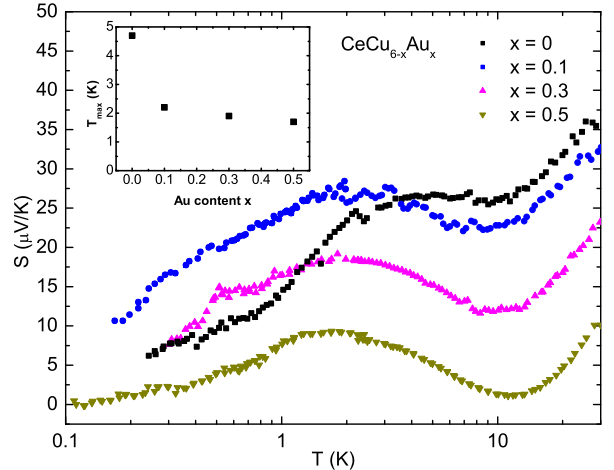


Figure 1: Temperature dependence of the thermopower S along the [1-0-0] direction of $\text{CeCu}_{6-x}\text{Au}_x$ for $x = 0, 0.1, 0.3$ and 0.5 . The data below 0.5 K were averaged over 5 data points. The inset shows the dependence of the Kondo temperature on the Au content x as determined by specific heat measurements.

a study of the thermoelectric power of $\text{CeCu}_{6-x}\text{Au}_x$ single crystals, extending considerably our brief previous study [8]. We show that $S(T)$ indeed diverges for $T \rightarrow 0$ around the quantum critical concentration $x_c \approx 0.1$. A magnetic field strongly reduces $S(T)$ and restores Fermi-liquid behavior [8]. Our experiments provide important input for a better understanding of QCPs in itinerant electron systems. Data were taken for heat flow along [100] and with magnetic field parallel to [001]. Samples were typically 2.5 mm long with a cross-section of $0.3\text{-}0.5$ mm². Data were taken between 0.1 and 2 K in a ³He/⁴He dilution refrigerator, and between 2 and 30 K in a standard ⁴He cryostat with similar measurement setups. Data were typically taken with a 3% difference in temperature. In view of the large scatter of the thermoelectric power for $T \rightarrow 0$, data below 0.5 K were averaged over 5 adjacent data points (running average). Before this procedure, data points that deviated by more than 15% from the average of all data points (obtained by a fifth-order polynomial fit) were discarded, e.g., 7 data points out of a total of 45 for $x=0.15$.

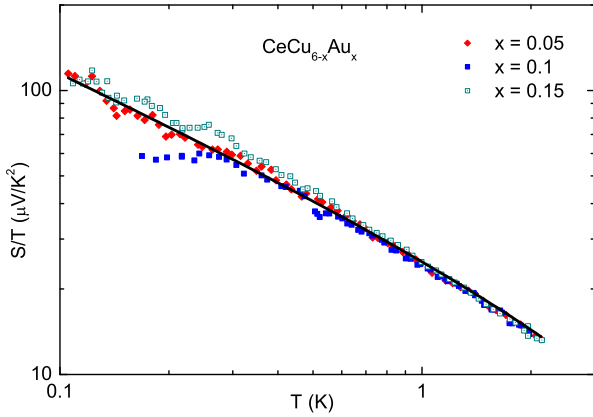


Figure 2: Low temperature thermoelectric power for $x = 0.05, 0.1, 0.15$. These data are shifted by $-10 \mu\text{V}/\text{K}$ for $x = 0.15$ and $+10 \mu\text{V}/\text{K}$ for $x = 0.05$

Fig.1 gives an overview over $S(T)$ for $x = 0, 0.1, 0.3$ and 0.5 and the total covered temperature range $0.1 \text{ K} \lesssim T < 30 \text{ K}$. The overall structure with a low- T maximum in $S(T)$ followed by a minimum toward higher T resembles the behavior well known from other Ce HFS, where the temperature of the $S(T)$ maximum is associated with the Kondo temperature T_K [7, 21] and the minimum marks the onset toward a high- T maximum due to the crystalline-electric-field (CEF) splitting of the Hund's rule $^2F_{5/2}$ ground-state multiplet [7]. Fig. 1 (inset) shows that T_K drops rapidly from $\approx 5 \text{ K}$ for $x = 0$ to $\approx 2 \text{ K}$ for $x \geq 0.1$. Although data are lacking to determine the exact x dependence of T_K in the vicinity of x_c , the present data are compatible with a jump of $T_K(x)$ around x_c recently observed from photoemission experiments [22].

In order to elucidate the quantum critical behavior of $S(T)$ in more detail, we have additionally measured the low- T thermoelectric power for $x = 0.05$ and 0.15 . The data are plotted as $\log S(T)$ vs $\log T$ in Fig 2. The data for the three samples around the quantum critical point, i.e., $x = 0.05, 0.1$, and 0.15 , follow a straight line in this plot, indicating an algebraic divergence $S(T) \sim T^{-\alpha}$ with $\alpha = 0.58$, although the data for $x = 0.1$ do not extend to low enough temperature to substantiate this behavior for this particular measurement. The algebraic behavior of $S(T)$ is in marked contrast to the specific heat $C/T \sim \ln(T_0/T)$ dependence. Further studies are underway to find the origin of this different behavior upon approach to the quantum critical point in $\text{CeCu}_{6-x}\text{Au}_x$.

This work was supported by the Deutsche Forschungsgemeinschaft through the Research Unit FOR 960.

- [1] I. Paul and G. Kotliar, Phys. Rev. B **64**, 184414 (2001)
- [2] L. Zhu et al., Phys. Rev. Lett. **91**, 066040 (2003)
- [3] H. v. Löhneysen, Physica B **378-380**, 1170 (2006)
- [4] P. Gegenwart et al., Science
- [5] N. W. Ashcroft and N. D. Mermin, Solid State Physics Saunders College Publishing, 1976
- [6] K. Behnia et al., J. Phys.: Cond. Matt. **16**, 5187 (2004)
- [7] V. Zlatić et al., Phys. Rev. B **76**, 085122 (2007)
- [8] J. Benz et al., Physica B **259-261**, 380 (1999)
- [9] T. Kuwai et al., Physica B **378.380**, 146 (2006)
- [10] K. Izawa et al., Phys. Rev. Lett. **99**, 147005 (2007)
- [11] J. Hartbaum et al., cond-mat/0807.-3420 (2008)
- [12] K.-S. Kim and C. Pepin, preprint.
- [13] H. v. Löhneysen et al., Rev. Mod. Phys. **79**, 1015 (2007)
- [14] H. v. Löhneysen et al., Phys. Rev. Lett. **72**, 3262(1994)
- [15] H. v. Löhneysen, J. Phys. Cond. Matt. **8**, 9689 (1996)
- [16] H. v. Löhneysen et al., Eur. Phys. J. B, (1998)
- [17] O. Stockert et al., Phys. Rev. Lett. **80**, 5627 (1998)
- [18] A. Schröder et al., Phys. Rev. Lett. **80**, 5623 (1998)
- [19] A. Schröder et al., Nature **407**, 351 (2000)
- [20] Q. Si, S. Raballo, K. Ingersent, and J. L. Smith, Nature **413**, 804 (2001)
- [21] We denote with "Kondo temperature" T_K the characteristic energy scale of the coupling of the Ce $4f^1$ moments to the conduction electrons in CeCu_6 being well aware of the fact that this is generally different in the corresponding dilute system. In this context, it is noteworthy that the specific heat of $\text{La}_{1-x}\text{Ce}_x\text{Cu}_6$ exhibits approximate single-ion scaling over the whole investigated range $0.1 \leq x < 1$ with a decrease of T_K by 31% between $x = 1$ and $x = 0.1$ (K. Satoh et al., J. Phys. Soc. Jpn. **58**, 1012 (1989))
- [22] M. Klein et al., Phys. Rev. Lett. **101**, 266404 (2008)

¹Technische Universität München, Physik Department, D-85748 Garching

²Max-Planck-Institut für Chemische Physik fester Stoffe, D-01187 Dresden

Sample preparation, magnetization and resistivity of CeTiGe₃

W. Kittler, V. Fritsch, G. Fischer and H. v. Löhneysen

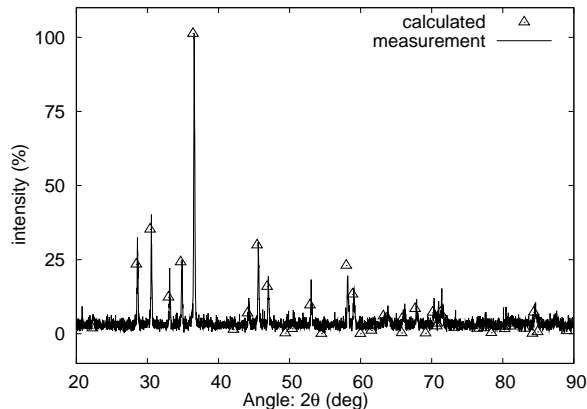


Figure 1: X-ray powder diffraction pattern of CeTiGe₃.

Relatively few heavy-fermion systems (HFS) exhibit ferromagnetic order compared to the numerous antiferromagnetic systems. In rare-earth-based HFS, the large effective masses arise from the Kondo effect in a lattice-coherent system ("Kondo lattice"). Since CeTiGe₃ was reported to be a ferromagnetic dense Kondo lattice [1], it might be a suitable candidate for studying the possible coexistence between magnetic order and Kondo effect, which was recently predicted theoretically [2].

Polycrystalline CeTiGe₃ was prepared by conventional argon-arc melting under an argon atmosphere and titanium gettering. To obtain a good homogeneity the samples were turned over and remelted several times. The samples were annealed at 1000° C for one week and subsequently quenched in liquid nitrogen. Powder x-ray diffraction measurements showed the samples to be single phase, crystallizing in the hexagonal perovskite BaNiO₃-structure with space group $hP10 - P6_3/mmc$. Magnetization measurements were performed in a commercial SQUID magnetometer in the temperature range between 2 and 300 K in magnetic fields up to 5 T. The resistivity was measured in a home-built ⁴He cryostat equipped with a superconducting magnet reaching fields up to 14 T, using a conventional four-terminal method with a LR-700 resistance bridge.

The x-ray powder diffraction patterns showed no traces of impurity phases in our samples, as shown in fig. 1. The samples crystallize in the desired hexagonal structure with the lattice parameters $a = 6.2633 \text{ \AA}$ and $c = 5.8631 \text{ \AA}$, in agreement with the

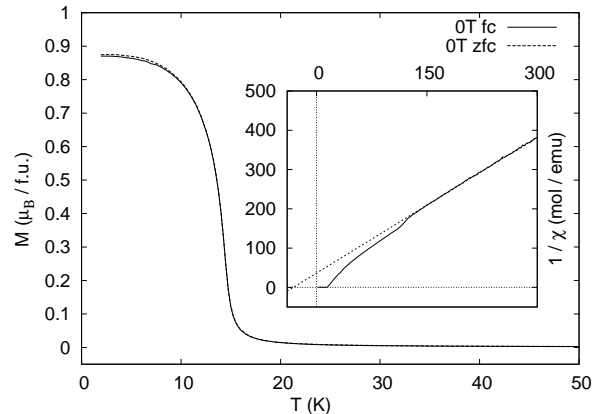


Figure 2: Main frame: Magnetization M vs temperature T of CeTiGe₃. Inset: Inverse dc-susceptibility $1/\chi_{dc} = H/M$ of CeTiGe₃ vs. temperature T .

previously reported values of Manfrinetti et al. [1].

Figure 2 presents the magnetization data of CeTiGe₃ in an external magnetic field of 0.1 T in the temperature range between 2 and 300 K. At the Curie temperature $T_C = 14 \text{ K}$ the onset of ferromagnetic order is clearly visible. There is no significant difference between zero-field cooled (zfc) and field-cooled (fc) data, indicating that the ferromagnet is almost reversible, i. e. the hysteresis loop is very small (see fig. 3 below). The inverse susceptibility $1/\chi_{dc} = H/M$ is shown in the inset of fig. 2. Above $T \approx 130 \text{ K}$ it varies linearly with temperature. A fit with a Curie-Weiss law $\chi = \frac{C}{T - \Theta_{CW}}$ yields a Curie constant $C = 0.87 \frac{\text{K}}{\text{mol}}$ and a Weiss temperature $\Theta_{CW} = -31.5 \text{ K}$. The negative value of the Weiss temperature, despite the clearly ferromagnetic order, was also found previously [1] and probably can be explained with the Kondo effect. From the Curie constant the effective paramagnetic moment was calculated to be $\mu_{eff} = 2.63 \mu_B$, close to the value $2.54 \mu_B$ expected for free Ce³⁺ ions. The small negative deviation of $1/\chi$ from the Curie-Weiss law below 130 K might be attributed to a small amount of an impurity phase present in the sample. A possible candidate for this impurity phase would be CeTiO₃, which orders antiferromagnetically at 116 K [3]. $M(T)$ curves under hydrostatic pressure up to 9 kbar (not shown) revealed a very small upward shift of the ferromagnetic transition temperature.

In fig. 3 a hysteresis loop measured at $T = 5 \text{ K}$ is shown. The width is indeed quite narrow indicat-

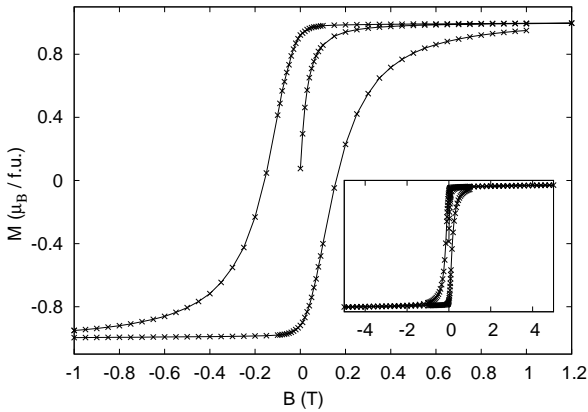


Figure 3: Main frame: Magnetization M vs external magnetic field B of CeTiGe_3 between -1 and 1.2 T. Inset: Magnetization M vs external magnetic field B of CeTiGe_3 between ± 5 T and a temperature of 5 K.

ing that CeTiGe_3 is a magnetically rather soft material as already inferred above from the similarity of fc and zfc $M(T)$ curves. Above a magnetic field of 1 T the magnetization is nearly constant and remains just below $1\mu_B/\text{f.u.}$, well short of the expected saturation moment of $2.14\mu_B/\text{f.u.}$ expected for the $5/2F_2$ Ce^{3+} ground state. The inset of fig. 3 shows that saturation is not yet reached at $T = 2$ K and $B = 5$ T.

The electrical resistivity of CeTiGe_3 is displayed in fig. 4. The inset shows the resistivity ρ of CeTiGe_3 in the whole temperature regime between 2 and 300 K: the temperature dependence of ρ at high temperatures is very small, after a shallow minimum ρ reaches a maximum at $T_M = 35$ K. Below T_M the resistivity falls steeply with a sharp kink at the Curie temperature $T_C = 14$ K. This behavior is usually associated with a transition from incoherent Kondo-like scattering at high temperatures to the lattice-coherent Bloch state of strongly correlated electrons at low temperatures. We could not observe any magnetoresistance around T_M in magnetic fields up to 5 T. At the lowest investigated temperatures the resistivity transforms into a temperature- and field-independent remnant resistivity. The resistivity ratio at $T = 2.5$ K of $RRR = 26$, in comparison to the previously reported value of approximately 13 [1], confirms the rather good quality of our samples. A magnetic field reduces the resistivity mainly around the Curie temperature, indicating a suppression of ferromagnetic fluctuations.

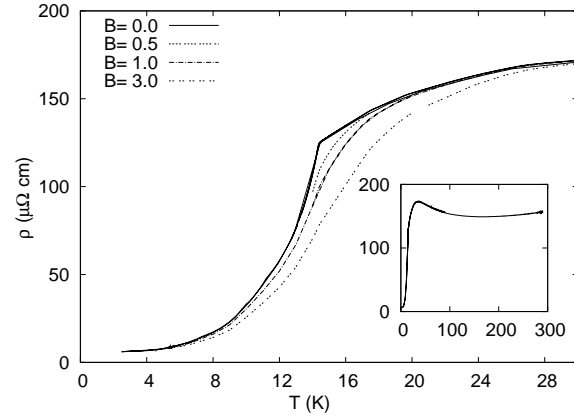


Figure 4: Resistivity ρ vs temperature T of CeTiGe_3 in different magnetic fields up to 5 T in the temperature range below 50 K. Inset: resistivity of CeTiGe_3 in the whole temperature range between 2 and 300 K.

In conclusion we prepared polycrystalline CeTiGe_3 , which is supposed to be a ferromagnetic dense Kondo lattice. Magnetization measurements under ambient pressure confirmed the onset of ferromagnetic order at $T_C = 14$ K and revealed a narrow hysteresis at low temperatures. At high temperatures above 150 K a paramagnetic effective moment $\mu_{\text{eff}} = 2.63 \mu_B$ was found. Such a stable moment was already reported for other Kondo compounds, e.g., CeFeGe_3 (which crystallizes in the tetragonal BaNiSn_3 structure) [4]. On a first glance the resistivity also seems to corroborate the system being a Kondo lattice: nearly temperature independent at high temperatures, then passing a maximum and a steep drop towards lower temperatures. Further investigations, such as measurements of specific heat and comparison with a non-magnetic reference sample, e.g., LaTiGe_3 are needed in order to clearly identify CeTiGe_3 as an example of a Kondo lattice.

This work was supported by the DFG through FOR960.

- [1] P. Manfrinetti et al., Sol. State Comm. **135**, 444 (2005).
- [2] M. D. Núñez-Regueiro and B. Coqblin, Physica B **359-361**, 741 (2005).
- [3] J. P. Goral and J. E. Greedan, J. Magn. Magn. Mater. **37**, 315 (1983).
- [4] H. Yamamoto et al., Phys. Rev. B **52**, 10136 (1995).

Pressure dependence of the magnetic ordering wave vector in $\text{CeCu}_{5.5}\text{Au}_{0.5}$

A. Hamann, O. Stockert¹, V. Fritsch, H. v. Löhneysen

CeCu_6 is a prototype heavy-fermion (HF) system that is rather well described by Fermi liquid (FL) theory ($\gamma = 1.6 \text{ J/mol K}^2$). Incommensurate anti-ferromagnetism (AF) is induced in the alloy series $\text{CeCu}_{6-x}\text{Au}_x$ for $x > x_c \approx 0.1$. T_N increases linearly with Au concentration (Fig. 1) and can be reduced by applying hydrostatic pressure p . In the vicinity of the quantum critical point (QCP), i.e., at the magnetic instability where $T_N = 0$, significant deviations from FL behavior have been observed, nicknamed non-FL (NFL) behavior [2, 3]. Moreover, the same quantum critical behavior of $\text{CeCu}_{5.9}\text{Au}_{0.1}$ is recovered by applying appropriate pressure to magnetically ordering $\text{CeCu}_{6-x}\text{Au}_x$ with $x > 0.1$. The quantum phase transition (QPT) can be tuned not only by x or p but also by magnetic field B . The field-tuned NFL behavior is in agreement with the standard Hertz-Millis-Moriya (HMM) model of three-dimensional (3d) itinerant quantum criticality [4, 5]. However, the x - or p -tuned QCP is in marked contrast to the HMM predictions: thermodynamic and transport data at respective QCP suggest 2d or even local quantum criticality which is corroborated by the results of inelastic neutron scattering (INS) [6, 7], prompting alternative scenarios [8, 9].

Previous measurements on $\text{CeCu}_{6-x}\text{Au}_x$ at ambient pressure revealed the positions of the magnetic Bragg peaks in the reciprocal a^*c^* plane (Fig. 2). Upon increasing x , the c^* component first decreases slowly and then abruptly drops to zero between $x = 0.4$ and $x = 0.5$ (Fig. 2 (b)) while $T_N(x)$ varies linearly. This apparent contrasting behavior needs clarification.

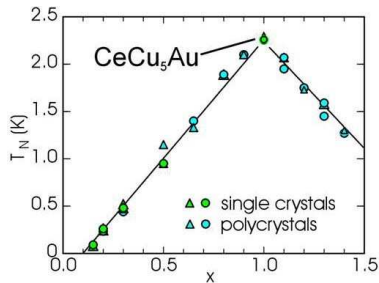


Figure 1: The Néel temperature T_N of $\text{CeCu}_{6-x}\text{Au}_x$ vs Au concentration x as determined from specific heat (triangles) and magnetic susceptibility (circles) [1]. For $0.1 \leq x \leq 1$, where Au exclusively occupies the Cu(2) positions in the CeCu_6 structure, T_N varies linearly with x .

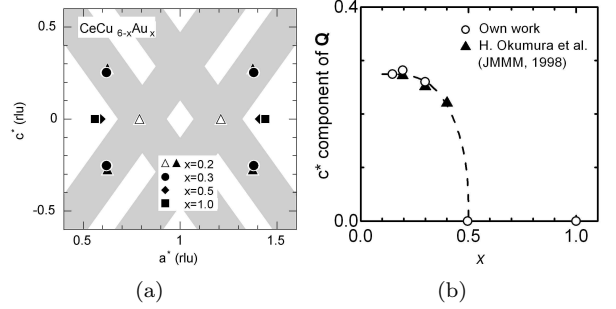


Figure 2: Previous results obtained by neutron diffraction on $\text{CeCu}_{6-x}\text{Au}_x$ at ambient pressure. (a) Doping dependence of the magnetic ordering wave vector in reciprocal a^*c^* plane. Filled symbols correspond to Bragg peaks and open symbols to short range fluctuations. Shaded regions indicate strong quasielastic scattering at the critical concentration $x = 0.1$ [10]. (b) c^* component of the magnetic ordering wave vector [11].

We therefore investigated the pressure dependence of the magnetic ordering of $\text{CeCu}_{5.5}\text{Au}_{0.5}$ using elastic neutron scattering. Our experiment was performed on the triple-axis spectrometer PANDA which is operated at the FRM II reactor in Munich. The sample was mounted in a Cu:Be pressure cell and cooled to 100 mK using a dilution refrigerator. We focused on elastic scans over the magnetic Bragg peak that corresponds to the (200) nuclear Bragg peak due to the large structure factor there. Fig. 3 shows the pressure dependence of the neutron intensity on a grid in the reciprocal a^*c^* plane covering the position of the magnetic Bragg peak of $\text{CeCu}_{5.5}\text{Au}_{0.5}$. In agreement with previous results, Fig. 3 (a) reveals that at ambient pressure the c^* component of the position of the maximum is very close to zero. (Note that investigations at $p = 0$ were performed with the sample in the pressure cell, too.) Upon applying $p = 8 \text{ kbar}$, the position of the Bragg peak significantly changes and assumes approximately the same c^* component that has been found for $\text{CeCu}_{5.7}\text{Au}_{0.3}$ at ambient pressure (Fig. 3 (b)). This indicates that by pressure tuning the sample towards the QCP, not only the thermodynamic and transport data [2, 3] but also the magnetic ordering wave vector of corresponding lower doping are recovered. On the other hand, at $p = 8 \text{ kbar}$ a small remnant peak at the position corresponding to am-

bient pressure ($c^* \approx 0$) is present (Fig. 3 (c)). We checked the magnetic origin of this feature by heating the sample above T_N where it disappears completely (see inset of Fig. 3 (c)). The double-peak structure is indicative of a Fermi surface providing two nesting vectors. Obviously, the corresponding energy levels are populated very differently with a clear preference of $c^* \approx 0.2$.

The T dependence of the intensity of the strong magnetic Bragg peak for $p = 0$ and $p = 8$ kbar is depicted in Fig. 4. Fitting the data with the mean-field behavior

$$I(T) = I_0 \cdot \left(1 - \left(\frac{T}{T_N}\right)^\nu\right) \quad (1)$$

yields respective Néel-temperatures and staggered magnetizations. The extraction of $T_N = 520$ mK at $p = 8$ kbar corroborates that the sample was indeed tuned very close to $x = 0.3$ behavior at $p = 0$, where according to [2] $T_N = 480$ mK was found.

To conclude, by applying hydrostatic pressure to $\text{CeCu}_{6-x}\text{Au}_x$ not only macroscopic properties such as the specific heat, magnetic susceptibility or specific resistivity of correspondingly lower doping x are recovered. We succeeded in showing that a microscopic quantity, i.e., the magnetic ordering wave vector, can be tuned accordingly. Ultimately, the goal must be to tune the sample into quantum criticality and to investigate the fluctuations there. Comparing with previous neutron scattering results on $\text{CeCu}_{5.9}\text{Au}_{0.1}$ could help to gain more insight into the mechanisms that drive the QPT.

This work was supported by the DFG through FOR960.

- [1] T. Pietrus et al., Physica B, **206-207**, 317 (1995).
- [2] H. v. Löhneysen, J. Phys.: Condens. Matter **8**, 9689-9706 (1996).
- [3] H. v. Löhneysen et al., Rev. Mod. Phys., **79**, 1015 (2007).
- [4] J. A. Hertz, Phys. Rev. B, **14**, 1165 (1976).
- [5] A. J. Millis, Phys. Rev. B, **48**, 7183 (1993).
- [6] O. Stockert et al., Phys. Rev. Lett., **80**, 5627 (1998).
- [7] A. Schröder et al., Nature, **407**, 351 (2000).
- [8] P. Coleman et al., Phys. Rev. B, **62**, 3852 (2000).
- [9] Q. Si et al., Nature, **413**, 804 (2001).
- [10] H. v. Löhneysen et al., Eur. Phys. J. B, **5**, 447 (1998).
- [11] P. Estrela et al., J. Magn. Magn. Mater., **272-276**, 23 (2004).

¹ Max-Planck-Institut für Chemische Physik fester Stoffe, 01187 Dresden

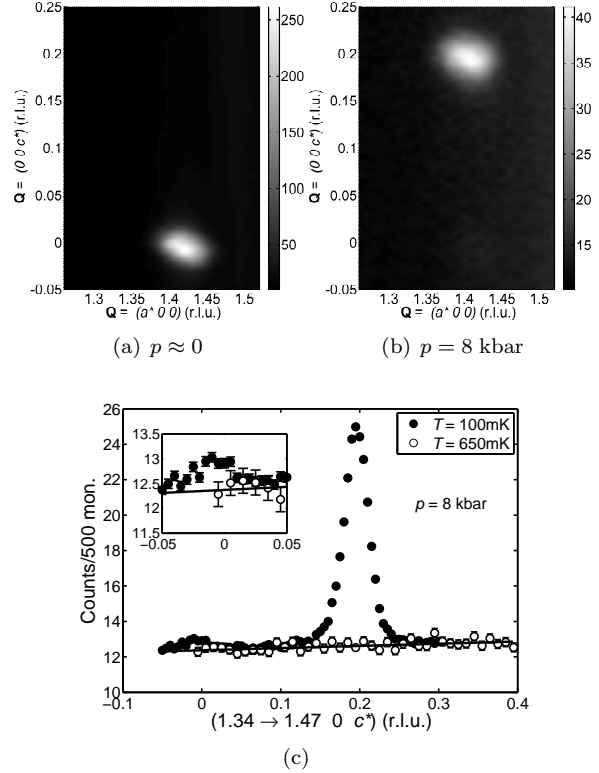


Figure 3: Position of the magnetic Bragg peak of $\text{CeCu}_{5.5}\text{Au}_{0.5}$ in plane that is spanned by reciprocal $[a^* 0 0]$ and $[0 0 c^*]$ directions at ambient pressure (a) and at $p = 8$ kbar (b) at $T = 100$ mK, respectively. (c) Temperature dependence of neutron intensity in c^* direction at $p = 8$ kbar. Each data point shows intensity summed in a^* direction for $1.34 \leq a^* \leq 1.47$. The solid line is a fit to data obtained at $T = 650$ mK. The inset shows data at $-0.05 \leq c^* \leq 0.05$ on a larger scale.

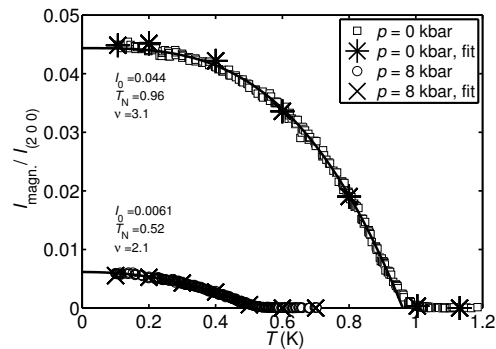


Figure 4: Magnetic intensity normalized to nuclear (200) Bragg peak. Data shown as squares or circles were taken at the $2d$ -fitted positions. Data shown as asterisks or crosses were extracted from $2d$ -fitting several scans over the Bragg peak in a^* and c^* direction and are in agreement with squares and circles.

Specific heat and magnetocaloric effect at the field-induced quantum critical point of $\text{CeCu}_{5.7}\text{Au}_{0.3}$

M. J. Wolf, G. Goll, V. Fritsch, H. v. Löhneysen

The investigation of the role of different tuning parameters at a quantum critical point (QCP) between magnetic and non-magnetic ground states in heavy-fermion systems is an active research field. Concentration-tuning of the QCP in $\text{CeCu}_{6-x}\text{Au}_x$ showed an unusual quantum-critical behavior for the critical concentration x_c dubbed "local quantum criticality" as revealed by inelastic neutron scattering (INS) [1]. Subsequent measurements of the specific heat [2] and INS [3] on $\text{CeCu}_{5.8}\text{Au}_{0.2}$ revealed different behavior when the incommensurate antiferromagnetic order was suppressed by magnetic fields and hydrostatic pressure. At the field-induced QCP of $\text{CeCu}_{5.8}\text{Au}_{0.2}$ the data can be very well described by the self-consistent renormalization model of Moriya and Takimoto [4] in a broad temperature regime from 60 mK to 2 K, whereas the similarity of the behavior at the pressure-induced QCP to that of the zero-pressure QCP at $x_c = 0.1$ suggests that the local-moment scenario applies to the pressure-driven QCP as well [2]. These findings led to the interest in specific heat measurements in magnetic fields at another Au concentration of the system $\text{CeCu}_{6-x}\text{Au}_x$.

Therefore a new measurement system was set up and an extended and automated measurement routine was programmed in LabVIEW.

We used a "semiadiabatic" heat-pulse technique to determine the specific heat and magnetocaloric effect. A short current pulse (usually 50 to 500 ms) at a time t_0 deposits a known amount of heat ΔQ and causes a temperature increase of the sample (usually chosen to $\approx 3\%$) which relaxes after the pulse to the initial temperature. Fitting an exponential function to this temperature decay and extrapolating to t_0 leads to the initial temperature increase ΔT and hence the specific heat can be calculated $C = \frac{1}{m} \frac{\Delta Q}{\Delta T}$.

In the magnetocaloric measurements the temperature change is caused by a change of the magnetic field B . To eliminate dissipative effects, we always measured the temperature change after positive as well as negative field changes and took the averaged difference $\frac{\Delta T}{\Delta B} = \frac{\Delta T^+ - \Delta T^-}{2|\Delta B|}$ as the magnetocaloric effect.

The $\text{CeCu}_{5.7}\text{Au}_{0.3}$ single crystal ($m = 32.8$ mg) is mounted in the $^3\text{He}/^4\text{He}$ dilution refrigerator with $B||c$, i.e., along the easy crystallographic axis. Fig. 1 shows the measured specific heat data in a C/T vs. $\log T$ -plot after a subtraction of the Cu-hyperfine term and measurement-setup (addenda) contribu-

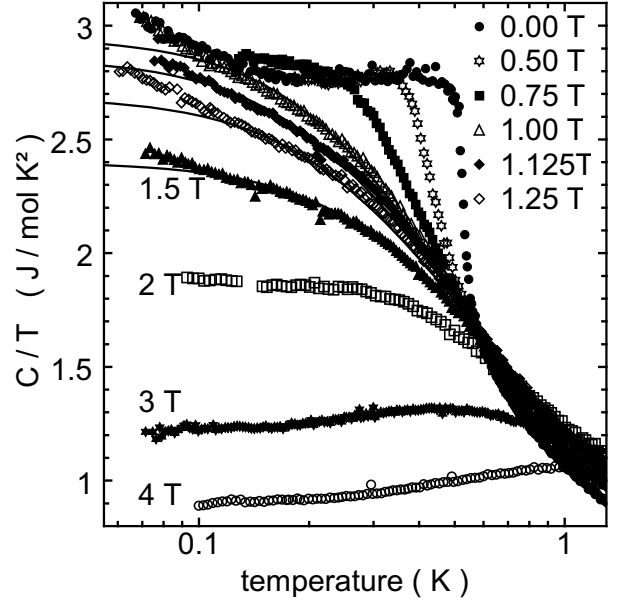


Figure 1: Specific heat C of $\text{CeCu}_{5.7}\text{Au}_{0.3}$ after subtraction of hyperfine and addenda contributions in different magnetic fields ($B || c$).

tions (heater, thermometer, grease, etc.). The phase transition for $B = 0$ is located at $T = 530 \pm 10$ mK, which is slightly larger than expected from previous measurements [5]. With increasing magnetic field the transition broadens and makes it difficult to determine the transition temperature. In magnetic fields above 2 T, a constant C/T towards the lowest measured temperatures is found, indicating a crossover to Fermi liquid behaviour.

Near the critical field B_c (see below) the parameters of the spin-fluctuation formula (eqn. 4.5 in [4]) were iteratively modified to match the specific-heat data. Apart from the increase of the specific-heat data towards the lowest measured data points, the agreement between the theoretical curve and the data points (solid lines in Fig. 1) is very good in the temperature interval from 0.1 to 1 K. This leads to the conclusion that in $\text{CeCu}_{5.7}\text{Au}_{0.3}$ the onset of antiferromagnetism at the critical magnetic field is driven by a spin-density wave. This is in strong contrast to early data of the pressure-driven QCP for the same concentration $x = 0.3$ [5] whose $\log(T_0/T)$ dependence of C/T is in agreement with the local

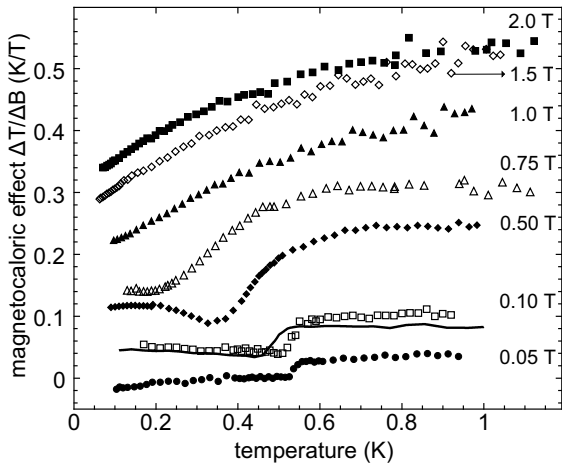


Figure 2: Magnetocaloric effect of $\text{CeCu}_{5.7}\text{Au}_{0.3}$ in different magnetic fields ($B \parallel c$). The curves are shifted by 0.05 K/T for better visibility.

moment scenario.

For the identification of the critical field B_c , magnetocaloric measurements were performed. Magnetocaloric temperature sweeps show (Fig. 2) a step-like increase at the phase transition for small fields ($B = 50$ and 100 mT) which broadens as well when approaching B_c . For fields higher than $B = 1$ T no jump but a continuous increase of the magnetocaloric effect can be identified.

The magnetocaloric effect can be related to the specific heat and magnetization via $\frac{dT}{dB} = \frac{\partial M / \partial T}{C_B / T}$ [6]. To check for consistency, the magnetocaloric effect was calculated from the data given in [6] and is shown in Fig. 2 as a solid line. The overall agreement between the two data sets is good, the small offset of the "directly" measured magnetocaloric data is most likely due to the non-ideal correction for dissipative effects. Garst et al. pointed out that at a QCP a sign change of the magnetic Grüneisen ratio Γ_M can be observed [7]. Γ_M is linked to the magnetocaloric effect just by a division by temperature, $\Gamma_M = \frac{1}{T} \frac{dT}{dB}$. The observed shift of the magnetocaloric effect data towards positive values is most likely the reason, why we do not observe a sign change but just a jump of the magnetocaloric effect at the phase transition.

From the whole ensemble of measurements (including magnetocaloric field sweeps not shown) the magnetic phase diagram was mapped out (Fig. 3).

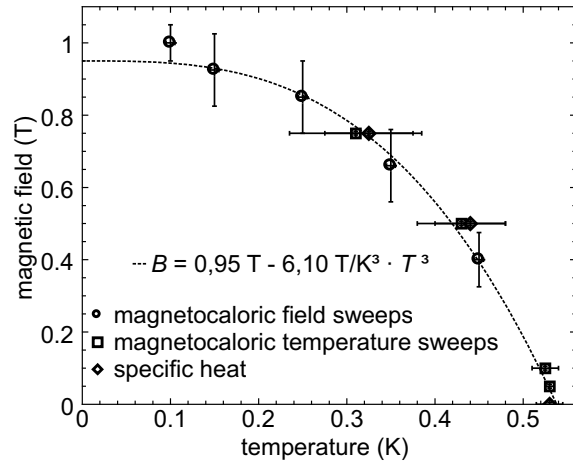


Figure 3: Magnetic phase diagram for $\text{CeCu}_{5.7}\text{Au}_{0.3}$ ($B \parallel c$).

A fit according to the data points with $T = (B_c - B)^{1/c}$ led to $B_c = 0.95 \pm 0.1$ T. The fit-exponent is nearly $c \approx 3$ which is strongly deviating from molecular field theory ($c = 2$) and spin-fluctuation theory for a 3d antiferromagnet ($c = 3/2$) [7].

In conclusion, the specific heat data of $\text{CeCu}_{5.7}\text{Au}_{0.3}$ show the same behavior as $\text{CeCu}_{5.8}\text{Au}_{0.2}$ with respect to tuning by a magnetic field and hydrostatic pressure and thus corroborated the previously found sensitivity of $\text{CeCu}_{6-x}\text{Au}_x$ to the tuning parameter of the QCP.

This work was supported by the DFG through FOR960.

- [1] A. Schröder et al., Nature **407**, 351 (2000)
- [2] H. v. Löhneysen et al., Phys. Rev. B **63**, 134411 (2001)
- [3] O. Stockert et al., Phys. Rev. Lett. **99**, 237203 (2007)
- [4] T. Moriya and T. Takimoto, J. Phys. Soc. Japan **64**, 960 (1995)
- [5] B. Bogenberger and H. v. Löhneysen, Phys. Rev. Lett. **74**, 1016 (1995)
- [6] H. G. Schlager et al., J. Low Temp. Phys. **90**, 181 (1993)
- [7] M. Garst and A. Rosch, Phys. Rev. B **72**, 205129 (2005)
- [8] H. v. Löhneysen et al., Rev. Mod. Phys. **79**, 1015 (2007)

Concentration tuning in $\text{CePd}_{1-x}\text{Ni}_x\text{Al}$ heavy-fermion compounds

N. Bagrets, V. Fritsch, G. Goll, K. Grube¹, S. Drobnik¹, M. Wolf, and H. v. Löhneysen

The heavy-fermion compound CePdAl orders antiferromagnetically (AF) at 2.7 K [1,2]. It crystallizes in the hexagonal ZrNiAl structure space group $P62m$ [1,2]. The magnetic Ce ions form a network of equilateral triangles in the ab plane, similar to the Kagomé lattice. Neutron diffraction measurements on powder samples have shown that two thirds of the Ce moments are ordered antiferromagnetically below the transition temperature with a propagation vector $k=(1/2\ 0\ 0.351)$, while one third remains paramagnetic [2]. Hence, the system is partially frustrated. The frustration parameter $f = \Theta/T_N$ is usually taken to characterize the degree of frustration. In CePdAl it was determined to be $f = 10.8$ which is rather large. According to this definition, a material with $f \geq 3$ is moderately frustrated, materials with $f > 10$ are considered to be strongly frustrated materials [3].

The competition between RKKY interaction and Kondo screening in heavy-fermion systems may lead to quantum critical behavior near $T \rightarrow 0$, i.e., the system can be tuned to a quantum critical point (QCP) by applying hydrostatic pressure [4] or by doping (chemical pressure) [5]. It was shown that T_N in CePdAl is reduced down to 1.7 K under 0.9 GPa [4]. Therefore, it is of interest to investigate the effect of chemical pressure in the substituted system $\text{CePd}_{1-x}\text{Ni}_x\text{Al}$. Previous studies [5] have shown that magnetic order disappears at a Ni content $x \geq 0.1$.

In this paper we present the results of measurements of the specific heat C of $\text{CePd}_{1-x}\text{Ni}_x\text{Al}$ alloys for Ni concentrations $0 \leq x < 0.15$. We compare the cell volume compression by applying both hydrostatic and chemical (doping with Ni) pressure. In addition, we discuss the behavior of the system near the critical concentration, where the transition temperature will be tuned towards zero. The Hertz-Millis [7,8] theory predicts for C/T versus T for two-dimensional antiferromagnets a logarithmic divergence near the QCP. We will show that at $x = 0.144$ this type of quantum critical behavior is observed.

Polycrystalline samples of $\text{CePd}_{1-x}\text{Ni}_x\text{Al}$ were prepared by arc-melting the pure elements of Ce(99.9), Pd(99.95), Ni(99.95), Al(99.999) in their stoichiometric ratio under argon atmosphere and titanium gettering. All $\text{CePd}_{1-x}\text{Ni}_x\text{Al}$ compounds crystallize in hexagonal ZrNiAl -type structure. The $\text{CePd}_{1-x}\text{Ni}_x\text{Al}$ samples were used as-cast since annealing causes a change of their structure type. Specific-heat measurements for the $\text{CePd}_{1-x}\text{Ni}_x\text{Al}$ samples with $x = 0.020, 0.052, 0.097, 0.104, 0.125,$

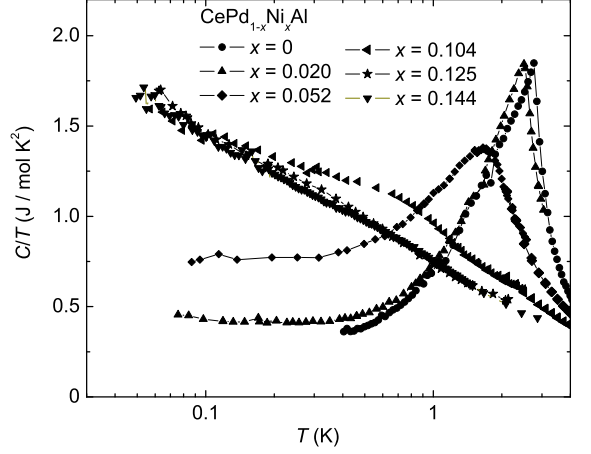


Figure 1: C/T versus T for $\text{CePd}_{1-x}\text{Ni}_x\text{Al}$ ($x = 0, 0.020, 0.052, 0.097, 0.104, 0.125, 0.144$).

and 0.144 were performed using a dilution refrigerator in the temperature range 0.03 – 2.5 K.

In Fig. 1 the dependences of C/T on T are shown. The CePdAl compound ($x = 0$) shows a clear λ -type anomaly at the Néel temperature $T_N = 2.7$ K. The anomaly is broadening for the doped compounds, and T_N moves towards lower temperatures with increasing Ni content. For the sample with $x = 0.104$ the antiferromagnetic (AF) transition is still visible as a broad shoulder in the C/T plot around 1 K. At $x = 0.131$ the AF transition is hardly visible. It is very weakly seen at about 0.25 K. For the concentration $x = 0.144$ no transition was found in the temperature range 0.05–3 K. C/T can be fitted rather well by $C/T = a \ln(T_0/T)$, with $a = 0.298$ J/molK² and $T_0 = 12.5$ K over almost two decades in temperature. Thus, the $\text{CePd}_{1-x}\text{Ni}_x\text{Al}$ system presents a further example of quantum critical behavior induced by concentration tuning. In Fig. 2 we show T_N versus x obtained from the specific-heat measurements. The experimental points can be fitted with $T_N(x) = T_N(0)|x - x_c|$, which is expected within the Hertz/Millis [7,8] scenario for the case of a 2D AF. The extrapolation to $T_N = 0$ suggests that x_c is very close to 0.144.

From the magnetization measurements the paramagnetic effective moments μ_{eff} and Weiss-temperatures Θ were determined (see Table 1). The negative Curie-Weiss temperature Θ indicates antiferromagnetic interactions. The kinks in $\chi(T)$ were taken as ordering temperature. For $x=0.104$ the T_N

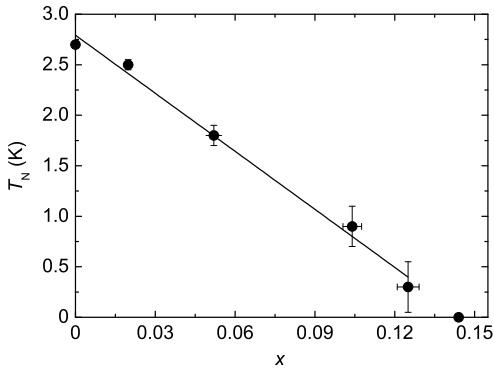


Figure 2: T_N versus Ni concentration x for $\text{CePd}_{1-x}\text{Ni}_x\text{Al}$.

x	$\mu_{\text{eff}}/\text{Ce atom } (\mu_B)$	Θ (K)	Θ/T_N
0	2.42	-35.7	10.8
0.020	2.41	-31.5	10.2
0.039	2.42	-32.5	12.5
0.061	2.46	-35.7	15.5
0.078	2.42	-32.4	18
0.104	2.41	-32.2	23

Table 1: Effective paramagnetic moments and Weiss temperatures for powder samples $\text{CePd}_{1-x}\text{Ni}_x\text{Al}$ as determined from magnetisation measurements in $B = 100$ mT.

was taken from AC susceptibility measurements.

The frustration parameter $f = \Theta/T_N$ increases (see Table 1) with increasing Ni content. Note that the Weiss temperature is more or less constant over the investigated concentration range, thus the increase of f is not due to an increasing Kondo effect, but an decreasing T_N only, either due to disorder or frustration.

In order to make a conclusion about the effect of Ni doping in the system, we compare the cell volume change by external pressure and by chemical pressure. We have estimated the bulk modulus for CePdAl from the bulk moduli of the pure constituents as described in Ref. [9] and calculated the cell volume for every pressure value from the work of Goto *et al* [4]. The cell volumes for the doped $\text{CePd}_{1-x}\text{Ni}_x\text{Al}$ samples were calculated from the X-ray diffraction data. The resulting pressure and doping diagram is shown in Fig. 3. It is seen that doping with Ni acts in the same way as applying hydrostatic pressure. The transition temperature T_N is suppressed both by applying hydrostatic and chemical pressure with essentially the same reduction of the cell volume.

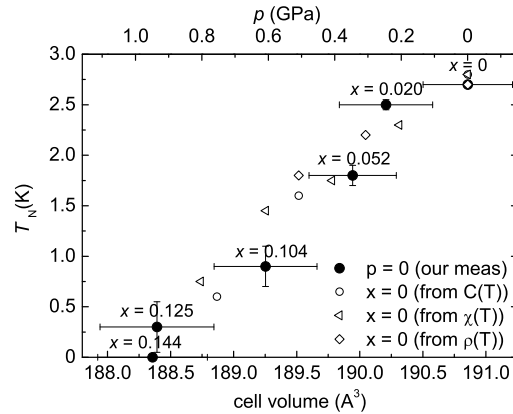


Figure 3: Pressure and doping diagram for $\text{CePd}_{1-x}\text{Ni}_x\text{Al}$ alloys. The data for CePdAl under pressure were calculated from data after Goto *et al* [3].

In this work the effect of chemical pressure on the substituted alloy $\text{CePd}_{1-x}\text{Ni}_x\text{Al}$ has been investigated systematically. The specific heat for a Ni concentration $x = 0.144$ shows a $C/T = a \ln(T_0/T)$ dependence compatible with the 2D AF Herz-Millis model of quantum criticality. Comparing effects of chemical and hydrostatic pressure, investigated by specific heat, allows us to conclude that T_N is suppressed by increasing frustration, not by disorder.

This work was supported by the DFG through FOR960.

- [1] A. Oyamada, K. Kamioka, K. Hashi, S. Maegawa, T. Goto, H. Kitazawa, J. Phys. Soc. Jpn. **65**, Suppl. B, 128 (1996).
- [2] A. Dönni, G. Ehlers, H. Maletta, P. Fischer, H. Kitazawa, and M. Zolliker, J. Phys.: Condens. Matter **8**, 11213 (1996), and references therein.
- [3] A. P. Ramirez, Annu. Rev. Mater. Sci. **24**, 453 (1994).
- [4] T. Goto, S. Hane, K. Umeo, T. Takabatake, and Y. Isikawa, Chem. of Solids, **63**, 1159 (2002).
- [5] Y. Isikawa, T. Mizushima, N. Fukushima, T. Kuwai, J. Sakurai, and H. Kitazawa, J. Phys. Soc. Jpn. **65**, Suppl. B, 117 (1996).
- [6] S. Hane, T. Goto, T. Abe, Y. Isikawa., Physica B **281-282**, 391 (2000).
- [7] J. A. Hertz, Phys. Rev. B **14**, 1165 (1976).
- [8] A. J. Millis, Phys. Rev. B **48**, 7183 (1993).
- [9] G. Grimvall, *Thermophysical properties of materials*. The Royal Institute of Technology, Stockholm, Sweden (1999).

¹Institut für Festkörperphysik, Karlsruhe Institut of Technology

Resistivity and magnetization measurements on doped and undoped barium iron pnictide

O. Berg, M. Marz, Th. Wolf¹, G. Goll and H. v. Löhneysen

We performed resistivity and magnetization measurements on doped and undoped barium iron pnictide single crystals to determine the magnetic and superconducting transition temperature, respectively [1]. We investigated three different samples BaFe_2As_2 , $\text{Ba}(\text{Fe}_{0.935}\text{Co}_{0.065})_2\text{As}_2$ and $\text{Ba}_{0.68}\text{K}_{0.32}\text{Fe}_2\text{As}_2$. The undoped and the Co-doped crystals were grown in FeAs flux, the K-doped crystal was grown in Sn flux. Resistivity measurements were done in the standard four-probe geometry in the temperature range $T = 1.5$ K to 300 K. Figure 1 shows the normalized resistivity for the three crystals. The normal-conducting parent compound

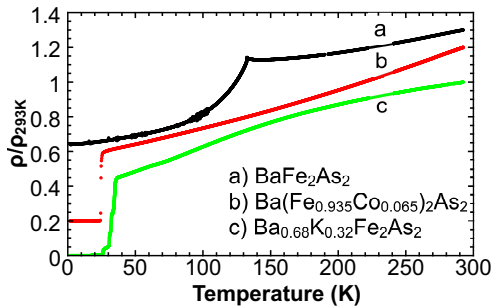


Figure 1: Normalized resistivity $\rho/\rho_{293\text{K}}$ vs. temperature T between 1.5 K and 300 K. a) The undoped parent compound BaFe_2As_2 shows an antiferromagnetic transition at $T_N = 132$ K. b) $\text{Ba}(\text{Fe}_{0.935}\text{Co}_{0.065})_2\text{As}_2$ undergoes a superconducting transition at $T_c = 24.5$ K. c) $\text{Ba}_{0.68}\text{K}_{0.32}\text{Fe}_2\text{As}_2$ becomes superconducting at $T_c = 32.3$ K. The curves a and b are shifted vertically for clarity.

BaFe_2As_2 (Fig.1 a) shows a single, well-defined and sharp transition at $T \approx 132$ K in the resistivity indicating that the magnetic and structural transitions coincide [2]. Both superconducting samples show no hints of a magnetic or structural transition in the resistivity. The superconducting transition temperature for the Co-doped sample (Fig.1 b) is $T_c = 24.5$ K with a very sharp step at the transition, with a temperature width between 10 and 90% of the normal-state resistivity of $\Delta T = 0.6$ K. The onset temperature of the superconducting transition of the K-doped sample is $T_c = 32.3$ K. However, the transition is strongly broadened with $\Delta T = 6.5$ K in this case. The much sharper transition of the Co-doped compound is the first evidence for the higher quality compared to the K-doped sample.

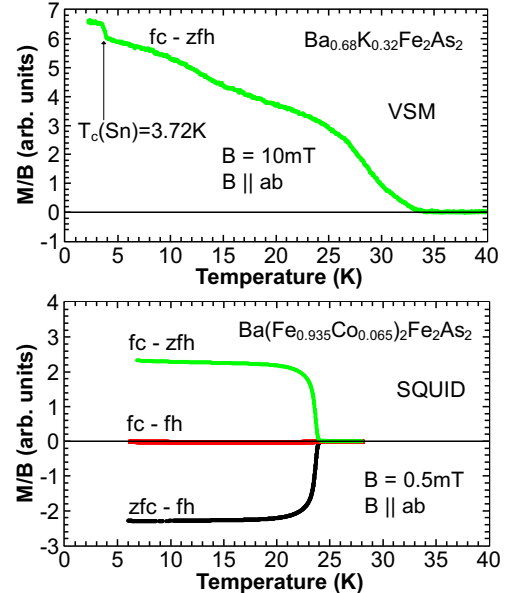


Figure 2: Magnetization $M(T)$ near the superconducting transition of the K- and Co-doped BaFe_2As_2 samples. The measurements on $\text{Ba}_{0.68}\text{K}_{0.32}\text{Fe}_2\text{As}_2$ (upper panel) were performed in a VSM in an applied field of $B = 10$ mT. The measurements on $\text{Ba}(\text{Fe}_{0.935}\text{Co}_{0.065})_2\text{As}_2$ (lower panel) were performed with a SQUID magnetometer in $B = 0.5$ mT.

The different degrees of sample quality are also visible in the magnetization measurements (Fig. 2). For the K-doped sample (upper panel), besides the very inhomogeneous transition starting at $T = 33$ K, a second superconducting transition due to elemental Sn is observed at $T = 3.7$ K. On the other hand, the transition of the Co-doped sample at $T_c = 24$ K is very sharp and no other signal occurs (lower panel). In both cases the Meißner signal is very small. The transition temperatures of both samples are in good agreement to the resistivity measurements and literature data [3, 4].

- [1] O. Berg, Diplomarbeit, Karlsruher Institut für Technologie (2009).
- [2] M. Rotter *et al.*, Phys. Rev. B **78**, 020503 (2008).
- [3] M. Rotter *et al.*, Ang. Chem. Int. Ed. **47**, 7949 (2008).
- [4] J.-H. Chu *et al.*, Phys. Rev. B **79**, 014506 (2009).

¹Institut für Festkörperphysik, Karlsruher Institut für Technologie, 76131 Karlsruhe.

Point-contact spectroscopy on doped and undoped 122 iron pnictides in the normal state

O. Berg, M. Marz, Th. Wolf¹, G. Goll, and H. v. Löhneysen

The discovery of superconductivity in iron pnictide LaOFeP has encouraged further research on iron based compounds [1]. A huge surprise was the critical temperature $T_c = 26$ K of F-doped LaOFeAs [2]. By now, iron arsenide superconductors have been firmly established as a second class of high- T_c superconductors, besides the cuprates. BaFe_2As_2 is another iron pnictide which becomes superconducting upon doping. The underdoped parent compound exhibits antiferromagnetic ordering at $T_N = 140$ K attributed to the formation of a spin-density wave with a concomitant structural distortion [3]. T_N is suppressed and superconductivity is observed upon doping on the Ba or Fe site [4, 5]. It is not yet fully understood if and how magnetic ordering and superconductivity coexist in doped iron-arsenide compounds.

We performed point-contact spectroscopic measurements to probe the 122 parent compound BaFe_2As_2 for possible excitations and to determine whether these excitations are affected or even suppressed by doping the crystal on the Ba site or the Fe site [6]. The differential conductance dI/dV vs. voltage V of $\text{BaFe}_2\text{As}_2/\text{Pt}$ point contacts with a point contact resistance of $R_0 = 17 \Omega$ has been measured in a bias range between $+60$ mV and -60 mV in the temperature range between 10 and 120 K. The data are shown in Fig. 1. Each curve is normalized to the value at $V = +60$ mV. For clarity the curves are shifted equidistantly.

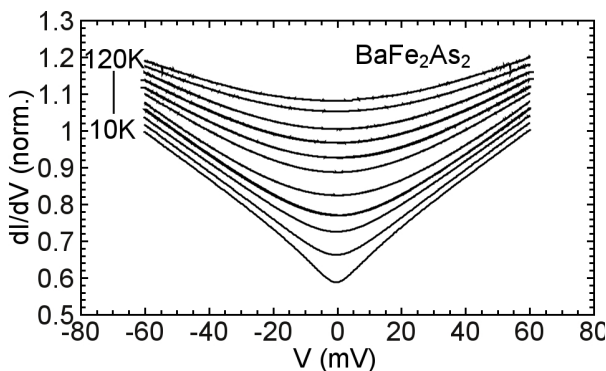


Figure 1: BaFe_2As_2 : Point-contact spectra dI/dV vs. voltage V measured in the thermal regime (17Ω) between $T = 10$ K and 120 K. The data are normalized to the value at 60 mV.

BaFe_2As_2 reveals a monotonic increase with increasing voltage. For the lowest temperature of 10 K, an almost linear increase of dI/dV with V is observed, with an increase between $V = 0$ and 60 mV by a factor of 1.7. With increasing temperature the distinct zero-bias minimum is progressively broadened. We can rule out heating effects as the origin of the observed structure since the differential conductance increases with the applied voltage whereas thermal heating due to the low contact resistance would cause a decreasing differential conductance. The increase of the conductance with increasing voltage is quite untypical for a metal. An associated feature is the increase of the zero-point conductance with temperature shown in Fig. 2. A possible origin of this unusual voltage and temperature dependence of the conductance may be found in the spin-density wave magnetic order and the associated opening of an energy gap on parts of the Fermi surface.

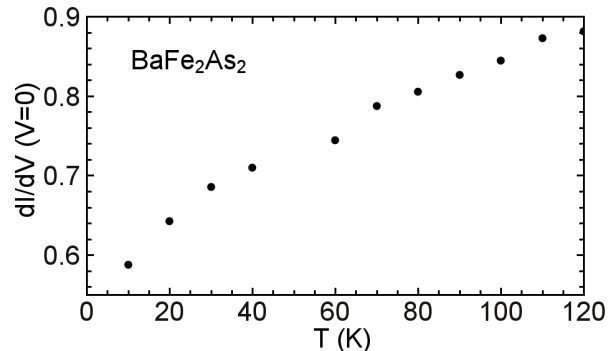


Figure 2: BaFe_2As_2 : Temperature dependence of the zero-bias conductance of the spectra shown in Fig. 1

In order to check this possibility, we performed corresponding measurements on K- and Co-doped BaFe_2As_2 . The spectra of a point contact (36Ω) of $\text{Ba}_{0.68}\text{K}_{0.32}\text{Fe}_2\text{As}_2$ for $T \geq T_c$ show only a shallow minimum in the differential conductance at zero bias. In contrast to the data for the undoped compound, the raw data exhibit a pronounced asymmetry with respect to V . Therefore, we determined the symmetric part of our measurements. These symmetric curves are displayed in Fig. 3.

Indeed, the amplitude of the change in dI/dV of the K-doped sample is a factor of about 20 smaller than for the undoped sample. This might suggest

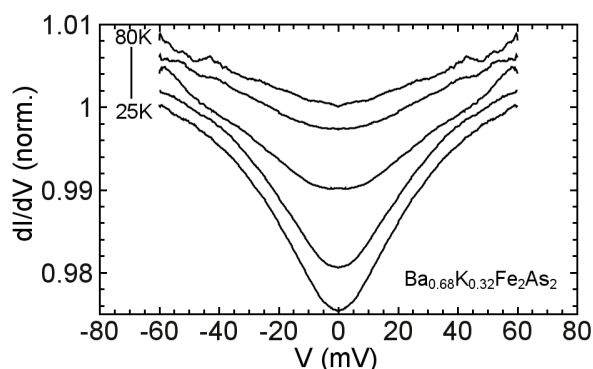


Figure 3: $\text{Ba}_{0.68}\text{K}_{0.32}\text{Fe}_2\text{As}_2$: Point-contact spectra dI/dV vs. voltage V measured in the thermal regime ($36\ \Omega$) between $T = 25\ \text{K}$ and $80\ \text{K}$. The data are normalized to the value at $60\ \text{mV}$.

that the strong features in the BaFe_2As_2 sample are indeed due to the opening of a gap due to the antiferromagnetic ordering.

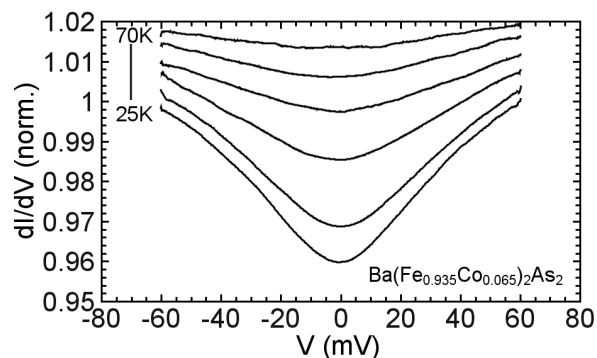


Figure 4: $\text{Ba}(\text{Fe}_{0.935}\text{Co}_{0.065})_2\text{As}_2$: Point-contact spectra dI/dV vs. voltage V measured in the thermal regime ($19\ \Omega$) between $T = 25\ \text{K}$ and $70\ \text{K}$. The data are normalized to the value at $60\ \text{mV}$.

This tentative assignment is corroborated by point-contact measurements on Co-doped $\text{Ba}(\text{Fe}_{0.935}\text{Co}_{0.065})_2\text{As}_2$ that reveal a similar behaviour as the K-doped one (see Fig. 4).

The fact that the doped samples $\text{Ba}_{0.68}\text{K}_{0.32}\text{Fe}_2\text{As}_2$ and $\text{Ba}(\text{Fe}_{0.935}\text{Co}_{0.065})_2\text{As}_2$ do not show such a strong temperature and voltage dependence of pure BaFe_2As_2 is readily explained by the fact that these compounds do not order antiferromagnetically, consistent with the general phase diagram of doped FeAs pnictide of the 122 family. Indeed, our K- and Co-doped samples are superconducting with $T_c = 32\ \text{K}$ and $24\ \text{K}$, respectively. Specifically, looking at the known phase diagrams of $\text{Ba}_{1-x}\text{K}_x\text{Fe}_2\text{As}_2$ and $\text{Ba}(\text{Fe}_{1-x}\text{Co}_x)_2\text{As}_2$, magnetic ordering is suppressed in our samples since the doping concentration of 32% at potassium on the one hand and 6.5% at cobalt on the other hand are in each case just above the critical concentration of antiferromagnetic ordering [7, 8]. More detailed investigations for other doping levels and in magnetic fields are underway.

- [1] Y. Kamihara *et al.*, J. Am. Chem. Soc. 128, 10012 (2006).
- [2] Y. Kamihara *et al.*, J. Am. Chem. Soc. 130, 3296 (2008).
- [3] M. Rotter *et al.*, Phys. Rev. Lett. 101, 107006 (2008).
- [4] M. Rotter *et al.*, Phys. Rev. B 78, 020503 (2008).
- [5] A. S. Sefat *et al.*, Phys. Rev. Lett. 101, 117004 (2008).
- [6] O. Berg, diploma thesis, 2009.
- [7] M. Rotter *et al.*, Angew. Chem. 47, 7949 (2008).
- [8] J.-H. Chu *et al.*, Phys. Rev. B 79, 014506 (2009).

¹ Institut für Festkörperphysik, Karlsruher Institut für Technologie, 76131 Karlsruhe

Point-contact spectroscopy on K-doped BaFe_2As_2 in the superconducting state

M. Marz, O. Berg, Th. Wolf¹, H. v. Löhneysen and G. Goll

The discovery of superconductivity in iron pnictide compounds [1] led to a novel class of high-temperature superconductors. They can be classified according to the stoichiometry of the parent compound in the (1111)-type, such as LaOFeAs , SmOFeAs etc., and the (122)-type, such as CaFe_2As_2 and BaFe_2As_2 . Electron and hole superconductivity occurs upon doping the parent compounds or under pressure. Both types show a superconducting transition in a comparable temperature range with maximal $T_c = 55$ K in SmOFeAs and $T_c = 38$ K in BaFe_2As_2 . In our point-contact experiments we found signatures that can be attributed to two-band superconductivity in both K- and Co-doped BaFe_2As_2 . Two-band superconductivity was discussed already in the early 1960s [2, 3], the first unequivocal experimental observation of this phenomenon was for MgB_2 in 2002 [4]. The situation with respect to the 122 iron pnictides is not very clear yet. Point-contact spectroscopy (PCS) indicate the presence of two nodeless gaps in K-doped BaFe_2As_2 , while Co-doped samples mostly exhibit broad features compatible with a single gap [5]. Recent measurements of the specific heat of Co-doped BaFe_2As_2 , on the other hand, give clear indication of two-band superconductivity as well [6].

The $\text{Ba}_{1-x}\text{K}_x\text{Fe}_2\text{As}_2$ ($x = 27.8\%$) single crystals were prepared in Sn flux, which results in a contamination with Sn, not only on the surface but also in the bulk where a small number of Sn atoms occupies Fe positions of the crystal lattice. Measurements on the electron-doped $\text{Ba}(\text{Fe}_{1-x}\text{Co}_x)_2\text{As}_2$ ($x = 8\%$) single crystals that were grown in FeAs flux show a higher sample quality with respect to the superconducting properties.

We performed resistance and magnetization measurements to determine the superconducting transition temperature and the quality of the different samples. We found the transition temperature with the 50% criteria to be $T_c = 26$ K for the K-doped crystals. The resistive transition between 90 and 10% of the normal-state value showed a relatively large broadening of $\Delta T_c = 4.4$ K for this sample. This hints at a rather large inhomogeneity in the samples, which was also clearly seen in the broad transition obtained in magnetization measurements. Co-doped samples showed the superconducting transition at $T_c = 22$ K. The transition is with $\Delta T_c = 1.5$ K much sharper than for the K-doped samples

(see [7] for details). Here we focus on the K-doped samples where we have investigated the anisotropy of PCS spectra.

The I - V -curves were obtained in a four-point geometry. dI/dV was measured using a lock-in technique, where a small ac signal ($\nu = 9.13$ kHz) was superposed to the dc bias. Measurements with $I \perp c$ were carried out with the 'edge to edge'-method [7]. Measurements with $I \parallel c$ were performed in the 'needle-anvil' geometry [8]. In all our measurements a Pt needle was used as normal-conducting counter electrode.

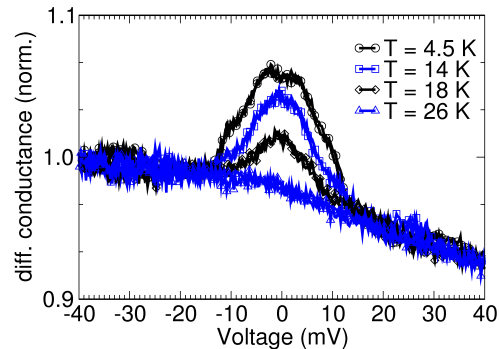


Figure 1: Differential conductance dI/dV vs. V for a K-doped BaFe_2As_2 / Pt point contact with $R = 25 \Omega$, $I \perp c$ for different temperatures.

The measurement in Fig 1 shows raw data of a point-contact experiment on the K-doped sample with I perpendicular to c . In general, the data for this sample exhibit a weak asymmetry. In the normal state at T_c , dI/dV shows a broad very shallow maximum at zero bias. In the superconducting state we observe around zero bias an increase of the differential conductance dI/dV between -15 and $+15$ mV with some internal structure. This structure can be interpreted as a second small maximum caused by the small gap on top of the broad maximum, both being due to the contribution of Andreev reflexion. To describe the data, this normal conducting background was subtracted, as shown in Fig. 2 and 4.

We used a modified BTK model to fit to the differential conductance in the superconducting state. For the fits we assume that the currents caused by Andreev reflection due to the two superconducting gaps Δ_1 and Δ_2 are independent of each other. Thus, the total conductance through the contact can be expressed as a weighted sum α , $0 < \alpha < 1$ as:

$$G_{\text{tot}}(V) = \alpha \cdot G_{\Delta_1}(V) + (1 - \alpha) \cdot G_{\Delta_2}(V).$$

We calculated the normalized conductance G_{Δ_i} for the individual gap Δ_i using the standard s-wave BTK-theory [9] including finite lifetime broadening modeled by a Dynes parameter Γ_i [10]. For the fitting procedure all measurements were normalized at the conductance for $V = -V_{\max}$. In addition, the normal conducting background was subtracted as previously mentioned. To accelerate the fitting procedure the data points were interpolated to use only 100 equidistant sampling points between $V = 0$ and $V = +30$ mV (out of total several hundred). The fit was performed for the lowest temperature by varying $\Delta_1, \Delta_2, \Gamma_1, \Gamma_2, \alpha$ as well as the barrier strengths z_1 and z_2 . With increasing temperature only the gap values were allowed to vary, all other parameters were kept constant, as the contact is not expected to change during one temperature sweep at low temperature. The result of the two-band fit for the data

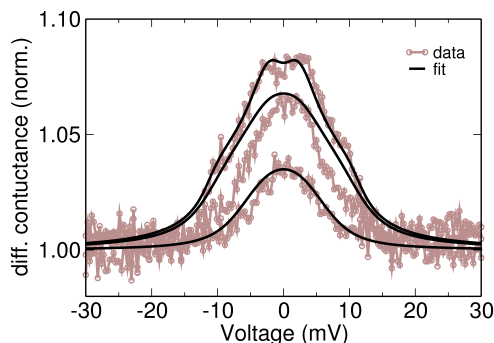


Figure 2: Best fits to the interpolated data of Fig. 1. The fits are calculated with a model to describe two-band superconductivity, details are given in the text.

shown in Fig. 1 is depicted in Fig. 2. The best fit is obtained for: $\Delta_1 = 15.19$ meV, $\Delta_2 = 1.55$ meV with $\Gamma_1 = 6.72$ meV, $\Gamma_2 = 2.25$ meV and $\alpha = 0.77$. The mean square deviation is $\chi^2 = 6 \cdot 10^{-6}$.

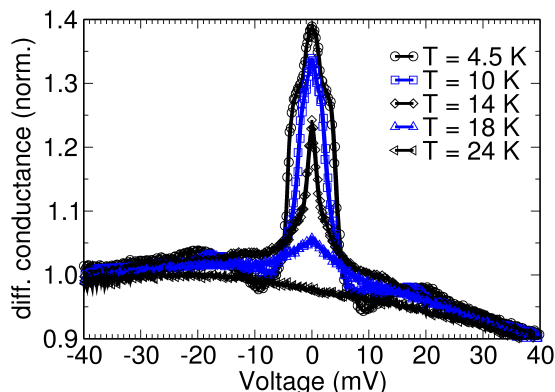


Figure 3: Differential conductance dI/dV vs. V for a point contact with $R = 48 \Omega$ and $I \parallel c$ for different temperatures.

Fig. 3 shows dI/dV for the same K-doped sample with I parallel to the c direction. Again, structure of the conductance enhancement around zero bias below T_c suggests the presence of two gaps. Note that here the enhancement amounts to maximally 40% as compared to maximally 8% only for I perpendicular to c . The fits to the data of Fig. 3 are shown in Fig. 4. In this case the parameters for the best fit are $\Delta_1 = 11.15$ meV, $\Delta_2 = 2.05$ meV with $\Gamma_1 = 1.39$ meV, $\Gamma_2 = 3.00$ meV and $\alpha = 0.95$, with $\chi^2 = 5 \cdot 10^{-5}$.

In conclusion, we have observed subgap structures

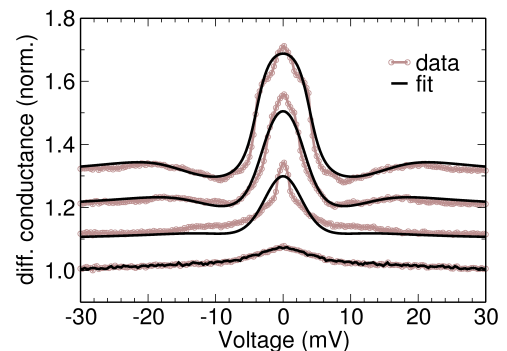


Figure 4: Best fits to the data in Fig. 3 with the two-band model for the interpolated data.

in point-contact spectroscopy in K-doped BaFe_2As_2 supporting the existence of two gaps. In addition, a distinct directional dependence of Andreev reflection hints at a strong gap anisotropy. This gap anisotropy is inferred from the difference of both the strength of the Andreev-reflection signal and the relative weight α of the two gaps with respect to the directions parallel and perpendicular to c .

- [1] Y. Kamihara *et al.*, J. Amer. Chem. Soc. **128**, 10012 (2006).
- [2] H. Suhl *et al.*, Phys. Rev. Lett. **3**, 12 (1959).
- [3] N. Schopohl *et al.*, Solid State Comm. **22**, 371 (1977).
- [4] A. Jounod *et al.*, Studies of High Temperature Superconductors **19**, 1 (2002).
- [5] P. Samuely *et al.*, Physica C **469**, 507 (2009).
- [6] F. Hardy *et al.*, Phys. Rev. B **81**, 060501(R) (2010).
- [7] O. Berg *et al.*, in this Annual Report.
- [8] F. Laube *et al.*, Phys. Rev. Lett. **84**, 1595 (2000).
- [9] G. Blonder *et al.*, Phys. Rev. B **25**, 4515 (1982).
- [10] R. Dynes *et al.*, Phys. Rev. Lett. **53**, 2437 (1984).

¹Institut für Festkörperphysik, Karlsruher Institut für Technologie, 76131 Karlsruhe.

High-pressure magnetization measurements on Co-doped BaFe₂As₂

S. Drotziger, K. Grube ¹, Th. Wolf ¹, P. Adelmann ¹, C. Meingast ¹, H. v. Löhneysen

Magnetic order in metals can be suppressed to zero temperature at a so-called quantum phase transition by non-thermal control parameters, e. g., hydrostatic pressure p or chemical composition x . Various experimental investigations report novel phases, e.g., superconductivity, emerging near a magnetic quantum phase transition.

Superconductivity in close proximity to long-range magnetic order was recently discovered in the iron pnictides [1]. One class of these new materials, the 122 compounds, show the same tetragonal ThCr₂Si₂ ($I4/mmm$) crystal structure as the heavy-fermion superconductor CeCu₂Si₂. Superconductivity in the 122 compounds was found in BaFe₂As₂ when Ba was partly substituted by K [2]. The parent compound BaFe₂As₂ shows spin-density-wave antiferromagnetic order at $T_N = 140$ K and a structural phase transition at $T^* \approx T_N(x = 0)$ to orthorhombic $Fmmm$. With increasing K content, T_N and T^* are suppressed to lower temperatures and superconductivity appears. It is commonly believed that the pairing mechanism is based on magnetic fluctuations due to the vicinity to the spin-density-wave instability. The structural element that carries superconductivity are Fe₂As₂ layers separated by Ba atoms. The charge carrier concentration within these layers is assumed to be the crucial parameter to control physical properties as the K substitution introduces holes into the system [2] in analogy to oxygen doping in the YBa₂Cu₃O _{x} cuprates [3]. Due to the proposed magnetic pairing mechanism it was expected that disorder should have an enormous effect on the superconducting order, especially if the gap shows point or line nodes. Surprisingly, the partial substitution of Co on Fe sites also induces superconductivity in BaFe₂As₂ [4], although Co is implemented into the Fe₂As₂ layers.

The fact that superconductivity can be induced in undoped BaFe₂As₂ by hydrostatic pressure suggests that, in addition to the charge carrier concentration, distinct bond lengths and angles have to be taken into account. As the application of pressure does not induce disorder in contrast to substitution, we investigated the p dependence of the superconducting transition temperature of Ba(Fe_{1- x} Co _{x})₂As₂ single crystals with $x = 0.041$ and 0.075 by temperature dependent magnetization measurements to disentangle the effects of doping, structural changes and disorder. Results on the compound with the nominal Co

concentration of $x = 0.075$ have been shown in a previous report [5].

Ba(Fe_{1- x} Co _{x})As₂ single crystals were grown with a self-flux method in an alumina crucible [6]. The Co content was determined by a XPS microprobe analysis [7]. A SQUID magnetometer (Quantum Design) was used to characterize the crystals at $p = 0$. From these crystals smaller samples with typical dimensions of $50 \mu\text{m} \times 50 \mu\text{m} \times 20 \mu\text{m}$ have been cut for our high-pressure magnetization measurements in a miniaturized diamond anvil cell up to $p = 4.3$ GPa [5]. The magnetization M was measured in a vibrating sample magnetometer at temperatures down to 2.3 K. For all measurements a magnetic field of $B = 5$ mT was applied along the c axis. We measured the diamagnetic shielding and the Meissner effect by

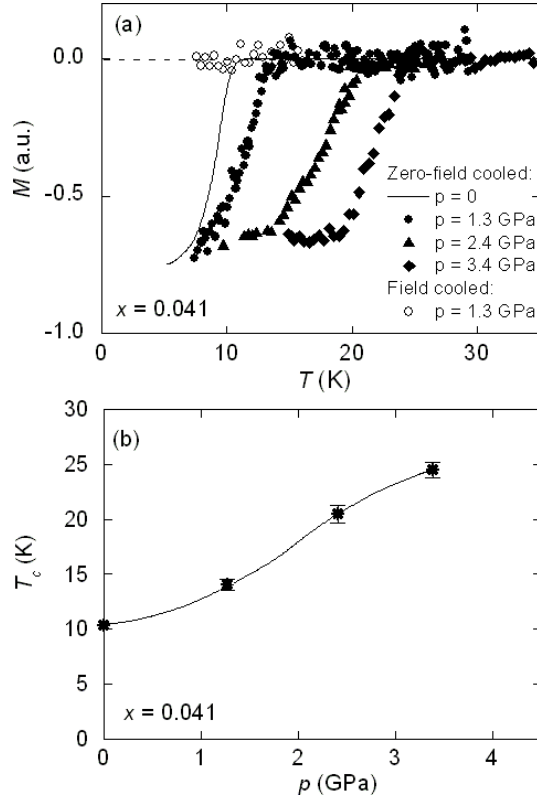


Figure 1: (a) $M(T)$ of Ba(Fe_{1.959}Co_{0.041})As₂ for $p \leq 3.4$ GPa. ZFC curves are shown for $p = 1.3$ GPa. FC curves are indicated by open symbols. (b) T_c as a function of $p \leq 3.4$ GPa in Ba(Fe_{1.959}Co_{0.041})As₂. The black line serves as guide to the eye.

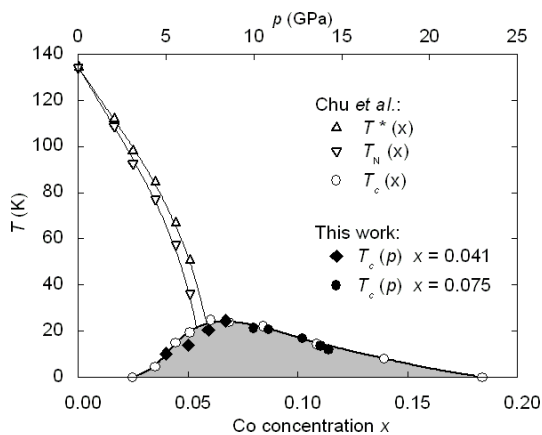


Figure 2: Comparison between the p and x dependence of T_c in $\text{Ba}(\text{Fe}_{1-x}\text{Co}_x)_2\text{As}_2$.

subsequent zero-field-cooled (ZFC) and field-cooled (FC) magnetization measurements, respectively.

Fig. 1 (a) shows $M(T)$ of $\text{Ba}(\text{Fe}_{1.959}\text{Co}_{0.041})\text{As}_2$ for p up to 3.4 GPa. The Meissner-Ochsenfeld effect (FC curves, open symbols) is invisible in our measurements, whereas the pronounced diamagnetic shielding, observed in all ZFC measurements, reveals bulk superconductivity. This large difference is usually related to strong pinning. The superconductivity of the $x = 0.041$ sample appears at ambient pressure for $T_c^{\text{onset}} \approx 11$ K as it is displayed in Fig. 1 (black line). With increasing pressure T_c^{onset} is shifted to higher temperatures and the transition broadens. The pressure dependence of T_c^{onset} is summarized in Fig. 1 (b).

The phase diagram of $\text{Ba}(\text{Fe}_{1-x}\text{Co}_x)_2\text{As}_2$ is shown in Fig. 2. The open symbols indicate $T_c(x)$ and $T_N(x)$ measured by Chu *et al.* [8]. The magnetic order vanishes approximately at a Co concentration corresponding to the maximum T_c . To compare the effect of pressure and concentration we included the $T_c(p)$ values of the $x = 0.041$ and 0.075 samples by using a conversion factor of $\Delta x/\Delta p = 0.0084/1$ GPa, cf., upper and lower horizontal axis. Surprisingly, all data points collapse on a single phase line, demonstrating that pressure and Co doping when properly scaled have the same effect on the superconducting order. Obviously, the disorder generated by Co doping has no influence on the superconducting state of $\text{Ba}(\text{Fe}_{1-x}\text{Co}_x)_2\text{As}_2$. This is an astonishing result as disorder usually suppresses unconventional superconductivity. For example, in the presumed p -wave superconductor Sr_2RuO_4 and the d -wave cuprate superconductor $\text{YBa}_2\text{Cu}_3\text{O}_x$ a high sensitivity to impurities and lattice defects is observed [9, 3]. In the latter even tiny amounts of Zn within the CuO_2 planes completely destroy superconductivity. Hence,

the insensitivity to disorder in the superconducting Fe_2As_2 layers is a strong indication for s -wave superconductivity.

Furthermore, the similar concentration and pressure dependences of T_c suggest that structural changes alone are sufficient to generate superconductivity. The significance of structural effects is supported by measurements on Cr doped BaFe_2As_2 where no superconductivity is observed, although Cr does induce charge carriers into the FeAs layers [10]. To clarify which structural changes are responsible for superconductivity in BaFe_2As_2 further investigations of the crystal structure as a function of p and x are necessary.

We acknowledge financial support in the framework of the Virtual Institute on Research on Quantum Phase Transitions (VIRQ VH-VI-127) and the DFG Research Unit Quantum Phase Transitions (FOR 960).

- [1] Y. Kamihara, T. Watanabe, M. Hirano, H. Hosono, *J. Am. Chem. Soc.* **130**, 3296 (2008).
- [2] M. Rotter, M. Tegel, D. Johrendt, *Phys. Rev. Lett.* **101**, 107006 (2008).
- [3] B. Jayaram, S. K. Agarwal, C. V. Narasimha Rao, A. V. Narlikar, *J. Alloys Comp.* **38**, 2903 (1988).
- [4] X. F. Wang, T. Wu, G. Wu, H. Chen, R. H. Liu, H. Chen, Y. L. Xie, X. H. Chen: arXiv:0811.2920 (2008).
- [5] S. Drotziger, K. Grube, Th. Wolf, H. v. Löhneysen, Annual report, Physikalisches Institut, Universität Karlsruhe (2008).
- [6] F. Hardy, P. Adelmann, H. v. Löhneysen, Th. Wolf, C. Meingast, *Phys. Rev. Lett.* **102**, 187004 (2009).
- [7] With this measurement the exact Co concentration of the sample reported in [5] was identified to be $x = 0.075$.
- [8] J. Chu, J. G. Analytis, C. Kucharczyk, I. R. Fisher, *Phys. Rev. B.* **79**, 14506 (2008).
- [9] A. P. Mackenzie, R. K. W. Haselwimmer, A. W. Tyler, G. G. Lonzarich, Y. Mori, S. Nishizaki, Y. Maeno, *Phys. Rev. Lett.* **80**, 161 (2007).
- [10] A. S. Sefat, D. J. Singh, L. H. VanBebber, Y. Mozharivskyj, M. A. McGuire, R. Jin, B. C. Sales, V. Keppens, D. Mandrus, *Phys. Rev. B.* **79**, 224524 (2009).

¹ Karlsruher Institut für Technologie (KIT), Institut für Festkörperphysik, Germany

Rabi spectroscopy of a strongly driven qubit-TLS system

J. Lisenfeld, C. Müller¹, J. H. Cole², P. Bushev, A. Lukashenko, A. Shnirman¹, and A. V. Ustinov

Spectroscopic analysis of superconducting qubits often shows clear signatures of avoided level crossings, indicating the presence of microscopic two-level systems (TLSs) that can be in resonance with the qubit. This resonant interaction allows to study the properties of individual TLSs by using a qubit to control and read-out their quantum states. Often, it is found that the coherence time of a TLS exceeds that of the macroscopic qubit, which makes them very interesting for quantum information processing. However, if the state of the TLS is controlled by resonant qubit interaction, the fidelity of quantum gates is limited by the short qubit coherence times. In this work we show that an effective direct coupling of the TLS to the external microwave exists. This allows to control the TLS's quantum state directly without involving short-living excited states of the comprising qubit.

The qubit we were using is a phase qubit 1, consisting of a Josephson tunnel junction shunted by both an overlap capacitor and a superconducting inductor to create an (nonlinear) LC - resonant circuit. A schematic of the circuit is shown in Fig. 1 (a). Microscopic TLSs are currently understood as nanoscale dipoles emerging from metastable lattice configurations in the amorphous dielectric [2] which constitutes the tunnel barrier of the qubit's Josephson junction or its shunting capacitor, see Fig. 1 (b) and (c). A switching between different charge configurations is possible even at low temperatures by quantum tunneling, and such an atomic-scale charge displacement can be associated with the creation of an electrical dipole. Thus, a TLS couples to the electrical field of the qubit, which oscillates at the qubit frequency.

For the qubit states, one uses the two Josephson phase eigenstates of lowest energy which are localized in a shallow potential well (see inset to Fig. 2), whose depth is controlled by the external magnetic flux through the qubit loop. The states are distinguished by the tunneling rate through the potential barrier, which is much larger from state $|1\rangle$ than from state $|0\rangle$. This tunneling results in a change of the flux in the qubit loop, which is detected by an inductively coupled DC-SQUID. The qubit state is controlled by an externally applied microwave pulse, which in our sample is coupled capacitively to the Josephson junction. Details of the experimental setup can be found in Ref. [3].

Spectroscopic data taken in the whole accessi-

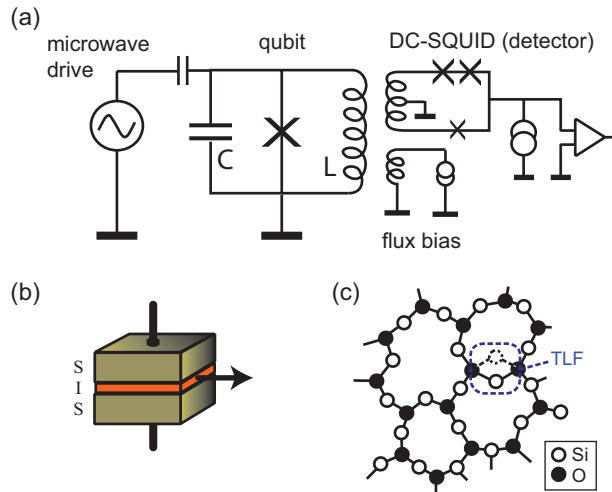


Figure 1: (a) Schematic of the phase qubit circuit. (b) Model of a Josephson junction. (c) Model of two-level states in an amorphous oxide.

ble frequency range between 5.8 GHz and 8.1 GHz showed only 4 avoided level crossings due to TLSs having a coupling strength larger than 10 MHz. In this work, we studied the qubit interacting with a fluctuator whose energy splitting was $\epsilon_f/h = 7.805$ GHz. From its spectroscopic signature, we extract a coupling strength $v_{\perp}/h \approx 25$ MHz. Direct measurements of the coherence times of this TLS indicate $T_{1,f} \approx 850$ ns and $T_{2,f} \approx 110$ ns.

Experimentally, we observe the probability $P(|e\rangle)$ of the qubit being in its excited state after driving it resonantly with a short microwave pulse of varying duration. If the energy splitting of the qubit is tuned far away from that of the fluctuator, the qubit remains decoupled from the TLS and $P(|e\rangle)$ displays the usual Rabi oscillations. If, in contrast, the qubit is tuned close to the resonance frequency of the TLS, the probability to measure the excited qubit state shows a complicated time dependence, which is very sensitive to the chosen qubit bias.

Figure 3(a) shows a set of time traces of $P(|e\rangle)$ taken for different microwave drive frequencies. The Fourier-transform of this data is shown in Fig. 3(b). We note a striking asymmetry between the Fourier components appearing for positive and negative detuning of the qubit relative to the TLS's resonance frequency, which is indicated in Figs. 3(a,b) by the

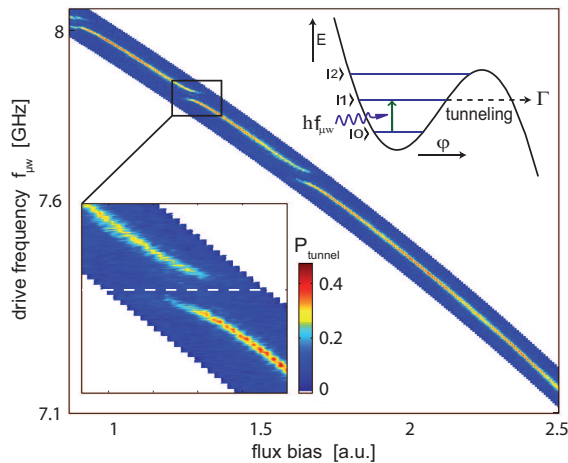


Figure 2: Spectroscopic data showing an increase in the tunnel probability (color-coded) when the applied microwave frequency matches the qubit's transition frequency. The zoom emphasizes an avoided-level crossing due to a TLS. Inset: potential of the phase qubit indicating the first three energy levels and the resonant photon absorption process.

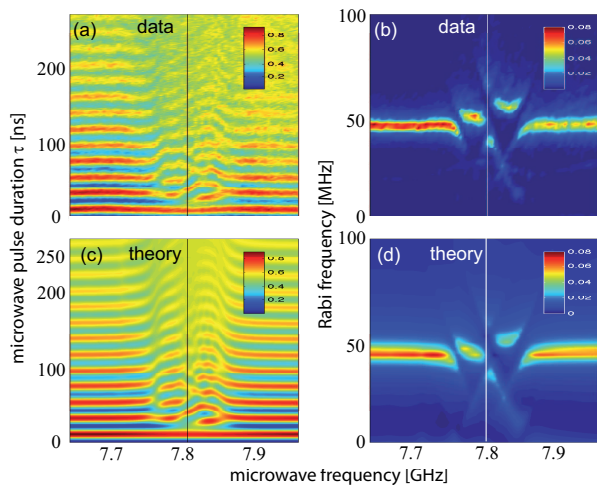


Figure 3: (color online) **(a)** Rabi oscillation of the qubit's excited state population probability and **(b)** its Fourier-transform, both plotted vs. driving frequency. **(c)** Numerical solution of the driven qubit-TLS system in the time domain and **(d)** its Fourier-transform, reproducing the asymmetric foot-print of the TLS interacting with the qubit. The resonance frequency of the TLS is indicated by vertical lines.

vertical lines at 7.805 GHz. Theoretical analysis gives strong indication that this asymmetry is due to virtual Raman-transitions involving higher levels in the qubit.

We identify three possible mechanisms which could break the symmetry: (i) Longitudinal coupling between qubit and TLS. In the case of a dipole coupling of TLS to the electric field of the qubit, this term would necessitate a constant electric field across the junction and is therefore not present. If, however, the TLS couples via a change in the critical current to the qubit, this coupling might indeed be strong. However such coupling was ruled out spectroscopically in Ref. [4] as well as by our preliminary spectroscopic data. (ii) Direct coupling of the TLS to the external field. Due to the presumably small size of the TLS this coupling should be negligible. (iii) Effective coupling of the TLS to the external driving field due to a second order Raman-like process in which the next higher level of the qubit $|2\rangle$ is virtually excited followed by a mutual flip of the TLS and the qubit. This gives an effective coupling of the TLS to the driving field which is only present when the qubit is (virtually) excited.

To fully describe the experiment, we include decoherence in our calculations by solving the time evolution of the system's density matrix using a standard Lindblad-approach. The theoretical spectral response of the system obtained by solving the dynamical equations is shown in Fig. 3(c, d). This calculation quantitatively reproduces the data without additional fit parameters.

We would like to thank M. Ansmann and J. M. Martinis (UCSB) for providing us with the sample that we measured in this work. This work was supported by the CFN of DFG, the EU projects EuroSQIP and MIDAS, and the US ARO Contract W911NF-09-1-0336.

- [1] R. W. Simmonds et. al., Phys. Rev. Lett. **93**, 077003 (2004)
- [2] P. Esquinazi (Ed.), *Tunneling Systems in Amorphous and Crystalline Solids* (Springer Verlag, 1998).
- [3] J. Lisenfeld, A. Lukashenko, M. Ansmann, J.M. Martinis, and A.V. Ustinov, Phys. Rev. Lett. **99**, 170504 (2007)
- [4] A. Lupascu, P. Bertet, E.F.C.Driessen, C.J.P.M. Harmans, and J.E.Mooij, Phys. Rev. B **80**, 172506 (2008)

¹ Institut für Theorie der Kondensierten Materie, Karlsruhe Institute of Technology

² Institut für Theoretische Festkörperphysik, Karlsruhe Institute of Technology

Implementation of superconductor-ferromagnet-superconductor π -shifters in superconducting quantum circuits

A. K. Feofanov, V. A. Oboznov¹, V. V. Bol'ginov¹, J. Lisenfeld, S. Poletto,
A. N. Rossolenko¹, V. V. Ryazanov¹ and A. V. Ustinov

In superconducting circuits, currents can flow without applying any electric field. The role of the electrostatic potential difference required to drive a current in conventional circuits is played here by a difference φ between the phases of the superconducting order parameters of the electrodes. In the absence of current, φ is zero. This fundamental property can be altered by inserting a particular type of superconducting weak link, a so-called π -junction [1,2] yielding a phase shift of π . We demonstrate the operation of a π -biased phase qubit, which utilises a π -phase shifter realised using superconductor-ferromagnet-superconductor sandwich technology [3]. We observe coherent Rabi oscillations and find no degradation of the measured coherence time compared to that of a conventional superconducting phase qubit.

The fundamental property of superconducting weak links is a 2π -periodic current-phase relation. The supercurrent through a conventional Josephson junction is usually described by the harmonic relation $I_s = I_c \sin \varphi$, where I_c is the critical current. The so-called Josephson π -junction has the inverse current-phase relation $I_s = I_c \sin(\varphi + \pi) = -I_c \sin \varphi$. Embedding a π -junction into a superconducting loop leads to self-biasing of the loop by a spontaneously induced supercurrent. Providing the π -junction critical current I_c is chosen to be much larger than that of conventional 0-junctions employed in the very same loop, the phase difference across the π -junction is always close to π even at zero magnetic field.

The usage of π -junctions as passive phase shifters offers an advantage for the operation of superconducting flux qubits at the degeneracy point requiring zero or a very small external magnetic field. Potentially, this allows noise and electromagnetic interference induced by magnetic field sources to be minimised. The answer to the question of whether or not π -junctions can become useful in superconducting circuits designed for quantum computing applications depends on their impact on the coherence properties of the qubits. Potential sources of decoherence introduced by π -junctions can for instance be spin-flips in the ferromagnetic barrier, either occurring randomly or being driven by high-frequency currents

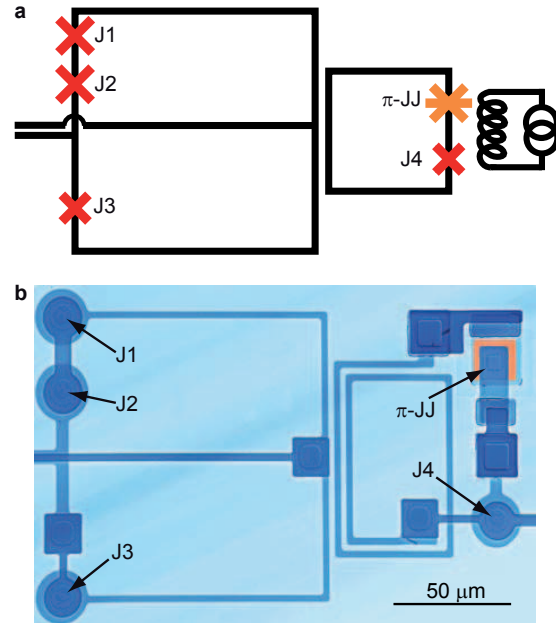


Figure 1: Self-biased phase qubit. **a**, Schematic of a phase qubit circuit used to test the decoherence properties of the π -junction. The qubit is realised by the central loop with embedded conventional and π -Josephson junctions. The larger loop to its left is a DC-SQUID for qubit readout. A current-biased coil coupled weakly to the qubit is used for flux-biasing the qubit. **b**, SEM picture of the realised phase qubit employing a π -junction in the qubit loop. The qubit flux-biasing coil is not shown for clarity.

and fields, as well as the dynamic response of the magnetic domain structure. We address these important coherence issues in an experiment, in which we use an SFS π -junction to self-bias a superconducting phase qubit. We have chosen here a phase qubit [4] rather than a flux qubit [5] due to the simpler fabrication procedure for the former. The results reported below would nevertheless remain fully applicable to flux qubits.

A phase qubit [4] consists of a single Josephson junction embedded in a superconducting loop. It is magnetically biased close to an integer number of flux quanta in the loop. At such a bias, the potential

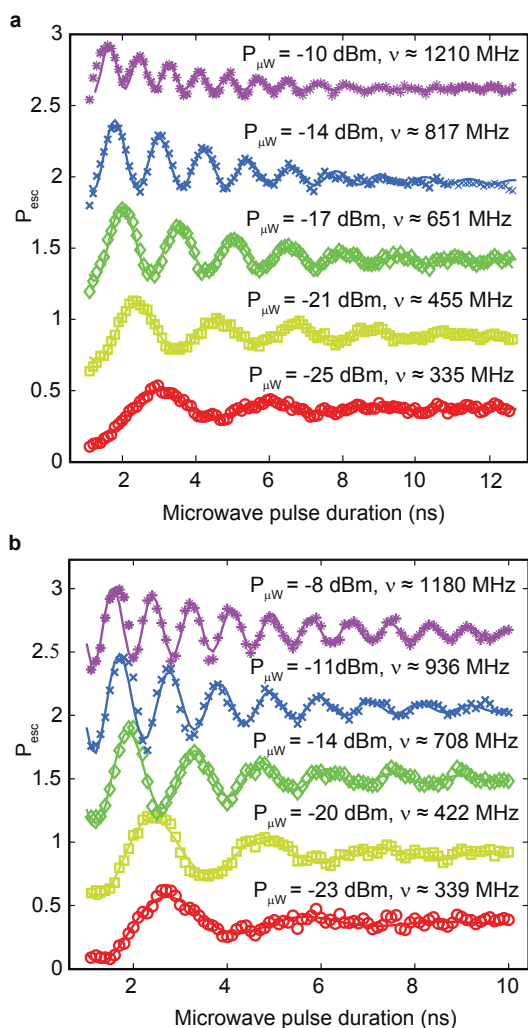


Figure 2: Rabi oscillations between the ground and the excited qubit states resulted from resonant microwave driving. **a**, Observed in the phase qubit with embedded π -junction, and **b**, A conventional phase qubit made on the same wafer as a reference. Each data set was taken using the indicated microwave power as delivered by the generator, giving rise to a change in the coherent oscillation frequency as expected for Rabi oscillation.

energy of the qubit exhibits an asymmetric double-well potential, whereas two quantised energy eigenvalues of the phase localised inside the shallow well only are used as the logical qubit states $|0\rangle$ and $|1\rangle$. Figure 1(a) shows a circuit schematic and 1(b) a micrograph of the tested sample. Here, a π -junction is connected in series to the phase qubit's tunnel junction. Coherent qubit operation is demonstrated by the data reported in Fig. 2(a), showing Rabi oscillation of the excited qubit state popula-

bility in dependence on the duration of a resonant microwave pulse. The oscillations exhibit a decay time of about 4 ns, which is a typical value reachable in samples fabricated using similar fabrication processes [6]. To find out whether π -junction does introduce additional decoherence, a conventional phase qubit without a π -junction was fabricated on the same wafer. As shown in Fig. 2(b), this reference qubit shows a nearly identical decay time for Rabi oscillations, allowing us to conclude that at least on the observable time scale no extra decoherence is introduced by the SFS π phase shifter employed in this circuit and that the decoherence in both qubits is limited by some other mechanism.

We compared the measured decoherence time with the theoretical predictions [7]. We assume here an *overdamped* SFS π -junction having a normal resistance of $R_{N,\pi} \approx 500 \mu\Omega$ and a critical current $I_{C,\pi} \approx 50 \mu A$. In our case, the qubit level splitting $\Delta \gg 2eI_{C,\pi}R_{N,\pi}$, where $\Delta \approx h \cdot 13.5$ GHz, h is the Planck's constant and e is the elementary charge. Here, the energy $2eI_{C,\pi}R_{N,\pi} \approx h \cdot 12$ MHz is associated with characteristic Josephson frequency of our SFS π -junction. Simplifying the expression for the relaxation time [7] in this limit, we can theoretically estimate the relaxation time τ_{relax} as

$$\tau_{\text{relax}} \approx \frac{\Delta}{2I_C^2 R_{N,\pi}} \approx 2 \text{ ns}. \quad (1)$$

Here, $I_C \approx 2 \mu A$ is the critical current of the small SIS qubit junction. The estimated value of the energy relaxation time is in good agreement with the measured decoherence time. We note, however, that the relaxation time (1) can be significantly enhanced by using SFS junctions with a smaller resistance $R_{N,\pi}$.

- [1] Bulaevskii, L. N., Kuzii, V. V. & Sobyenin, A. A. *JETP Lett.* **25**, 290-294 (1977).
- [2] Buzdin, A. I., Bulaevskij, L. N. & Panyukov, S. V. *JETP Lett.* **35**, 178-180 (1982).
- [3] Ryazanov, V. V. *et al.* *Phys. Rev. Lett.* **86**, 2427-2430 (2001).
- [4] Simmonds, R. W. *et al.* *Phys. Rev. Lett.* **93**, 077003 (2004).
- [5] Chiorescu, I., Nakamura, Y., Harmans, C. J. P. M. & Mooij, J. E. *Science* **299**, 1869-1871 (2003).
- [6] Lisenfeld, J., Lukashenko, A., Ansmann, M., Martinis, J. M. & Ustinov, A. V. *Phys. Rev. Lett.* **99**, 170504 (2007).
- [7] Kato, T., Golubov, A. A. & Nakamura, Y. *Phys. Rev. B* **76**, 172502 (2007).

¹ Institute of Solid State Physics, Russian Academy of Science, Chernogolovka, 142432, Russia

Two-photon spectroscopy of the hybrid quantum system

P. Bushev, C. Müller¹, J. Lisenfeld, J. Cole², A. Lukashenko, A. Shnirman¹ and A. V. Ustinov

The Dipole-dipole (DD) interaction is one of the most fundamental interactions in nature, underlying such diverse effects as Fluorescence-Resonance-Energy-Transfer (FRET) [1], Super- and Sub-Radiance and dipole blockade. Despite the progress in optics in observing and utilizing the effects based on DD-coupling in dense media or in molecular and atomic ensembles, there are only very few experiments where it was possible to probe *individual* quantum optical systems. The main experimental constraint in conventional quantum optics is the difficulty in bringing two atoms sufficiently close together to induce electrostatic interactions (distances less than an optical wavelength). This constraint is easily overcome in the emerging field of superconducting circuit QED [2] where the artificial “atoms” can be placed “at will” (on the scale of a wavelength) to obtain the regime of very strong coupling.

In our experiment we survey a system in a regime where both the “atom”-“atom” coupling and the driving field are strong. We study a superconducting phase qubit, consisting of a single Josephson Junction (JJ) embedded in a superconducting loop. For details on the experimental setup please refer to Ref. [3]. The results we present are from spectroscopic measurements of the qubit. In spectroscopy the steady-state of the system under driving is probed. It is performed by applying a microwave pulse for a sufficiently long time (here $\sim 2\mu s$) and then reading out the state of the system. Doing this as a function of microwave frequency and flux bias, we can map out the possible transitions into excited states, see Fig. 1. At this figure we present the spectroscopic results for the system when irradiated with a relatively low microwave power, corresponding to a Rabi-frequency of the qubit of about $\Omega_q = 4$ MHz. Near resonance with the TLS $\omega_{01} \approx \omega_f = 7.845$ GHz we see the characteristics of an anticrossing, indicating the coupling between qubit circuit and the TLS. The strength of the coupling v can be inferred from the size of the anticrossing exactly in resonance $\omega_{01} = \omega_f$. In this case, in the coupled system of qubit circuit and TLS, there are two degenerate states, $|1g\rangle$ and $|0e\rangle$. Due to the coupling, the degeneracy is lifted, and the system forms the eigenstates $|1\pm\rangle = 1/\sqrt{2}(|1g\rangle \pm |0e\rangle)$, which are separated in energy by the coupling v .

In the middle of the anticrossing, an additional line can be seen. From its power-dependence (Fig. 1, Inset) as well as its dependence on the bias point of the qubit, we can identify this line as a 2-photon

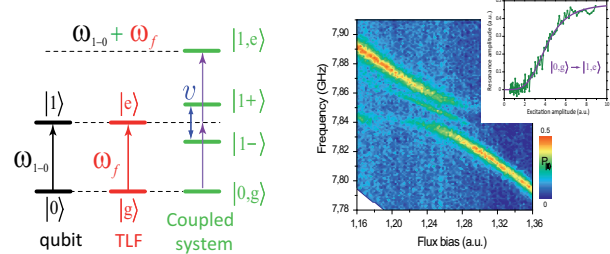


Figure 1: Quantum levels of coupled qubit-TLF system and transitions. The excitation spectrum of the qubit. Inset: amplitude dependence of the two-photon transition.

$|0g\rangle \leftrightarrow |1e\rangle$ transition of the coupled system. To verify this conclusion, we measured the power dependence of the amplitude of the middle peak. At low microwave power, when the Rabi frequency of the qubit Ω_q is much less than its linewidth ~ 7 MHz we observe a single anti-crossing. At higher excitation level, the additional peak appears and its amplitude saturates at very high power. The curve is well fitted with a $\sim V^4/(1+V^4)$ dependence (solid violet line), where V is proportional to the driving amplitude, thus corresponding to the absorption of two microwave photons.

The data shows the extremely high level of control that is possible in modern superconducting quantum systems, while also shedding light on the interaction with a intrinsic, microscopic two-level system. Understanding of the nature of TLS is crucial for the further improving the operation of solid state quantum bits.

[1] T. Förster, *Modern Quantum Chemistry* (Academic Press, New York, 1996).

[2] M. Devoret et al., *Ann. Phys.* **16**, 767 (2007)

[3] J. Lisenfeld et al., *Phys. Rev. Lett.* **99**, 170504 (2007)

¹ Institut für Theorie der Kondensierten Materie, Karlsruhe Institute of Technology

² Institut für Theoretische Festkörperphysik, Karlsruhe Institute of Technology

Observation of a dissipative dynamics in a strongly coupled TLS-qubit system

G. J. Grabovskij, P. Bushev, J. Lisenfeld, A. Lukashenko, and A. V. Ustinov

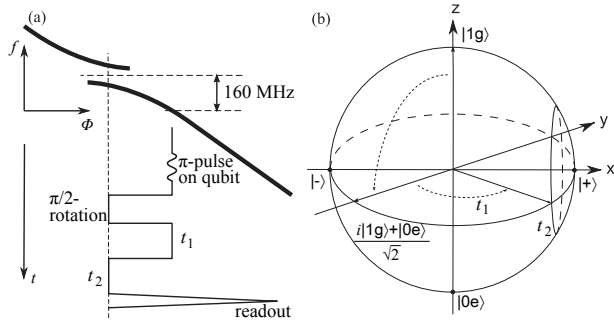


Figure 1: (a) Pulse sequence and sketch of excitation spectrum with a level anti-crossing. (b) Bloch sphere of the coupled system and its corresponding states.

The coherent control of the individual and coupled quantum systems is a topic of a great interest because of many possibilities of its application to quantum information processing. The ways of controlling the decoherence of the coupled systems are of particular importance as they constitute basic elements of a quantum processor [1].

In this brief report we present experiments on interaction of a Josephson phase qubit with a microscopic two-level-system (TLS) embedded in its oxide tunnel barrier. We outline our first experiments on creation of decoherence-protected states of a coupled qubit-TLS system. As it has been already shown TLS-qubit forms a coupled system [2] resembling coherent interaction between effective dipoles similar to the case of two atoms. This type of coupling could lead to cooperative effects such as super- and sub-radiance [3], when coupled system is prepared in symmetric and anti-symmetric combinations of a qubit and TLS wavefunctions. These effects are readily observed with atomic ensembles, and are associated with a constructive or destructive interference of electric fields emitted by atomic dipoles which accelerate or slow down the decay of quantum states. The latter interference effects are also widely explored in antenna design to suppress or enhance emission lobes. The goal of our research is (i) to create states $|\pm\rangle = 1/\sqrt{2}(|1,g\rangle \pm |0,e\rangle)$ (where $1, 0$ are qubit states, g, e are states of TLS) and (ii) to study its temporal dynamics, e.g. decay and coherence times. We hope to shed light on the nature of fluctuators and its coupling to qubits.

For our experiment we choose one of the TLS

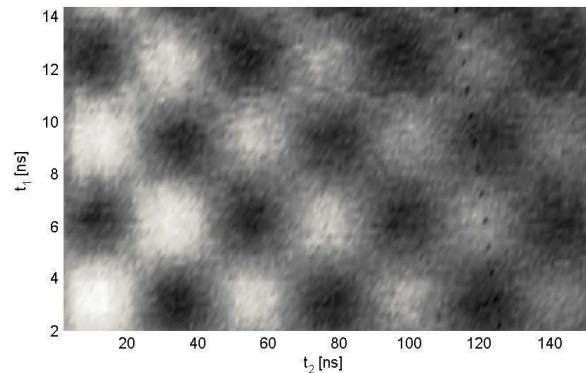


Figure 2: The qubit state probability versus rotation and decay times t_1 and t_2 .

which has resonance frequency $f_f = 7.735$ GHz, coupling strength $g/2\pi = 23$ MHz, decay time $T_1 \approx 400$ ns, and coherence time $T_2 \approx 400$ ns. The qubit is initially detuned below TLS by $\Delta = 160$ MHz, see Fig.1(a). Strong π pulse on the qubit pumps the whole coupled system into the state $|1, g\rangle$ with probability of 0.8, after that qubit is brought in resonance with TLS for 11 ns and Bloch vector is rotated around x -axis and reaches the state $1/\sqrt{2}(|1,g\rangle + |0,e\rangle)$, as shown in Fig.1(b). To get $|\pm\rangle$ states, Bloch vector is moved along the equatorial plane for the time t_1 when qubit is detuned by 160 MHz.

To measure the decay of the resulting state, the qubit is brought again into resonance with TLS and readout after time t_2 . The resulting measurement versus rotation time t_1 and decay time t_2 is shown on Fig.2. The graph displays a checkerboard pattern. For certain values of t_1 , probability of state $|1\rangle$ shows no oscillations with t_2 , and therefore it corresponds to eigenstates of the interaction Hamiltonian, i.e. states $|\pm\rangle$. The states $|\pm\rangle$ decay with the same characteristic time of 110 ns, contrary to atomic systems where enhancement or suppression of the rate would be observed. It can be explained by photon emissions into different baths, as it has been recently predicted by the group of Alexander Shnirman (TKM).

[1] C. J. Myatt *et al.*, Nature **403**, 269 (2000)

[2] M. Neeley *et al.*, Science **325**, 722 (2009)

[3] F. Varsanyi and G. H. Dicke, Phys. Rev. Lett. **7**, 442 (1961).

Noise measurements of cryogenic amplifiers for qubit experiments

C. Schwemmer, T. Wirth, A. Lukashenko, M. Mück¹, and A. V. Ustinov

Ultra-low noise cryogenic amplifiers are a prerequisite for a variety of readout schemes for superconducting qubits based on Josephson junctions. The evaluation of the noise temperature of cryogenic amplifiers is an essential task for achieving high sensitivity and lowest back action. We developed a cryogenic noise source based on a 50 Ohm load located in vacuum at temperature variable between 10 K and 45 K. By measuring the output power of a cryogenic low noise HEMT-amplifier at different temperatures of the load using a standard spectrum analyzer we determine the gain and the noise temperature of the amplifier. The advantage of our method compared to the conventional noise diode switching technique is that in our approach the noise source is heated up continuously providing many data points and thus offering better accuracy. We also use this technique to measure the noise temperature and amplification of microstrip SQUID amplifiers operated at 4.2 K.

The noise temperature of an amplifier can be determined by means of a noise source. Our setup is shown in Fig. 1. The noise source is mounted on a dipstick immersed in liquid helium. The idea behind this approach is that a 50 Ω load at temperature T produces a total noise power of

$$P_{\text{noise}} = k_B T B$$

in a frequency band B . Thus the load produces noise power determined by its physical temperature. As shown in Fig. 1, the noise source consists of a 50 Ω load with a small copper coil with manganin wire around it. A maximum heating power of 100 mW can be achieved with this coil heating up the load. On top of the 50 Ω load there is a small copper block with a carbon glass thermometer to measure the temperature of the load. The load is mounted on a short piece (10 cm) of a microwave cable. It is crucial that this microwave cable is made of stainless steel, since this type of material has a much lower thermal conductivity than a copper cable. This ensures that, on the one hand, the helium bath in which the noise source is immersed does not cool down the load and that, on the other hand, the load does not heat up the device under test. The 50 Ω load and the stainless steel microwave cable are mounted inside a brass cylinder that is evacuated with a vacuum pump. At the bottom of the brass cylinder, there is a flange to open the cylinder so that the heater and the thermometer can be inspected. The flange is made helium-tight with an indium seal.

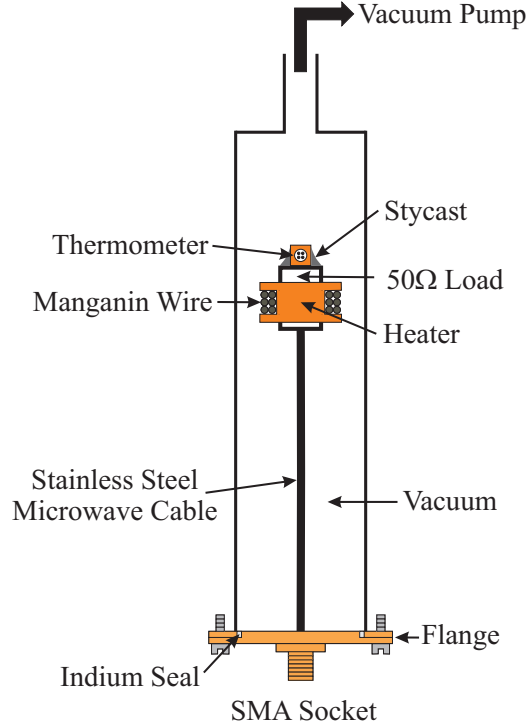


Figure 1: Schematics of the noise source used for determining the noise temperature of our cryogenic amplifiers.

The noise measurement setup is shown in Fig. 2. The noise source is connected to the device under test with a copper microwave cable and two 1 dB attenuators. These serve for improving matching of the input impedance of the device under test (which is not always 50 Ω) and for thermal anchoring of the inner conductor of the microwave cable. Other components mentioned above are immersed in liquid helium and thus have a temperature of 4.2 K. The brass cylinder is evacuated to hold vacuum since otherwise the load could not be heated up.

The second stage amplifier indicated in Fig. 2 is optional. Only if the noise power at the output of the device under test is too small to be detected by the spectrum analyzer, a second stage amplifier is needed. The second amplifier could also be immersed in liquid helium or it can be operated at room temperature.

Since microstrip SQUID amplifiers operated in liquid helium have a noise temperature of the order of the bath temperature [1], it should be possible to

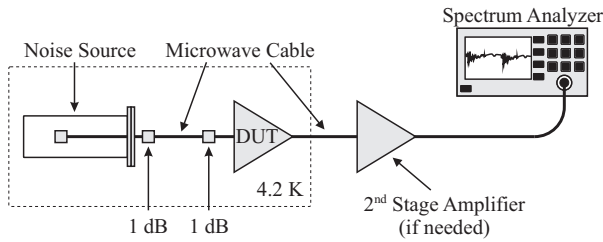


Figure 2: Setup used for noise temperature measurements.

measure their noise temperature with our method. The setup shown in Fig. 2 was used for this kind of measurements. A microstrip SQUID amplifier should not be directly connected to the spectrum analyzer for two reasons. On the one hand, the amplifier could easily be saturated by thermal noise fed by the coaxial cables from the components of the setup at room temperature. On the other hand, the signal level at the output of the microstrip SQUID amplifier is too low to be detected by the spectrum analyzer. Therefore a second stage cold amplifier was used in this case, and the total noise power in a band of 50 MHz width was measured with a spectrum analyzer.

In order to find the best settings of the SQUID bias and the flux bias, a map of its control currents was recorded. Both the SQUID and the flux bias were swept by means of two current sources that were controlled by the analog outputs of a D/A card in the measurement computer. Fig. 3 shows the input power of the spectrum analyzer versus the SQUID bias and the flux bias for a constant temperature of the load of 30 K. The SQUID bias current was increased from $1 \mu A$ to $8 \mu A$ in steps of $0.1 \mu A$ and the flux bias current was swept from $-40 \mu A$ to $130 \mu A$ in steps of $1 \mu A$. One can see the best bias points for maximum amplification of the SQUID amplifier are at a SQUID bias of $5 \mu A$ and the flux bias of $10 \mu A$ and $105 \mu A$ respectively. This also exhibits that the gain is a periodic function of the flux, as it is ex-

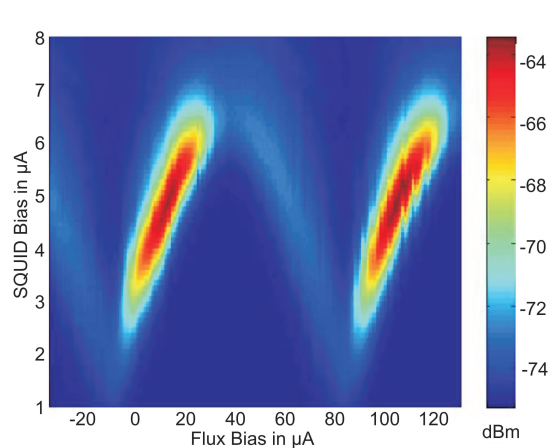


Figure 3: Bias current map recorded with the setup shown in Fig. 2. The temperature of the 50Ω load was kept at 30 K. The settings of the spectrum analyzer were: center frequency 2.025 GHz, resolution bandwidth 300 kHz, video bandwidth 1 MHz, sweep time 100 ms, span 100 MHz, channel bandwidth is 50 MHz.

pected. However, in this first experiment we did not detect an increase in the total noise power when the load was heated up. A possible reason for this might be an impedance mismatch on the input of the SQUID amplifier.

We have additionally directly verified the noise temperature of our HEMT amplifiers. This approach is promising and our measurements lay out the way for further experiments. We successfully characterized cryogenic broad band HEMT amplifiers, made at IMS (KIT) with our setup.

[1] M. Mück, C. Welzel and J. Clarke, *Appl. Phys. Lett.*, **82**, 3266, (2003).

¹ Institut für Angewandte Physik, Justus-Liebig Universität Giessen, 35392 Giessen, Germany

Depinning of fluxons in Josephson arrays with magnetic inhomogeneities

Kirill G. Fedorov and Alexey V. Ustinov

Josephson phenomena are of great interest because of their unique properties. One is the exhibition of topological solitons associated with vortices in long Josephson junctions. A soliton is a magnetic flux equal to the magnetic flux quantum $\Phi_0 = h/(2e) = 2.07 \cdot 10^{-15}$ Wb, that is why they are also called *fluxons* [1]. Fluxons (see Fig.1) can travel along a junction with a maximum velocity only 20 – 30 times smaller than speed of light in vacuum. Fluxons can serve for many applications such as Josephson transmission lines, frequency clock-generators [2], qubit readout techniques [3].

One of the main challenges for the practical use of fluxons in discrete Josephson arrays is their pinning on random fluxes, situated inside a system. The random flux can be induced, e.g., by Abrikosov vortices randomly trapped in superconducting electrodes of the array (see Fig.2). The illustration of a such situation is depicted on current-voltage characteristic of a Josephson junction with one fluxon on Fig.3. Pinned fluxon sits in a metastable state until bias current η reaches certain value at which potential barrier U_0 vanishes and fluxon escapes, switching Josephson junction from superconducting to finite voltage state. Due to a thermal fluctuations, switching histogram broadens. Another fundamental pinning force appears from so-called Pierles-Nabarro potential, which is the consequence of the discrete nature of such a chain (for the details see [4]).

The goal of this work is to investigate values of depinning current dependent on system's parameters. We would like to find the scaling of the depinning currents with the discreteness. Our interest in this problem from a different point of view related to propagation of Cooper pair charge solitons in junction arrays [5].

For describing dynamics of the system we employ perturbed sine-Gordon equation:

$$\frac{\partial^2 \phi_i}{\partial t^2} + \alpha \frac{\partial \phi_i}{\partial t} - \frac{\phi_{i+1} - 2\phi_i + \phi_{i-1}}{a^2} = \eta - \sin(\phi_i) + I_i - I_{i-1}, \quad (1)$$

here ϕ_i is phase difference of the i -th junction (for the charge solitons case it is the charge variable of the i -th island), η is the bias current normalized to the critical current, α is the damping, a is the discreteness parameter normalized to the mean Josephson length, I_i is the current, created by random flux, pinned in between i -th and $(i-1)$ -th junction.

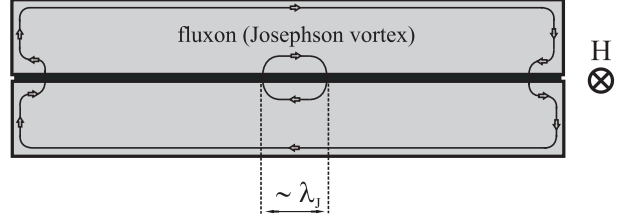


Figure 1: Schematic cross section of a conventional distributed Josephson junction with a fluxon (Josephson vortex) located deep inside it. Lines show the flow of screening supercurrents.

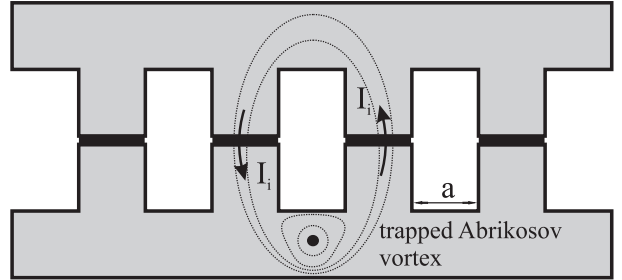


Figure 2: Schematic cross section of a discrete Josephson array with a trapped Abrikosov vortex creating parasitic random current I_i .

We simulate depinning of a single fluxon in the discrete Josephson array with the following constraints. We fix the amplitude of random fluxes, trapped between two neighboring junctions, measured in the units of flux quantum Φ_0 . We take fluxes as uniformly distributed within given amplitude. Due to the normalization, constraint on random currents transforms into $-\gamma\pi/a^2 < I_i < \gamma\pi/a^2$, there $\gamma = 1$ corresponds to maximum possible flux of Φ_0 .

We calculate depinning current using numerical simulations of the sine-Gordon equation (1), in the underdamped regime with $\alpha = 0.05$ and with random currents which induced by trapped fluxes. Numerical solution of (1) with open boundary conditions has been computed on the basis of implicit finite-difference scheme. Typical values of time discretization step are $\Delta t = 0.05 - 0.01$, number of averaging realizations are $N = 2000 - 10000$. The simulations run as follows. First, we solve solution of sine-Gordon equation with a single fluxon placed

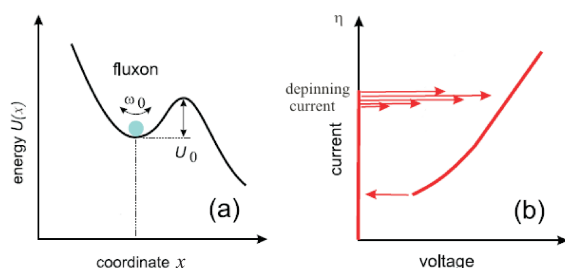


Figure 3: (a) Fluxon pinned in a potential well induced by a pinned Abrikosov vortex. (b) Depinning event of the fluxon at the certain bias current. Amplitude of arrows corresponds to probability of switching.

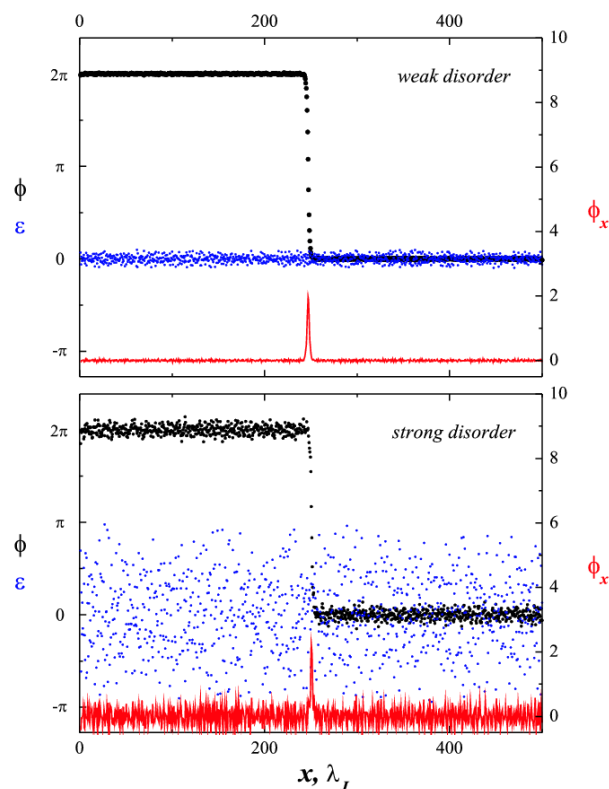


Figure 4: Fluxon in the Josephson junction array with parameters: $a = 0.5$ and for different random current intensities; resulting random current $\varepsilon_i = I_i - I_{i-1}$.

in the middle of long Josephson junction, then we increase the bias current and at some point fluxon starts to move and reaches the boundary of system. At this moment we register that fluxon is completely depinned. To check this outcome, the ramping rate of the bias current is decreased and the length of the

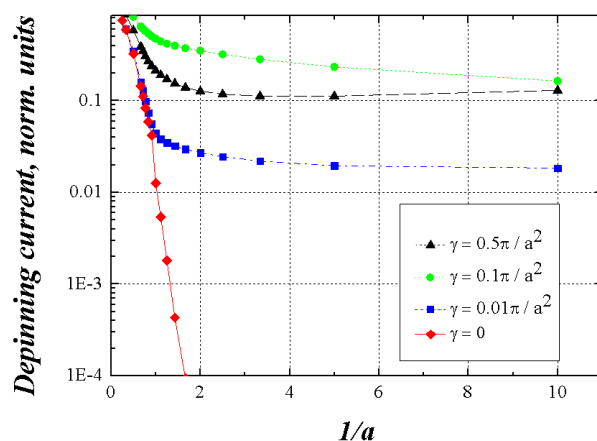


Figure 5: Dependence of depinning current on the discreteness parameter a .

array increased. Once the obtained depinning current converges, we take this as the final result.

In Fig.4 one can see the snapshots of the initial phase distribution with fluxon inside of the array for small and large random flux intensities γ ; One can notice that even relatively large random fluxes does not significantly change the form of the fluxon.

Figure 5 shows the results of calculation of the depinning current. Solid line with $\gamma = 0$ shows pinning force due to Pierless-Nabarro potential. Curves with higher γ correspond to the non-zero random fluxes ranging from small amplitude disorder $\gamma = 0.01\pi$ to large disorder at $\gamma = 0.5\pi$. It is interesting, that for curves with moderate γ , the behavior of depinning current becomes non-monotonic. Above a certain value of discreteness (about $a = 0.3$), depinning current increases with decreasing a . This could be explained by the fact, that we are keeping the maximum random flux between junctions constant, but not the standard deviation of the phase itself, which leads to an increase of the potential barrier for the pinned fluxon. The question, why we do not see the same effect for the maximum amplitude of random flux remains and should be investigated further.

[1] T. A. Fulton and R. C. Dynes, Solid St. Commun. **12**, 57 (1972).

[2] E. Kirichenko and V. Vernik, IEEE Trans. Appl. Supercond., **15**, 296 (2005).

[3] D.V. Averin, K. Rabenstein, and V.K. Semenov, Phys. Rev. B **73**, 094504 (2006).

[4] O.M. Braun and Y.S. Kivshar, The Frenkel-Kontorova Model, Springer (2004).

[5] Z.Hermon, E. Ben-Jacob and G.Schön, Czechoslovak Journal Of Physics, **46**, 587 (1996).

Microwave fluxon readout for superconducting qubits

Kirill G. Fedorov and Alexey V. Ustinov

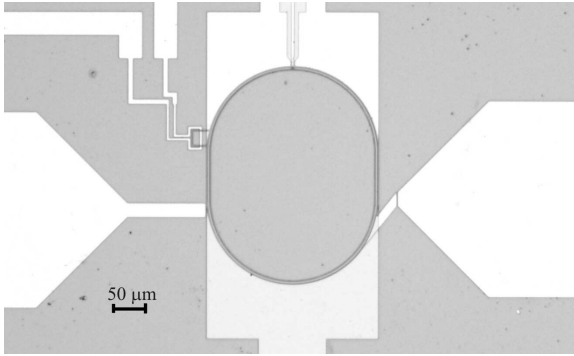


Figure 1: Photo of the sample with the annular Josephson junction (looking like a stadium here) and microwave antennas on the sides. Current injectors, for creating fluxons, are attached to the top to the ring. Control line left to the annular junction is inductively coupled to it.

We are experimentally investigating a new type of detector for very fast and weakly perturbing readout of superconducting qubits. The detection principle is based on measuring the delay time of a ballistic fluxon moving in a Josephson transmission line induced by a qubit [1,2]. Due to a small magnetic perturbation the fluxon propagation delay depends on the state of the qubit.

Advantages of this method are small dissipated power, high time resolution and small perturbation of the investigated system. We would like to measure time delay as a phase shift of fluxon oscillations phase-locked by an external clock. As the first step towards the experimental realization of fluxon detector, here we report measurement of fluxon radiation from annular Josephson junctions using a cryogenic amplifier.

Our detector is an annular Josephson junction with microwave antennas (see Fig.1). The most significant advantage of closed topology of annular junction is the conservation of trapped flux, which allows, by putting special current injectors in the biasing electrode, to create the required number of fluxons [3]. The test circuit was fabricated using photolithography and standard Nb/AlO_x/Nb trilayer process.

Detection of fluxon radiation was performed at the 4.2 K temperature with the use of a cryogenic microwave amplifier placed at the same temperature in the vicinity to the sample. Radiation spec-

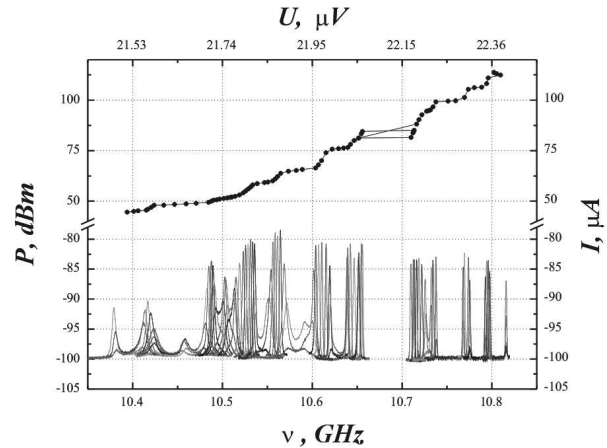


Figure 2: Measured radiation spectrum of Josephson vortex in annular junction and recalculated the current-voltage characteristic of a single fluxon step.

trum was measured using Rohde&Schwarz FSUP26 spectrum analyzer. An example of measured spectrum of fluxon oscillations in the annular junction is shown in the Fig.2. Second Josephson relation allows us to recalculate the frequency spectrum into current-voltage characteristics, with a precision that, roughly, is by factor 100 higher than a precision of direct voltage measurements. Such the approach allows us easily identify the fine structure of the fluxon step. Detailed investigation of single fluxon spectra reveals many interesting details, as regions of negative differential resistance, hysteretic behavior, points of bifurcations. All these features are expected due to the imperfections of the sample, details of its geometry, all enhanced due to the small damping in this system.

On the way towards practical realization of a fluxon qubit readout, we observe that the fluxon delay by an external magnetic perturbation of 0.1 nT induces measurable frequency shift of 1.9 MHz fluxon oscillations. This result permits using of the frequency-locked fluxon oscillator as a non-destructive tool for repetitive measurements of the qubit state.

[1] D.V. Averin, K. Rabenstein, and V.K. Semenov, Phys. Rev. B **73**, 094504 (2006).

[2] A. Fedorov, A. Shnirman, G. Schön, and A. Kidiyarova-Shevchenko, Phys. Rev. B **75**, 224504 (2007).

[3] A.V. Ustinov, Appl. Phys. Lett. **80**, 3153 (2002).

Search for charge solitons in small-capacitance Josephson junction arrays

H. Rotzinger, R. Schäfer, W. Cui, J. Zimmer and A.V. Ustinov

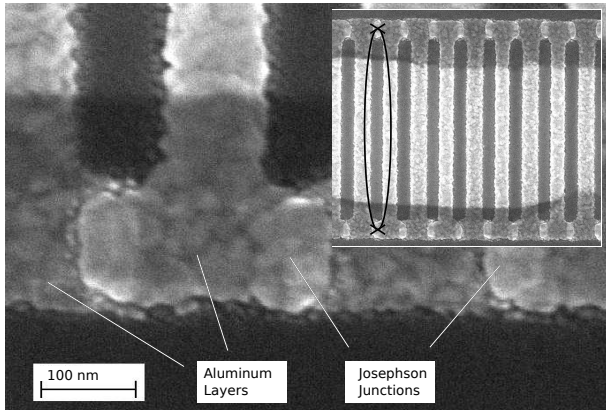


Figure 1: SEM micrograph of an array of small capacitance SQUIDs made by aluminum shadow evaporation (inset). The junction area of about 30×100 nm leads to an island capacitance in the range of 1 fF.

Coupled superconductors have been revealing a rich variety of physical effects since the discovery of the Josephson effect in the 60's of the last century. More recently, the investigation of small, isolated islands became possible and led to fascinating effects including devices like the Cooper pair transistor. In this emerging experimental project we aim towards a better understanding of uniform arrays of small capacitance Josephson junctions (SCJJ). In particular, we are interested in the charge transport properties of these devices, since theory predicts the occurrence of constant current steps at current values $I_n = n 2ef$ in the current-voltage characteristics (IVC) [1]. Here n is an integer number and f is the frequency.

In Figure 1 a micrograph of such an array of coupled SCJJ is shown. The sample was fabricated utilizing conventional electron beam lithography and aluminum shadow evaporation. The SQUID Josephson junction arrangement, shown in the inset, does allow to externally tune the Josephson coupling energy $E_j = \hbar I_c(B)/2e$ by changing an applied magnetic field B .

SCJJ arrays are characterized by a zero current state (Coulomb blockade, CB) for bias voltages below a threshold voltage V_t . Our first measurements of the IVC for different applied magnetic fields at a temperature of 20 mK are shown in Fig. 2.

In a basic picture V_t can be understood considering the Coulomb energy $E_c = e^2/2C$ necessary to place an excess Cooper pair charge $2e$ on one island.

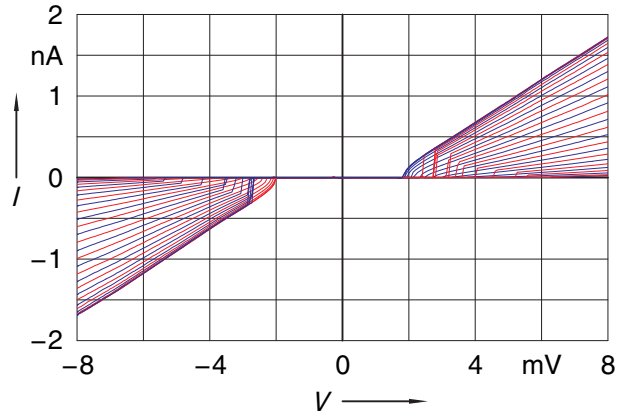


Figure 2: Current-to-voltage characteristics of the small capacitance Josephson Junction array depicted in Figure 1.

Here the capacitance $C \sim 1$ fF is mainly given by the capacitance of the two SQUID Josephson junctions. An array of islands does further enhance this blocking effect since an applied bias voltage is distributed over the whole array. For voltages larger than V_t the device displays a resistive branch and a not yet fully understood hysteresis in the return path.

Due to the Josephson coupling, E_c should be compared with E_j . Depending on the ratio E_c/E_j and the charge screening length $\Lambda \sim \sqrt{C/C_0}$, C_0 is the capacitance to the environment, one excess Cooper pair charge is spread over several (Λ) islands. An external bias voltage induces charge motion [2][3]. Taking the small capacitances and non-linear inductance of the Josephson junction into account, the system allows to be described by a sine-Gordon type equation which exhibit solitary wave solutions corresponding to $2e$ charge solitons. These solutions have been studied in detail in a dual system, long Josephson junctions, there magnetic flux vortices play the role of solitons (for a review see e.g. [4]).

Further experimental work includes the fabrication of samples with tailored properties as well as their study under microwave irradiation.

[1] W. Guichard, F. W. J. Hekking, (2009), to be published

[2] S.Rachel, A. Shnirman, (2009), to be published

[3] D.B.Haviland, P. Delsing, Phys. Rev. B, **54**, 10 (1996)

[4] A.V. Ustinov, Physica D, **123**, 315 (1998)

Searching for “Münchhausen Effect” in an asymmetric dc-SQUID

S. Butz, K. G. Fedorov, A. K. Feofanov, R. Dolata¹, B. Mackrodt¹ and A. V. Ustinov

It has been suggested by Thomann *et al.* [1] that the coupling of one classical and one quantum mechanical degree of freedom can be realized in an asymmetric dc-SQUID. Since such a coupled system can escape from a metastable state on seemingly its own account, its behaviour was called “Mnchhausen effect”, after baron Mnchhausen who claimed to have himself rescued out of a swamp by pulling at his own hair.

The equation of motion for a single Josephson junction within the RCSJ model [2] is analogous to the equation of motion of a pendulum under external torque: The bias current through the junction corresponds to a constant external torque and its intrinsic capacitance can be considered as mass equivalent. Thus, if the capacitance is small enough, the particle, i.e. in our case the phase difference across the junction, exhibits quantum mechanical behaviour such as the ability to tunnel through a potential barrier. The idea for the experimental realization of the “Mnchhausen effect” is to take a dc-SQUID with two small identical junctions. In order to make one of them behave classically, its “mass” is artificially increased by shunting it with a large capacitor close to the junction.

Within the RCSJ model the dynamical behaviour of a dc-SQUID is given by the equations of motion

$$\omega_{pi}^{-2} \ddot{\varphi}_i + \eta_i \dot{\varphi}_i = -\partial_{\varphi_i} v(\varphi_1, \varphi_2), \quad i = 1, 2 \quad (1)$$

where φ_1 is the phase difference across the classical and φ_2 the phase difference across the quantum junction. $\omega_{pi} = \sqrt{2eI_{ci}/\hbar C_i}$ is the plasma frequency and $\eta_i = \hbar/2eR_i I_{ci}$ the damping coefficient. In our case $I_{c,1} = I_{c,2}$ and $R_1 = R_2$ but $C_1 \gg C_2$.

The potential $v(\varphi_1, \varphi_2)$ is given as

$$v(\varphi_1, \varphi_2) = (1 - \cos \varphi_1) + (1 - \cos \varphi_2) - j(\varphi_1 + \varphi_2) + \frac{k}{2}(\varphi_1 - \varphi_2)^2. \quad (2)$$

$j = I_b/(2I_c)$ is the normalized bias current through the SQUID and $k = 1/\beta_L = \hbar/(2eLI_c)$ (with L being the inductance of the SQUID loop) gives the inductive coupling between the two junctions. We can picture the dynamics of the dc-SQUID as a particle that moves in a two dimensional potential (cf. Fig. 1) and that behaves quantum mechanically in φ_2 - and classically in φ_1 -direction. For strong damping we can neglect the kinetic part in the equations of motion and understand the system by analyzing the potential solely.

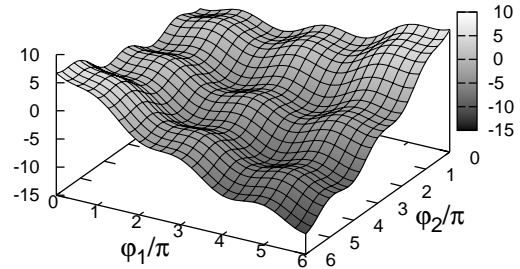


Figure 1: The energy potential $v(\varphi_1, \varphi_2)$ plotted for $j = 0.3$ and $k = 0.07$.

At $j = 0$ the particle resides in its global minimum at $\varphi_1 = \varphi_2 = 0$. For $j > 0$ the potential is tilted as can be seen in Fig. 1 and $\varphi_1 = \varphi_2 = 0$ is not the global minimum anymore. There are two possible escape directions, namely along φ_1 and along φ_2 . The question is now, when, how and along which direction the particle leaves this metastable state.

At zero temperature the particle cannot leave the metastable state in φ_1 -direction as long as there is a barrier between its own and the adjacent minimum. In φ_2 -direction, however, the particle can tunnel through the barrier as soon as the adjacent minimum is lower than the current one. After the tunneling process the system is at $(\varphi_1, \varphi_2) \approx (0, 2\pi)$. If the coupling k between the two junctions is strong enough, there is no barrier blocking the escape in φ_1 -direction. By repeating this process the particle starts running down the potential. As the particle coordinate in reality corresponds to phase differences across Josephson junctions, a voltage drop occurs across the SQUID.

If k is not big enough, a further increase of the bias current is necessary to tilt the potential until the barrier between $\varphi_1 \approx 0$ and $\varphi_1 \approx 2\pi$ ($\varphi_2 \approx 2\pi$) vanishes. Beyond this point the system enters the running state.

Thus, we have two escape mechanisms. Either the particle can escape right after the tunneling process in φ_2 -direction or after the tunneling a further increase in current is necessary to enable the escape. Which of the two escape mechanisms described above takes place, and at which current $j_c(k)$ the system switches to the voltage state, depends on the cou-

pling strength k . In Ref. [1] predictions for this dependence for strong as well as for weak damping were made and it is the aim of our experimental work to test these predictions.

We designed four different underdamped SQUIDs S1, S2, S3 and S4 with parameters given in Tab. 2.

	S1	S2	S3	S4
I_c (μA)	0.56	0.56	3.5	3.5
L (nH)	4	8	0.25	0.7
k	0.14	0.074	0.37	0.13

Table 2: Design parameters for the dc-SQUIDs. I_c is the critical current of one junction, L the inductance of the SQUID loop.

The SQUIDs were fabricated with a standard Nb/ AlO_x /Nb trilayer process [3] and cooled down to temperatures $T \approx 310$ mK using a 3He cryostat.

To determine the switching properties of the different SQUIDs current ramp histograms were taken. The bias current is ramped with a constant rate. It starts from a current value approximately $I_{start} < 0$, until the voltage across the SQUID switches to some finite voltage above the set threshold voltage. The time between the crossing of $I_b = 0$ and the switching to the voltage state is measured, and, by multiplying it with the ramping rate, the switching current is determined. This method is repeated 10^4 times to gather data for a histogram.

In Fig. 2 measurement results for S2, S3 and S4 and shown.

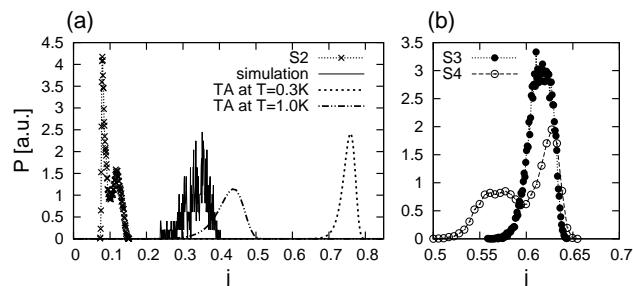


Figure 2: (a) Measurement results for S2 (crosses) compared with the thermal escape of the single junction at $T = 300$ mK (dashed) and at $T = 1$ K (dashed/dotted). Solid lines show the histogram resulting from our simulation based on the equations (1) including thermal noise at $T = 1$ K. (b) Measurement results for S3 (solid circles) and S4 (open circles). Note different current intervals for (a) and (b).

The double peak structure of the measured histograms of the S2 and S4 indicates that we are looking at two different competing escape mechanisms.

One can also see that different coupling parameters k lead to different histogram shapes, i.e. a single peak for S3 and nearly mirrored double peak structures for S2 and S4.

We need to consider the influence of temperature which was not done in theory. If the temperature is high enough, the phase particle is able to overcome the barrier in φ_1 -direction via thermal activation (TA). In Fig. 2(a) we compare the histogram of S2 with histograms for single junctions calculated numerically by using the thermal escape rate [4].

In order to understand the behaviour of the system in more detail and to compare it with theoretical predictions for parameters that exactly match our design and measurement conditions, we performed numerical simulations. By integrating numerically the coupled differential equations (1) including a thermal noise term, a switching current histogram is produced. It is shown in Fig. 2(a) for $T = 1$ K (solid line) with the parameter values of sample S2. The simulation of the dc-SQUID shows a lower switching current than the calculation for the single junction. This is because for $k < 1$ the coupling between the two junctions decreases the barrier height compared to that of the single junction.

Since the numerical results at $T = 1$ K show the switching at higher currents than our measurements taken at $T \approx 300$ mK, we believe that, due to electromagnetic interference, the effective temperature of the junctions is considerably higher than the temperature of the cryostat. We plan to improve the setup by adding extra filtering. The escape via thermal activation can be reduced by measuring the samples at lower temperatures in a dilution cryostat. Further measurements should be made to explain the values of the switching currents and the origin of the double peak structure of the histograms of S2 and S4.

The reported first measurement data look intriguing. So, if Mnchhausen really can pull himself out of the swamp, remains to be seen.

[1] A.U. Thomann, V.B. Geshkenbein, G. Blatter, Phys. Rev. B **79**, 184515 (2009).

[2] M. Tinkham, "Introduction to Superconductivity", Dover Publ., (1996).

[3] R. Dolata *et al.*, J. Appl. Phys. **97**, 054501 (2005).

[4] J. Martinis *et al.*, Phys. Rev. B **35**, (1987).

¹ Physikalisch-Technische Bundesanstalt, 38116 Braunschweig, Germany

A tunable rf SQUID manipulated as flux and phase qubit

S. Poletto, J. Lisenfeld, A. Lukashenko, B. Döring and A.V. Ustinov

We report experiments with a tunable rf SQUID and demonstrate two different manipulation procedures. The system under test, a double SQUID, can be operated in two different regimes: (i) as a flux qubit manipulated via fast dc-pulses of magnetic flux, and (ii) as a phase qubit in which the quantum state evolution is controlled by microwave pulses of chosen amplitude and phase. The former manipulation approach without using microwaves allows to reach very high oscillation frequencies [1], while operating the same circuit as a phase qubit offers the possibility to verify the obtained results using a well defined and studied manipulation technique [2]. We saw that the coherence times measured using the two different manipulation schemes are rather similar, suggesting that decoherence acts in a similar way in both cases. This conclusion draws attention to common sources of decoherence (presumably, dielectric loss due to two-level fluctuators in the material used for chip fabrication), and emphasizes the relevance of increasing the number of qubit gates within the coherence time by increasing the oscillation frequency of the system.

The circuit we studied is shown in Fig. 1. It consists of a superconducting Nb loop of inductance $L = 85\text{pH}$ interrupted by a small dc SQUID of inductance $l = 6\text{pH}$. This double SQUID is manipulated via two magnetic bias fluxes Φ_x and Φ_c applied to the large and small loops, respectively. The system is inductively coupled to an unshunted dc SQUID used for the readout of state information. The circuit was fabricated by Hypres using standard Nb/ AlO_x /Nb technology and SiO_2 as dielectric material for junction isolation.

The flux qubit manipulation scheme shown in Fig. 2 is based on changing the double well potential to a single well shape and back, caused by fast dc pulses on the bias flux Φ_c . The computational states are the flux states of the double well potential (i.e. left and right wells), while the coherent evolution occurs between the two lowest energy eigenstates of the single well potential. The first step of the manipulation procedure is the initialization of the system in a defined flux state. (1) Starting from a double well with high barrier, the potential is tilted by changing Φ_x until it has only a single minimum (left or right, depending on the polarity and amplitude of the applied flux pulse). This potential shape is maintained long enough to ensure relaxation to the ground state. (2) Afterwards, the potential is tuned back to the initial double-well state. The high barrier prevents

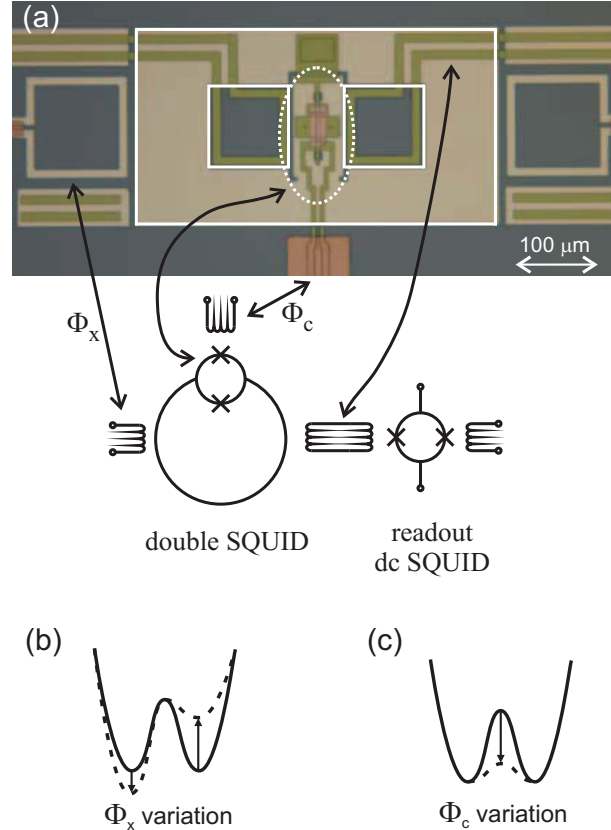


Figure 1: (a) Photo and schematic representation of the studied double SQUID. The entire device occupies a space of $430 \times 230\mu\text{m}^2$. (b)-(c) Manipulation of the energy potential profile via the two bias fluxes Φ_x and Φ_c . Variation of the symmetry is achieved by changes of the flux Φ_x , while the barrier between the local minima is tuned by the flux Φ_c .

any tunneling and the qubit is thus initialized in the chosen potential well. (3) Next, the barrier height is lowered to an intermediate level that preserves the initial state but allows just a small-amplitude Φ_c flux pulse to be used for the subsequent manipulation. (4) The following Φ_c -pulse transforms the potential into a single well for a duration Δt in the nanosecond range. In this situation, the relative phase of the ground and the first excited states evolves depending on the energy difference between them. (5) After the end of the Φ_c -pulse, the double well is restored and the system is measured in the flux base $\{|L\rangle, |R\rangle\}$. The readout of the qubit flux state is accomplished by starting a bias current ramp to the dc SQUID and

recording its switching current to the voltage state.



Figure 2: Variation of the potential shape during the manipulation.

The pulse sequence is repeated for $10^2 - 10^4$ times in order to evaluate the probability $P_L = |\langle L | \Psi_{final} \rangle|^2$ of the left state occupation at the end of the manipulation. In Fig. 3, we show coherent oscillations between the states $|L\rangle$ and $|R\rangle$ which were obtained by changing the duration Δt of the manipulation pulse Φ_c . Increasing the amplitude of the Φ_c -pulse results in a deeper single well, which leads to a larger level spacing which in turn results in a higher oscillation frequency.

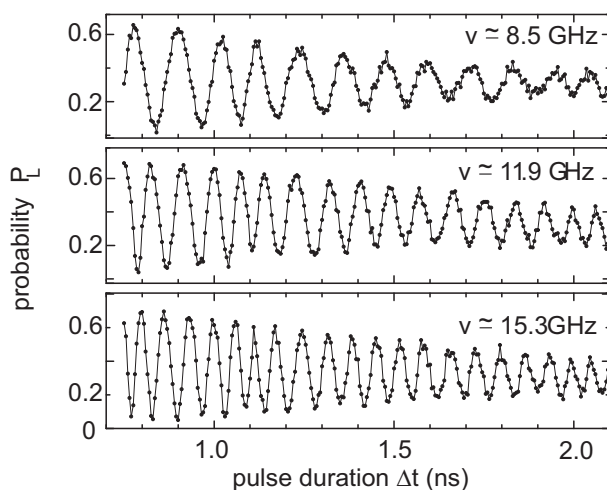


Figure 3: Dependence of the probability of measuring the state $|L\rangle$ on the pulse duration Δt for the qubit initially prepared in the $|L\rangle$ state, for different pulse amplitudes $\Delta\Phi_c$, resulting in the indicated oscillation frequency.

In addition to the above microwave-free manipulation, we have also operated the system as a phase qubit using microwave driving, which is possible due to its tunability. The operating procedure is the same as that reported in Ref. [3]. Here the two logical qubit states are located in the shallow potential well of a strongly asymmetric double well potential. State transitions were induced by interaction with an applied resonant microwave field, allowing us to detect driven Rabi oscillations, shown in Fig. 4, by changing the duration of the microwave pulse. The

energy relaxation time T_1 was measured directly by observing the exponential decay of the excited state population probability after applying a microwave π -pulse.

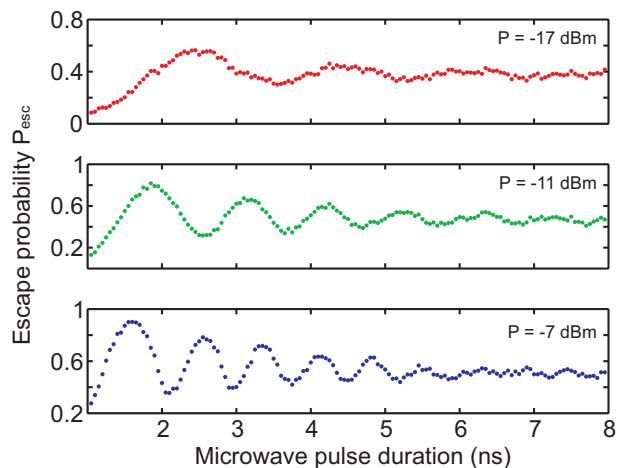


Figure 4: Rabi oscillations of the double SQUID manipulated as a phase qubit by applying microwave pulses at 19 GHz. The oscillation frequency changes from 540 MHz to 1.2 GHz by increasing the power of the microwave signal by 10dB

The measured coherence time of the Larmor oscillations obtained in the flux regime is about 1 ns, of the same order as the relaxation time T_1 in the phase regime. Since best available phase qubits already display relaxation times of several 100 ns, obtained by using appropriate materials in the fabrication processes [4], we suppose that also the coherence time of the Larmor oscillations obtained without microwaves could strongly benefit from the same treatment. Such a possible improvement of the coherence by two orders of magnitude, together with the much higher oscillation frequency in the microwave-free Larmor mode, should in principle allow to reach the ultimate goal of 10^4 single-qubit operations within the coherence time which is needed for the implementation of quantum algorithms [5].

Further experiments with new samples made from Al and with SiN as dielectric layer are in progress.

Acknowledgements: This work was a collaboration with F. Chiarello, M.G. Castellano, C. Cosmelli, G.Torrioli and P. Carelli at IFN CNR in Rome.

- [1] S. Poletto *et al.*, *New J. Phys.* **11** (2009) 013009
- [2] S. Poletto *et al.*, *Phys. Scr.* **137** (2009) 014011
- [3] J. Lisenfeld *et al.*, *Phys. Rev. Lett.* **99** (2007) 170504
- [4] J.M. Martinis *et al.*, *Phys. Rev. Lett.* **95** (2005) 210503
- [5] E. Knill *Nature* **434** (2005) 39

Investigation of dielectric losses in amorphous thin-films used in Josephson junction fabrication

S.T. Skacel, Ch. Kaiser¹, H. Rotzinger, J.M. Meckbach¹, S. Wnsch^{1,2}, S. Poletto, A. Bruno³, M. Siegel¹, and A.V. Ustinov

Many applications of Josephson junctions like Josephson voltage standards, radiation sources, digital-to-analogue converters or RSFQ circuits with passive transmission lines involve microwave signals, so that keeping microwave losses in these structures small is strongly desirable. For superconducting qubits, reducing dielectric losses is extremely important. As Martinis *et al.* have pointed out recently, the microscopic origin of the dielectric losses are spurious dipoles-like two-level-systems (TLSs), which couple to the qubit and hence reduce its coherence time [1, 2]. These TLSs were found in dielectric thin films and contribute to the dependence of the losses on temperature and power [1, 2]. Another recent work of Gao *et al.* reported TLSs on metal surfaces [3] as well. Furthermore, the sample processing was reported to influence the dielectric losses [4].

We have recently developed a reliable method for the direct measurement of dielectric losses in amorphous thin films using a special design of lumped element superconducting resonators (see Fig. 1) [5].

The goal of the present work is to characterize the

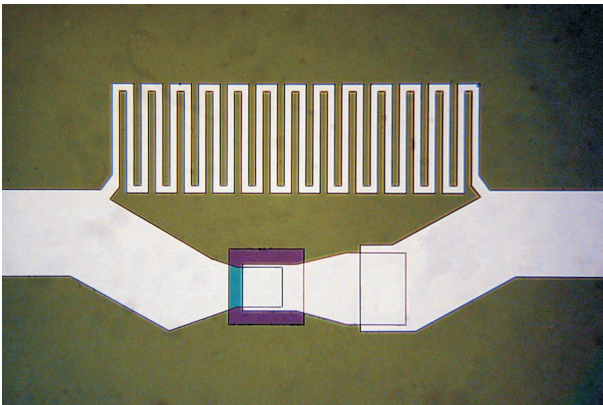


Figure 1: Our design of a lumped LC resonator used for loss measurements.

losses of different dielectric thin films and to investigate the frequency dependence of the losses in order to reveal the underlying loss mechanisms. Furthermore, we want to carry measurements down to temperatures and energies in the qubit operation regime (mK temperatures, single photon energy) and relate the results to coherence time measurements in super-

conducting qubits.

Dielectric losses are measured as the loss tangent $\tan \delta = R/X$, which is the ratio of the real to the imaginary part of the complex impedance $Z = R + iX$. By measuring the intrinsic quality factor Q_0 of a resonator at 3 dB above the resonance frequency (see Fig. 3), we obtain the dielectric losses $\tan \delta = 1/Q_0$ [5]. Fig. 2 shows the losses for different dielectrics characterized in the present work. For all investigated materials (Nb_2O_5 and SiO), no dependence of the losses on the dielectric film thickness was found. This is not surprising for such lossy amorphous materials and shows that the bulk losses exceed the interface losses by far. In the future we will investigate further materials like SiO_2 , SiN_x , a/nc-Si:H and a/nc-SiC:H fabricated with varying parameters. These dielectrics are viewed as more promising because of fewer OH defects [1] and a more constrained lattice [2].

Dielectric losses can also be given by the imaginary part of the complex susceptibility χ'' . The Debye picture of non-interacting ideal dipoles with the same relaxation time τ leads to a frequency dependence

$$\chi'' \propto \frac{1}{1 + i\omega\tau}. \quad (1)$$

In this picture, the losses are maximal at a peak frequency $\omega_p = 1/\tau$. It is a general rule that the frequency dependence of dielectric loss in almost all materials is given by fractional power laws. For GHz frequencies it is found that for $\omega \gg \omega_p$:

$$\chi'' \propto \omega^{n-1} \quad \text{with} \quad 0 < n < 1. \quad (2)$$

This is usually referred to as the 'universal law' [6, 7]. The value of the exponent n depends on the nature of the TLSs as well as their coupling to each other. While it seems clear that the TLSs in amorphous thin films are dipoles, the coupling range remains unclear. The universal law predicts exponents $n = 0$ for non-interacting (Debye-like) dipoles, $n \sim 0.5$ for nearest-neighbour interactions and $n > 0.6$ for many-body interactions. As illustrated in Fig. 2 by the fits (solid lines), the universal law $\tan \delta \propto \omega^{n-1}$ is fulfilled for all investigated dielectrics with exponent values $0.65 \leq n \leq 0.69$ (see [5] as well). This is close to what is predicted within this model for dipoles with many-body interactions. Such a behaviour can be expected for the investigated amorphous and hence

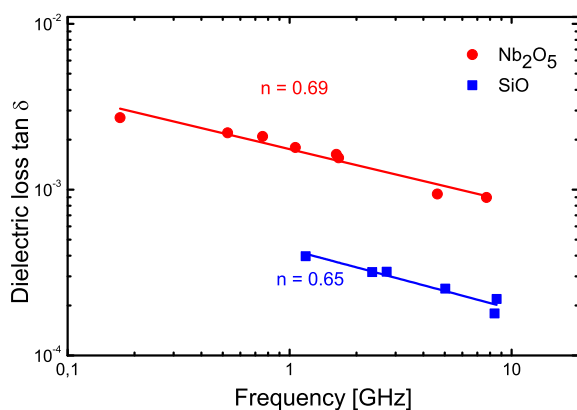


Figure 2: Frequency dependence of dielectric losses in Nb_2O_5 and SiO amorphous thin films at 4.2K. The data are in agreement with the universal law and the exponents n are in the expected range [5].

glass-like materials. This result should be considered for modelling of TLSs in Josephson circuitry.

As qubits operate at very low temperatures (mK) and energies (single photon power), there is the need to carry out loss measurements at low temperatures and energies. We will achieve this goal by using a dilution cryostat working at mK temperatures in order to learn more about loss mechanisms influencing the coherence times of qubits. We hope to quantitatively compare dielectric losses of qubits and resonators fabricated in the same fabrication process. For the investigation of the frequency dependence of losses, we have developed a sample design with multiple resonators connected in series (see Fig. 3). We have also developed amplifiers with a wide bandwidth of 20 MHz to 12 GHz which will be employed for this purpose.

As dilution cryostat measurements are time consuming and won't cover full range of materials and frequencies, we perform complimentary experiments at 300 mK by using a He-3 cryostat.

As mentioned above, TLSs may also exist on metal surfaces [3]. The corresponding losses can be measured using coplanar waveguide (CPW) resonators on low-loss single-crystalline substrates offering higher intrinsic quality factors. We are developing a suitable CPW resonator design to change the surface properties by nitridization, passivation or damaging in order to see how the TLSs and there-with the loss will be influenced.

The final goal in the present work will be to fabri-

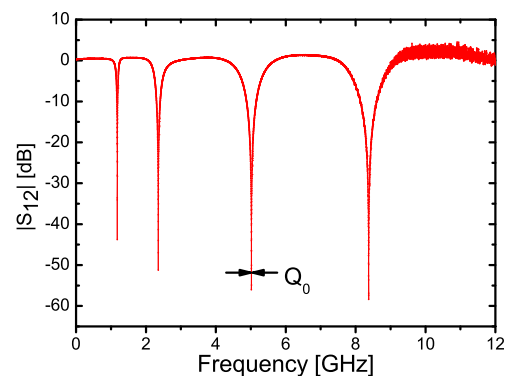


Figure 3: A typical measurement with four resonances measured in series, with illustration of Q_0 .

cate phase qubits with improved coherence time extending to μs range.

- [1] J.M. Martinis, K.B. Cooper, R. McDermott, M. Steffen, M. Ansmann, K.D. Osborn, K. Cicak, S. Oh, D.P. Pappas, R.W. Simmonds and C.C. Yu *Phys. Rev. Lett.* **95**, 210503 (2005)
- [2] A.D. O'Connell, M. Ansmann, R.C. Bialczak, M. Hofheinz, N. Katz, E. Lucero, C. McKenney, M. Neeley, H. Wang, E.M. Weig, A.N. Cleland and J.M. Martinis *Appl. Phys. Lett.* **92**, 112903 (2008)
- [3] J. Gao, M. Daal, A. Vayonakis, S. Kumar, J. Zmuidzinas, B. Sadoulet, B.A. Mazin, P.K. Day and H.G. Leduc *Appl. Phys. Lett.* **92**, 152505 (2008)
- [4] W. Chen, D.A. Bennett, V. Patel and J.E. Lukens *Supercond. Sci. Technol.* **21**, 075013 (2008)
- [5] Ch. Kaiser, S.T. Skacel, S. Wnsch, M. Siegel, R. Dolata, B. Mackrodt and A. Zorin submitted to: *Supercond. Sci. Technol.* (2009)
- [6] A.K. Jonscher *J. Phys. D: Appl. Phys.* **32**, R57–R70 (1999)
- [7] K.L. Ngai, A.K. Jonscher, C.T. White *Nature* **277**, 185 (1979)

¹ Institut für Mikro- und Nanoelektronische Systeme, Karlsruher Institut für Technologie, Hertzstraße 16, D-76187 Karlsruhe, Germany

² Center for Functional Nanostructures, Karlsruher Institut für Technologie, Wolfgang-Gaede-Straße 1a, D-76128 Karlsruhe, Germany

³ Consiglio Nazionale delle Ricerche, Istituto di Cibernetica "E. Caianiello", Via Campi Flegrei 34, I-80078, Pozzuoli (Na)

Lifetimes of magnetic excitations in Fe and Co atoms and clusters on Pt(111)

T. Schuh, T. Balashov, T. Miyamachi, S. Suga¹, W. Wulfhekel

Recent investigation of single atoms and clusters on Pt(111) show giant magnetic anisotropy energies (MAE) [1,2]. This raised the hope of an magnetic stable atom. However, the lifetimes of the excited states and magnetization dynamics were not investigated so far, playing an important role for the stability. We use scanning tunneling microscopy (STM) with a high lateral resolution to probe single atoms, dimers and trimers. The magnetization dynamics can be investigated with inelastic tunneling spectroscopy (ITS). In this report the lifetimes of the excited magnetic states and the decay mechanisms are described.

For preparation, small amounts of Fe or Co were deposited on an atomically clean Pt(111) crystal at 4.3 K, resulting in isolated atoms. The capabilities of atomic manipulation with the STM were used to create dimers and trimers [3]. To describe these systems the effective spin Hamiltonian DS_z^2 ($D < 0$) is used with S_z as the z-component of the spin and D the quantummechanical MAE constant.

During the tunneling process, electrons may exchange angular momentum (spin) with the magnetic cluster or atom [4]. As a result of such an inelastic spin-flip scattering, electron changes the spin of the atom or cluster from the ground state $S_z = \pm S$ ($S_{Fe} = 3/2$, $S_{Co} = 1$) to the excited state $S_z = \pm(S-1)$. The energy of the inelastic spin-flip process E_{sf} is the difference between these two states and can be measured with ITS. For metallic systems, elastic tunneling leads to a linear increase in tunneling current I upon increasing the bias voltage U in the low bias regime. When the energy eU reaches E_{sf} , an additional inelastic tunneling channel opens. As a consequence, the slope of $I(U)$ is slightly increased for $eU > E_{sf}$. This change is usually too small to be identified directly. It can, however, be seen as a extrema in d^2I/dU^2 independent of the tunneling direction. d^2I/dU^2 spectra were recorded for Fe atoms and the bare Pt surface (crosses in Fig. 4 inset). The genuine excitation spectra 4 a) and 4 b) were obtained by subtracting the Pt background spectrum from the Fe and Co spectrum, respectively. The excitation energies can be determined from the maximum/minimum of the spectra and with the correspondance principle, the classical MAE can be extracted. Further, similar experiments for dimers and trimers give their classical MAE [2]. One notices that not only the positions of the peaks changes for the

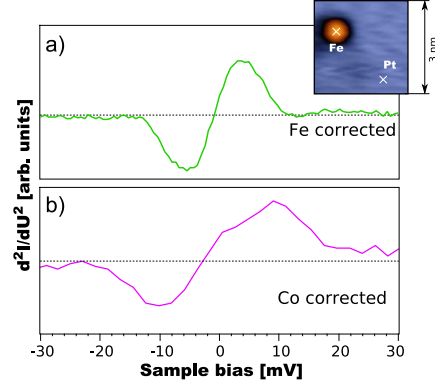


Figure 4: Topography of a single Fe atom on Pt(111) (inset), corrected d^2I/dU^2 of a) Fe and b) Co atom

Fe and Co spectra 4 a,b), but also their widths. The width W depends on the intrinsic width W_{in} and an experimental broadning from the temperature T and the lock-in amplifier U_{mod} . The intrinsic width W_{in} is given by the lifetime τ of the excitation via the uncertainty principle $\tau W_{in} \geq \hbar/2$. Since the T and U_{mod} are known, one can calculate τ [5]:

$$\tau \geq \frac{\hbar}{2\sqrt{W^2 - (5.4kT)^2 - (1.7eU_{mod})^2}}$$

This procedure, applied to the observed excitations, gives the lifetimes as detailed in Table 3. All the values are of the order of tens of femtoseconds. As the width of the peaks tends to disperse more than the peak position, the precision of the values is around ± 5 fs.

To relax the magnetically excited atom or cluster back to the ground state, spin angular momentum has to be transferred to the substrate. This can be achieved by spin-orbit interaction or much easier via spin-flip scattering of conduction electrons of the substrate, shown in Fig. 5 a) (dashed arrows) for the case of Fe. This process is similar to the excitation mechanism. The electron that is scattered is, however, not provided by the tunneling current but by the Fermi sea of the substrate. Hence, an electron of the atom or cluster transfers the $\Delta S_z = \pm 1$ and energy to a conduction electron. The strong hybridization of the Fe or Co states with the Pt(111) substrate bands results in short lifetimes. The excitation lifetimes tend to decrease with increasing cluster size. The only exception from this rule is the lifetime of a single excited

	atom	dimer	trimer	dimer non-collinear
Fe	55	45	30	10
Co	20	45	30	

Table 3: Lifetimes of excited states of atoms and clusters in fs

Co atom that is noticeably smaller than the value for the Fe atom. The reason for this effect lays in the spin configuration of the excited state (Fig. 5 b)). An excited Co atom has $S_z = 0$, and can thus relax into both ground states with $S_z = \pm 1$. All the other clusters have a spin higher than 1 and the excited state can only relax in one direction. This would effectively halve the lifetime of the excited state of Co with respect to other clusters, in good agreement with the measured values. A further reduction of the lifetime is caused by a stronger hybridization of Co with the substrate.

In the case of an Fe dimer, the total dimer spin is composed of the two spins of the individual atoms. In the ground state, both spins align in parallel. For simplicity, we assume that both spins have a maximal spin of $s = 3/2$. The interaction with an electron leads to a transition from a ground state $|s, s\rangle$ to a superposition of states, where the spin of one of the composing atoms is changed by one, namely $|s, s-1\rangle$ and $|s-1, s\rangle$. There are two linear combinations of these states that form an eigenstate of the Heisenberg Hamiltonian including the exchange constant J

$$\Psi_1 = \frac{1}{\sqrt{2}} |s, s-1\rangle + \frac{1}{\sqrt{2}} |s-1, s\rangle, \quad (3)$$

$$\Psi_2 = \frac{1}{\sqrt{2}} |s, s-1\rangle - \frac{1}{\sqrt{2}} |s-1, s\rangle. \quad (4)$$

The energies of the two states differ by $3J$, so two inelastic excitation signatures are expected in the spectrum.

The cluster in the first state has a total spin of $S = 2s$ and the z projection $S_z = 2s - 1$. Thus, this state can be described as a rotation of the total spin of the cluster in the analogy to the excitation of an individual atom.

In the second state the dimer has a spin of $S = S_z = 2s - 1$. The energy of the state is higher due to the exchange interaction between the two spins coming into play. The total energy cost of this excitation is a sum of the exchange and the anisotropy contributions, $E_x = 2Js - D(4s - 1)$. Indeed a second peak is observed for Fe dimers, as shown on Fig. 6. An excitation energy of $54 \pm 2\text{meV}$, is observed giving a J of $16 \pm 1\text{meV}/\hbar^2$. The non-collinear state has the shortest lifetime of all. A likely reason for this is given by two possible ways for decaying: spin-flip and non-spin-flip. The spin-flip process is the

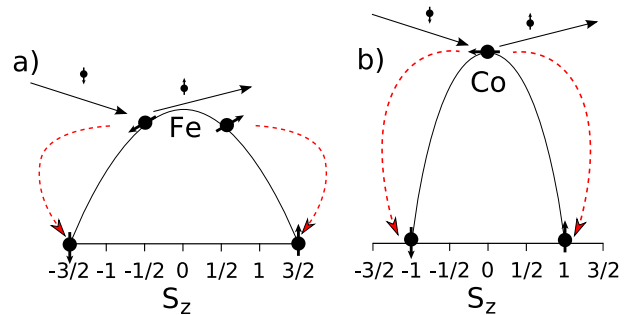


Figure 5: Scheme of relaxation processes for a) Co and b) Fe atoms

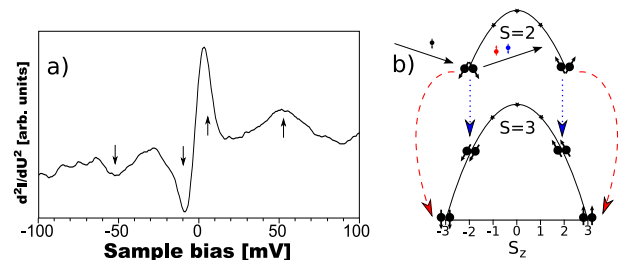


Figure 6: a) Inelastic spectrum taken on an Fe dimer, with two inelastic excitations visible at $\approx \pm 5$ meV and $\approx \pm 50$ meV as indicated by the arrows. b) Scheme of relaxation processes for an Fe dimer

inverse process of the excitation similar to the relaxation discussed above, relaxing to the ground state (see dashed arrows Fig. 6b). Due to conservation of spin moment, only the majority electrons can relax the cluster. The non-spin-flip relaxation leads to a decay to the collinear excited state, keeping S_z but changing the phase of the dimer spin wavefunction (dotted arrow). Thus electrons of both spins can de-excite the non collinear dimer state via non-spin flip scattering, doubling the scattering probability.

These lifetimes give information on the magnetization dynamics of the atoms and clusters. The strong hybridization of the atomic states with the Pt substrate states leads to efficient electron-electron scattering processes that relax the magnetic state of the atom. One can conclude that the magnetic states are not stable in spite of the high MAE's due to the short lifetimes.

- [1] P. Gambardella *et al.* Science **300**, 1130 (2003)
- [2] T. Balashov *et al.* Phys. Rev. Lett. **102**, 257203 (2009)
- [3] D. M. Eigler *et al.* Nature **344**, 524 (1990)
- [4] A. J. Heinrich *et al.* Science **306**, 466 (2004)
- [5] J. Klein *et al.* Phys. Rev. B **7**, 2336 (1973)

¹ Osaka University, Japan

Giant magneto resistance of single molecules measured with spin-polarized STM

Stefan Schmaus, Yasmine Nahas, Annika Bork, Toyo Kazu Yamada, Wulf Wulfhekel

Nowadays essential challenges of nano electronics are to realise and to measure systems of extreme size with interesting electronic properties. Using single molecules to build electronic devices is a fundamental approach to nano electronics to further downsizing electronic systems [1]. A second outstanding development, in particular in data storage techniques, is based on the electron spin to realise functions. This field of spintronics was initiated by the discovery of the giant magneto resistance (GMR) in thin metallic films [2, 3] and now plays an important role in modern applications. A combination of both approaches, i.e. molecular spintronics, is a field in its infancy. In this work, we realise for the first time molecular GMR junctions consisting of two ferromagnetic electrodes bridged by a single organic molecule.

Scanning Tunnelling Microscopy (STM) has been used as a powerful tool to measure electronic properties of single molecules. It allows the direct addressing of single molecules and by contacting with the tip to measure molecular conductances [4, 5]. We use a spin polarised STM to measure transport properties of single molecules in dependence of spin polarisation of the electrodes, i.e. a magnetic surface and a spin-polarised STM tip. The experiments were carried out in an home built STM working in ultra high vacuum (UHV) and at 4K. As tip we used a wet etched W tip coated by a thin Co film of ≈ 10 monolayers (ML) thickness. As substrate we used a Cu(111) single crystal on which we deposited a sub-monolayer amount of Co with molecular beam epitaxy. This yield the formation of bilayer islands of Co with exhibit an spontaneous out-of-plane magnetisation. Due to a strong surface anisotropy there are two stable magnetisation states, magnetisation out of the surface plane either pointing to the vacuum or do the substrate direction [6]. Thus, the Co islands naturally provide magnetic electrodes with two spin polarisation directions. Onto these surfaces hydrogen phthalocyanine (Pc) molecules were deposited in situ from a Knutsen cell heated to ≈ 500 K. Fig. 1a shows the STM topography of the sample after depositing molecules. The molecules are recognised by their shape showing the four aromatic sidegroups [5].

By using Co coated tips the direction of magnetisation direction of the individual islands can be determined. dI/dV curves were measured on the bare islands with the lock-in technique. The differential

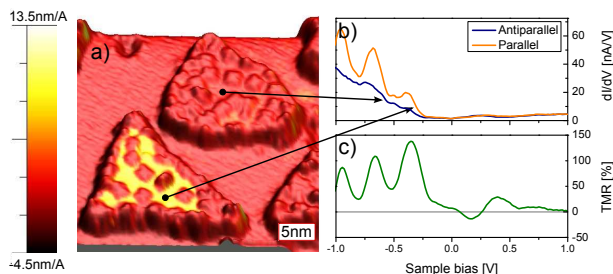


Figure 1: a) Topographic image of two Co islands on the Cu(111) surface. The colour code displays the measured dI/dV map at -310 mV. One can distinguish between parallel (yellow) and antiparallel (red) magnetisation of the islands with respect to the tip. b) shows the dI/dV spectra taken on two contrarily magnetised islands. In c) the optimistic TMR ratio calculated from the dI/dV spectra is plotted. The highest value is measured at around -350 meV. This is used to distinguish between the two different magnetised islands.

conductivity dI/dV is proportional to the local density of states (LDOS) within the Tersoff Hamann model. Especially at surface states or bulk band edges appearing as peaks in the dI/dV spectrum the LDOS is highly spin-polarised [6]. As a result the dI/dV recorded with spin polarised tips shows a dependence of the peak intensities on the relative orientation of the sample and tip magnetisation. Fig. 1b shows the dI/dV curves for two different islands, one magnetised parallel the other antiparallel to the tip. Particularly large difference in the spectra are found at -350 meV stemming from the surface state of Co. This difference is used to detect the local magnetisation direction of Co islands by recording maps of the local differential conductivity at this voltage. The colour code of Fig. 1a represents this local differential conductivity indicating with bright areas magnetised parallel and with dark anti parallel to the tip. The tunnelling magneto resistance (TMR) defined as the difference of conductivity over the smaller conductivity of the tunnelling junction formed by the tip and sample is strongly energy dependent as depicted in Fig. 1c. Note that at small bias the TMR is only of the order of 5%.

To contact single molecules with the STM tip, we positioned the tip above a molecule at the aromatic side groups, opened the feed-back loop, and

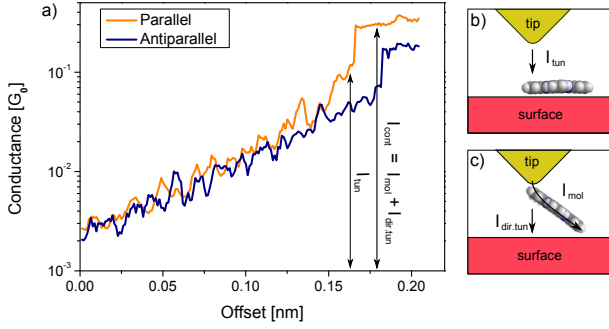


Figure 2: a) Two typical single conductance distance curves measured at two contrariwise magnetised islands with a constant tunnelling voltage of 10 mV. Below a certain tip-surface separation the curves shows a jump of the conductance to higher values. This can be identified by a jump of the molecules into contact. After the jump there are two contributions to the transport. One by the direct tunnelling between tip and surface while the other is the transport across the molecule (see c)).

approached the tip towards the molecule ($\approx 1 \text{ \AA/s}$). During this approach the tunnelling current was recorded, resulting in current distance curves. As the observed conductances of phthalocyanine molecules are rather high [5], small voltage (10 mV) has to be used to avoid thermal disintegration of the molecules. Firstly, an exponential increase of the conductance is observed, as expected due to decreasing the tunnelling barrier width (see Fig. 2). Below a certain distance — typically 3-4 \AA above the point contact — the curve shows a jump indicating a sudden change of the junction geometry. These jumps have already been seen for Pc molecules and have been identified by a lifting of the flat molecule such that it bridges the tunnel gap [5]. The current after the jump only depends slightly on the distance and represents the conductance of the molecule I_{mol} plus an additional contribution from direct tunnelling between tip and sample $I_{\text{dir.tun}}$. This conductance in contact depends on the relative orientation of the magnetisation of tip and sample (see Fig. 2). For the parallel case the conductance is found to be around $0.30 G_0$ while in the anti parallel case it is slightly smaller ($0.17 G_0$). To eliminate the spin dependent direct tunnelling part, the measured tunnelling current I_{tun} before the jump is subtracted from that after I_{cont} . By this the spin dependent conductance of the molecule can be calculated $I_{\text{mol}} \approx I_{\text{cont}} - I_{\text{tun}}$.

To ensure to work with the same tip, measurements on two different Co islands with perpendicular

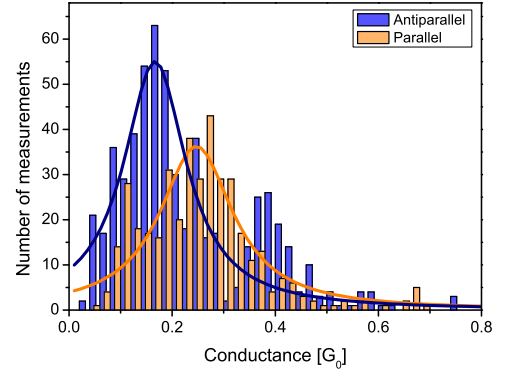


Figure 3: Histogram the corrected molecular conductances (397 times parallel / 576 times anti parallel). A Lorentzian fit is used to determine the conductance and calculate the GMR ratio.

magnetisation were done in the same scan. This measurement has been repeated and the distribution of the observed molecular conductance is depicted in Fig. 3. The observed scatter of the conductance, be it due to noise of the current measurement or to slightly different binding geometries of the molecule to the tip, is small when compared to previous work [4]. The scatter of a single measurement is of similar order as the difference due to the magnetisation. Nevertheless, one can clearly see the difference between the two magnetisation directions. A lower tendency is observed for the anti parallel measurement. To determine the GMR from the statistical measurements Lorentzian fits were used. In the parallel case we measured an averaged conductance value of $G_p = (0.247 \pm 0.005)G_0$ and in the anti parallel case $G_{ap} = (0.167 \pm 0.005)G_0$. These values result in an optimistic GMR ratio of $\text{GMR} = \frac{G_p - G_{ap}}{G_{ap}} = (48.2 \pm 7.2)\%$. This is one order of magnitude larger than the TMR for direct tunnelling. This indicates that the molecular conductance couples to specific highly spin polarized Co states.

- [1] A. Aviram and M. A. Rattner Chem. Phys. Lett. **29** 277 (1974)
- [2] M.N.Baibich *et al.* Phys. Rev. Lett. **61** 2472 (1988)
- [3] G. Binasch *et al.* Phys. Rev. B **39** 4828 (1989)
- [4] W. Haiss *et al.* Nature Mat. **5** 995 (2006)
- [5] A. F. Takács *et al.* Phys. Rev. B **78** 233404 (2008)
- [6] O. Pietzsch *et al.* Phys. Rev. Lett. **92** 57202 (2004)

Structure and local electronic properties of Ag islands and Co/Ag on Nb(110)

T. Tomanic, C. Sürgers, H. v. Löhneysen

The local variation of the superconductive order parameter in hybrid structures of a superconductor S in contact with a normal metal N or ferromagnet F is a topic of current interest. We investigate Ag and Co islands on the (110) surface of superconducting Nb via low-temperature scanning tunneling microscopy (STM) and spectroscopy (STS).

The preparation of a clean and oxygen-free Nb (110) surface is a challenge. It is difficult to obtain an oxygen-free Nb surface by Ar^+ -sputtering and subsequent annealing in ultra-high vacuum (UHV) [1] due to the high solubility of oxygen in Nb and the segregation of oxygen at temperatures above 600 K. However, oxygen-free Nb (100) surfaces have been obtained by flash heating to temperatures up to 2500 K [2]. In order to achieve such a high temperature for our Nb (110) crystals, a small electron gun was built to heat the samples up to temperatures of 2800 K by electron bombardment of the back of the Nb crystal through a window in the sample holder. The set-up provides optical access to the sample surface to check the temperature by means of an optical pyrometer during flash heating. The setup is attached to the preparation chamber (base pressure $< 10^{-10}$ mbar) on a single flange and allows cleaning of the Nb crystal and subsequent deposition of Ag and/or Co on Nb (110).

The Nb (110) single crystal, with a diameter of 6 mm and a height of 1 mm, was attached to a substrate holder with a window of 5 mm diameter and was cleaned by repeated cycles of Ar^+ sputtering and heating to 1100 K. The final flash heating with the e-gun takes 1-2 minutes for reaching a temperature of 2500 K, which is then kept constant for 1 minute and turned off within 30-40 seconds. Figure 1 shows an STM image taken at room temperature after this cleaning process. Highly ordered atomic chains of 10 ± 1 atoms are visible which are oriented along the Nb $[\bar{1}\bar{1}1]$ direction. In the perpendicular direction, the chains are repeated every 3 atomic rows, thus forming 10×3 supercells. Auger spectroscopy on Nb single crystals cleaned in this way show oxygen concentrations below 5 %.

A nominal thickness of 5 nm Ag was deposited onto the flash-heated Nb surface with a rate of 1 nm/min at a substrate temperature $T_S = 500 - 600$ K. The growth of Ag (111) on Nb (110) in this temperature range is of Stranski-Krastanov type in agreement with the growth behavior observed for the

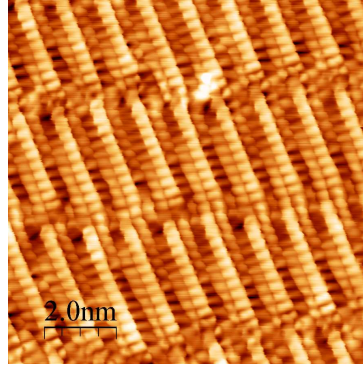


Figure 1: STM image (10 nm \times 10 nm) of a Nb (110) single crystal with surface reconstruction after cleaning.

similar heteroepitaxial system Ag/W(110) [3]. Large Ag islands are formed after the surface is covered by nominally 1-2 monolayers of Ag. Fig. 2 shows two height profiles along the major axes of an Ag island with two large steps imaged at room temperature. The surface of these islands exhibits a number of monatomic steps although the atomic order was not resolved. For $T_S = 600$ K, the surface is covered by 25 % with Ag islands of 200 nm in diameter and 20 nm in height. At a lower $T_S = 500$ K they are typically 100 nm in diameter and 10 nm in height with a coverage of 50 %. The corresponding increase of island density by almost one order of magnitude is in agreement with the temperature-dependent island density of Ag/W (110) reported earlier [3].

Tunneling spectroscopy was performed at $T = 3$ K on the virgin Nb (110) surface and on Ag islands (not shown). We only mention that the characteristic tunneling spectrum of a superconductor with an energy gap at the Fermi energy E_F was resolved. The width of the gap decreases with increasing island height as expected from the superconducting proximity effect. This will be further investigated in detail.

Fig. 3 shows tunneling spectra acquired at room temperature on top of the Ag island at the indicated positions 1, 2, and 3. With increasing positive voltage applied to the sample, a step-like behavior followed by a number of oscillations is observed. (The apparent gap around zero bias is due to glitches produced by the STM electronics when crossing $V = 0$ and is removed in all subsequent measurements). The step

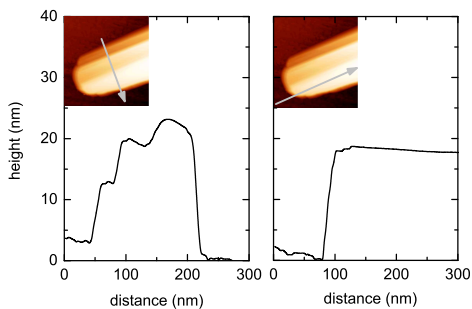


Figure 2: Height profiles along the indicated lines (arrows) of an Ag island after deposition of 5 nm Ag on Nb (110) at $T_S = 600$ K. STM image size: $200 \text{ nm} \times 200 \text{ nm}$.

marks the lower edge of the L -gap surface state observed by STS on bulk Ag (111) at -67 meV below E_F [4]. In the present case, the band edge is strongly shifted upward to 25 - 45 meV above E_F [4] possibly due to the residual strain in the surface region of the islands [5]. This shift of 100 meV corresponds to an in-plane tensile strain of $\Delta a/a = 0.75\%$ as inferred from a previous photoemission study on epitaxial Ag (111) films [4]. This strain is conceivable even for an island thickness of ≈ 20 nm height due to the strong lattice mismatch between bcc-Nb (110) (in plane next-neighbor distances $r_{NN} = 2.86 \text{ \AA}$ and 3.3 \AA) and fcc-Ag (111) ($r_{NN} = 2.89 \text{ \AA}$).

The additional oscillations with a period of ≈ 25 meV are attributed to discrete quantum well-states (QWS) of electrons which are confined by the island perimeter as well as by the surface band gap in [111] direction [5 - 7]. The energies of the QWS depend on the total phase shift at the boundaries and on the surface band structure. QWS have been observed by photoemission on atomically uniform Ag (111) films up to thicknesses of 115 monolayers on Au (111) [6]. In the present case, a height of 20 nm corresponds to 85 monolayers. Further measurements on islands of well-defined shape and height are required in order to understand the position-dependent energy of the surface-state band edge (Fig. 3) and to allow a quantitative analysis of the QWS.

Co was deposited with a nominal thickness of 0.2 monolayers on Nb (110)/Ag (111) at room temperature. The STM images reveal a cluster growth of Co on Ag. Fig. 4 shows an image after heating to 500 K. Due to the enhanced mobility the clusters have migrated to the island edges forming chains. The chains show a very regular pattern with Co clusters of distinct size and distance to each other. Measurements over a long period of time (about one day) did

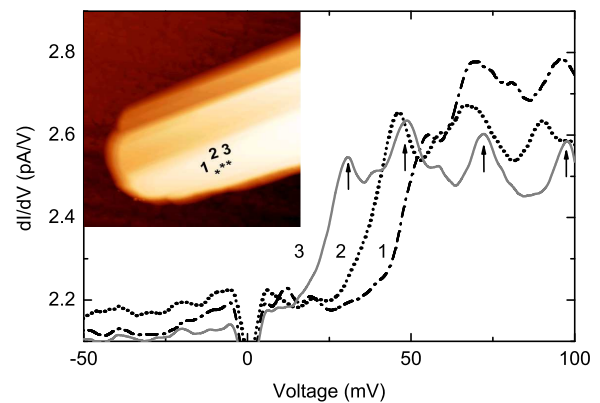


Figure 3: dI/dV vs. sample bias acquired at different points on top of the Ag island, see STM image ($200 \text{ nm} \times 200 \text{ nm}$). Arrows indicate contributions from QWS.

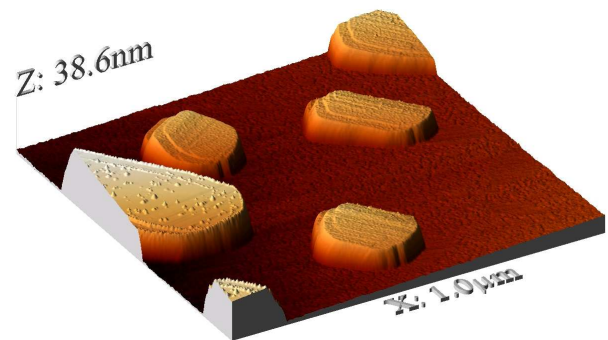


Figure 4: Ag island covered with Co clusters after heating to 500 K. The clusters form lines at the island edges.

not show further changes at room temperature. We will proceed in the determination of the local electronic properties on Co clusters on superconducting Nb and on Ag/Nb (110).

- [1] C. Srgers et al., Surf. Science **471**, 209, (2001).
- [2] B. An et al., Phys. Rev. B **68**, 115423, (2003).
- [3] G.D.T. Spiller et al., Surf. Science **131**, 517 (1983)
- [4] L. Limot et al., Phys. Rev. Lett. **94**, 036805 (2005)
- [5] G. Neuhold et al., Phys. Rev. Lett. **78**, 1327 (1997)
- [6] T.-C. Chiang, Surf. Sci. Rep. **39**, 181 (2000)
- [7] J. Li et al., Phys. Rev. Lett. **80**, 3332 (1998)

Pulse injection of air onto Cu(111) surfaces: copper oxide surface structures

C. Pérez León, C. Sürgers, H. v. Löhneysen

The deposition of organic molecules on metal substrates has been extensively studied in recent years due to the increasing interest in functional surfaces and molecular electronics. Large or reactive organic molecules cannot be sublimated thermally in ultra-high vacuum (UHV), because they tend to decompose before sublimation. A very promising alternative deposition method is pulse injection [1]. Here, a solution of the molecules under investigation is injected into the UHV chamber using a high-speed pulse valve. When the solvent enters the chamber, it vaporizes quickly ideally leaving only the molecules under investigation on the substrate surface. Compared with other solution-based deposition methods this approach has the advantage that the sample is prepared in situ, i.e., the sample is never exposed to air throughout the process. However, when the solution is introduced into the pulse valve, it is for a short time exposed to ambient atmosphere. It is difficult to avoid that a small amount of air dissolves into the solution, or that a layer of air remains between the solution and the opening of the valve, which then enters the chamber before the solution does and contaminates the substrate. Therefore, a study of the potential effects of such impurities introduced by the injected solution on a clean surface is of large interest. Here, we present the results of our investigations of the clean Cu(111) surface after injection of air by Auger electron spectroscopy (AES) and scanning tunneling microscopy (STM) for different coverages when the substrate was kept at room temperature (RT) and at elevated temperature.

In order to carry out the pulse-injection deposition, a specially designed molecular deposition chamber was used (see Ref. [2]). The base pressure in the deposition chamber was lower than 1×10^{-9} mbar. For the injection of air, the sample was placed in a horizontal position 10 cm below the nozzle of the pulse valve. The valve was opened for a short time of 10 ms, once or several times, in intervals of several minutes, i. e., the time needed for recovering the base pressure. During the opening of the valve the pressure increased to $< 1 - 5 \times 10^{-6}$ mbar and recovered within a few minutes. After completion of the deposition, the sample was transferred to the analysis chamber where the base pressure was lower than 1×10^{-10} mbar. AES spectra reveal that mainly oxygen is adsorbed on the copper surface. In various experiments a small to medium carbon peak was observed that can be ascribed to CO_2 or to impurities

such as dust that are present in ambient atmosphere.

Fig. 1 shows STM images of the Cu(111) surface after exposure to air. The morphology of the copper surface is strongly affected by the exposure. The step edges are not straight but rather angled, often with an acute-angled shape, Fig. 1 (a). These changes are accompanied by the appearance of fringes at the step edges, whose contrast and apparent height strongly depend on the tunneling parameters. In Fig. 1 (a, b) they appear to be slightly deeper than the lower terrace of the step. In addition to these changes at step edges bright and dark islands show up on terraces. The bright islands show a contrast similar to that of the structure at step edges, whereas the darker ones show an apparent lower depth close to one atomic step Fig. 1 (a-d). The shape and internal structure of such features are strongly influenced by the substrate temperature during deposition and by the oxygen coverage.

The observed effects and new structures correspond to the formation of copper oxide or oxide precursors resulting from the interaction of the oxygen with the Cu surface [3, 4]. At step edges, the oxygen reacts with the Cu atoms of the upper terrace. These atoms are incorporated into the oxide islands which grow in the lower terrace edging the borders of the upper step. We denote this oxide as “step oxide”. However, oxide islands also appear on the terraces. Such oxide islands can nucleate from vacancy islands or atomic defects at the surface, which act as step edges. Therefore, oxide is formed on the lower terrace which gives rise to a very dark contrast. This kind of oxide, denoted as “terrace oxide”, displays a somewhat triangular form whose edges are parallel to the symmetry directions of the (111) copper plane. In addition, there are bright islands on the terraces. These correspond to a third kind of oxide, denoted as “added oxide”. It results from the reaction of oxygen with the excess of copper atoms liberated by the formation of the “step” and “terrace oxides”. Its different formation process leads to irregularly shaped islands rather than to triangular ones.

In Fig. 1 (c,d) height profiles of the copper surface exposed to air are presented. They confirm that the oxide islands have a lower height than the terrace in which they are grown. The apparent depth depends on the tunneling parameters and is 0.069 and 0.047 nm, in (c) and (d), respectively. However, in Fig. 1 (e) and (g), they appear to be higher than

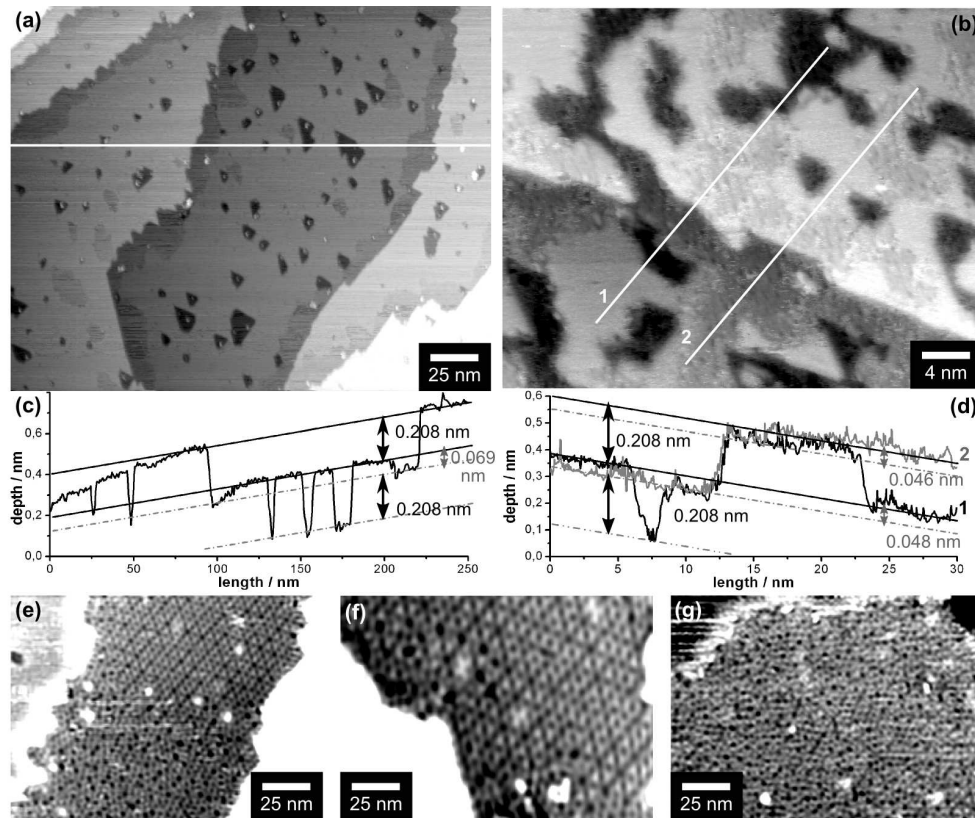


Figure 1: STM images of the Cu(111) surface after exposure to air: (a) Exposure at $\sim 200^\circ\text{C}$. Tunneling current 0.7 nA and tunneling bias -36 mV. (b) Exposure at RT, 0.2 nA, 0.5 V. (c,d) Height profiles along the white lines in (a) and (b) respectively. (e-g) STM images of the internal structure of the different oxides after exposure at $\sim 200^\circ\text{C}$ for low coverages with a tunneling current of 0.7 nA: (e) Step oxide, 0.9 V. (f) Terrace oxide, -0.9 V. (g) Added oxide, 0.9 V. (See text for details.)

the terrace. Such changes of the contrast are known for thin oxide films on metallic surfaces, especially in the vicinity of the valence or conduction band edges, where contributions from the oxide film and metallic substrate to the current vary greatly. The dark islands (“terrace oxide”) display a depth of one atomic step in addition to the depth of the oxide (0.208 nm), since they grow in the lower terrace.

At low coverages, the three different kinds of oxide (“step”, “terrace”, and “added” oxides) produced at RT are well distinguished, see Fig. 1 (a). For higher coverages [Fig. 1 (b)], we observe two types only since the “step oxide” and “added oxide” appear mixed and show the same shape and image contrast. In the poorly ordered oxide structures only locally ordered domains with a hexagonal lattice (not shown) are observed.

In contrast, surface oxides produced at higher temperature ($\sim 200^\circ\text{C}$) exhibit highly ordered structures. Fig. 1 (e–g) displays the internal structure of the different oxides obtained in atomic resolution with a nearest-neighbour distance of 0.55–0.65 nm. The “terrace oxide” and “step oxide” show large domains with a hexagonal lattice, whereas “added ox-

ide” displays a much lower order.

The internal structure of the oxides depends strongly on the tunneling parameters. This can be attributed to the fact that in oxides, electronic states are generally more localized than on pure metal surfaces, resulting in sharper features in the LDOS which give rise to a strong voltage dependent image contrast. This renders the identification of atomic-scale patterns, based on the lattice constant and known symmetry of the imaged patterns, difficult. In our measurements, the ordered lattice corresponds to a strained $\text{Cu}_2\text{O}(111)$ lattice that coincides with the Cu(111) substrate.

[1] H. Tanaka, T. Kawai, *J. Vac. Sci. Technol. B* **15** 602 (1997).

[2] C. Pérez León, C. Sürgers, M. Mayor, M. Marz, R. Hoffmann, H. v. Löhneysen, *J. Phys. Chem. C* **113** 14335 (2009).

[3] T. Matsumoto, R.A. Bennett, P. Stone, T. Yamada, K. Domen, M. Bowker, *Surf. Sci.* **471** 225 (2001).

[4] F. Wiame, V. Maurice, P. Markus, *Surf. Sci.* **601** 1193 (2007).

Low temperature dielectric properties of $^{88}\text{Sr}^{48}\text{TiO}_3$

F. Aslan, T. Peichl, G. Fischer, S. Schöllhammer¹, W. Menesklou¹ and G. Weiss

It is well established that the behavior of amorphous solids at low temperatures is governed by atomic two-level tunneling systems with properties as detailed in the phenomenological tunneling model [1]. However, this genuine tunneling model cannot explain the recently measured magnetic field dependence of the low temperature dielectric properties of glasses [2]. Extensions of the tunneling model [3] that include a coupling of the lateral motion of the atoms to the orientation of their nuclear quadrupole moment could explain at least some of the observed magnetic field effects, in particular dielectric echo-experiments in the frequency range of 1 GHz [4] but failed so far to explain the low frequency experiments [5]. In our studies, we try to demonstrate directly the role of nuclear quadrupole moments by comparing the dielectric behavior of SrTiO_3 -ceramics made of isotopes of natural abundance with that of samples enriched with the isotopes ^{88}Sr (99.25%) and ^{48}Ti (99.8%) which have no nuclear quadrupole moment. In contrast to the expectation, the magnetic field effects of the dielectric constant of $^{88}\text{Sr}^{48}\text{TiO}_3$ were not smaller but even 4.5 times larger than those of SrTiO_3 with natural components.

Our samples were produced from SrCO_3 and TiO_2 powders in the solid state reaction (calcination) $\text{SrCO}_3 + \text{TiO}_2 \rightarrow \text{SrTiO}_3 + \text{CO}_2$ and subsequent sintering. SEM studies of the powder reagents revealed that the particles of the natural and isotopically enriched powders differed both in size and structure. By ball milling with zirconia spheres the particle sizes were equalized and then mixed in stoichiometric proportion. For calcination, the mixed powders were brought to 1050°C for about 15 h. The produced strontium titanate powder was compressed to pills and sintered at temperatures between 1350°C and 1450°C for about 10 h. Figure 1 shows by four examples the dependence between grain sizes and sintering temperature of our SrTiO_3 ceramics. Independent of the isotopic composition we find grain sizes of the order of $10\ \mu\text{m}$ at 1400°C .

For dielectric measurements we used an Andeen-Hagerling capacitance bridge at a frequency of 1 kHz and a driving AC-voltage of $U = 50\ \text{mV}$ corresponding to electrical fields of about $E = 80\ \text{V/m}$ for our sample geometry. To capture the magnetic field dependencies, field sweeps 0 to 2 T at rates of 0.01 and 0.001 T/s were performed. Here, only the real part of the dielectric constant will be presented, measured by the capacitance of our samples.

In figures 2 and 4, for various temperatures be-

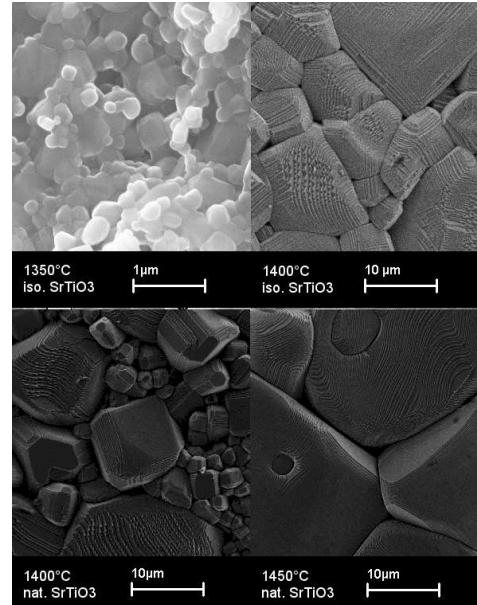


Figure 1: SEM pictures to illustrate the dependence of grain size on sintering temperature of our SrTiO_3 ceramic samples with both isotopically enriched and natural composition, iso- SrTiO_3 and nat- SrTiO_3 , respectively.

tween 50 mK and 300 mK, relative changes of the capacitance as a function of magnetic field are shown of two capacitors made of nat- SrTiO_3 and of enriched $^{88}\text{Sr}^{48}\text{TiO}_3$, respectively. In both samples the dielectric constant passes a shallow maximum before it decreases rapidly to a lower value at magnetic fields around 100 mT. The changes are of the order of 10^{-3} and become significantly smaller with increasing temperature. At the same time the drop off shifts to higher magnetic field values as indicated by the arrows. Both, the gradual vanishing with temperature and the shift to higher magnetic fields of significant features of the dielectric constant have been observed in previous experiments on glasses [2] and SrTiO_3 based ceramics [6].

Comparing figures 2 and 4, we observe a remarkable similarity which proves that this effect has a common physical origin. Moreover, since this effect is about 4.5 times larger in the $^{88}\text{Sr}^{48}\text{TiO}_3$ sample, it is clearly not produced by nuclear quadrupole moments coupling to the tunneling motion of the respective atoms.

Figures 3 and 5 show the temperature dependence

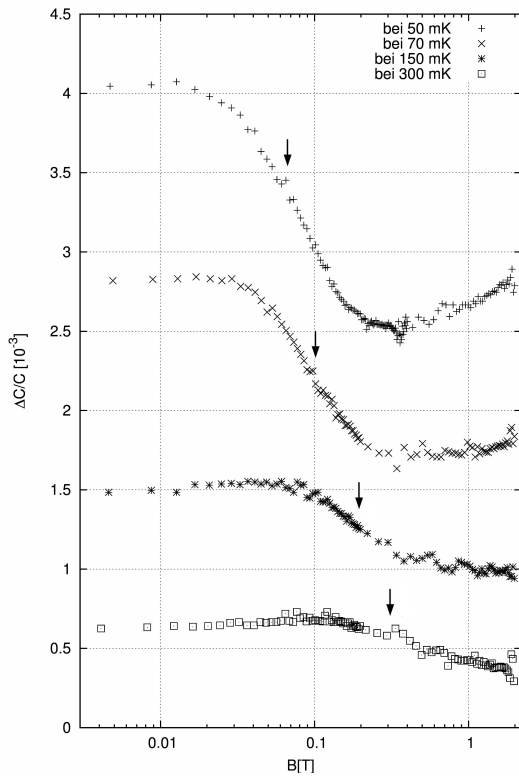


Figure 2: Relative magnetic field dependence of the dielectric constant (measured as capacitance changes) of nat-SrTiO₃ at several temperatures as indicated. Data sets are arbitrarily shifted for better presentation.

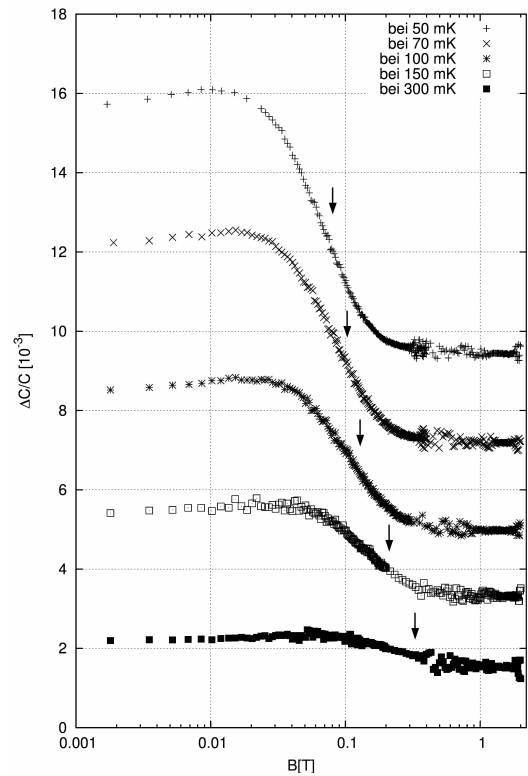


Figure 4: Relative magnetic field dependence of the dielectric constant (measured as capacitance changes) of enriched ⁸⁸Sr⁴⁸TiO₃ at several temperatures as indicated. Data sets are arbitrarily shifted for better presentation.

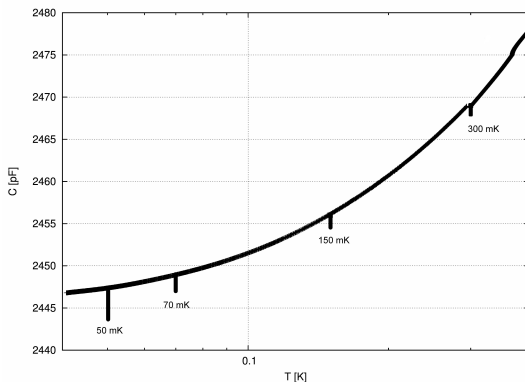


Figure 3: Temperature dependence of the capacitance of the sample made from nat-SrTiO₃. Vertical lines at indicated temperatures mark the changes induced by a magnetic field sweep from 0 to 2 T.

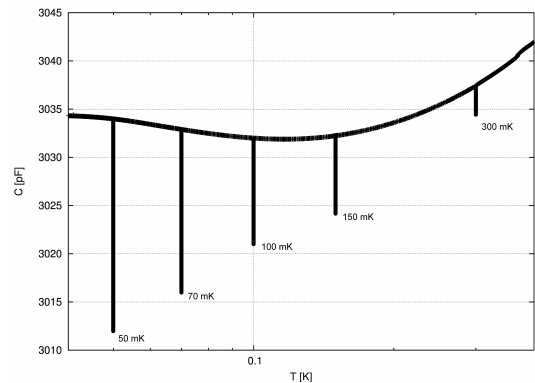


Figure 5: Temperature dependence of the capacitance of the sample made from ⁸⁸Sr⁴⁸TiO₃. Vertical lines at indicated temperatures mark the changes induced by a magnetic field sweep from 0 to 2 T.

of the capacitance of the two samples and the respective changes that are induced by the magnetic field at a given constant temperature. In contrast to the capacitor made of nat-SrTiO₃ the capacitance of the ⁸⁸Sr⁴⁸TiO₃ sample passes a minimum at 120 mK reflecting more closely the usual behavior of glasses. It is well conceivable that slightly different preparation procedures and the unequal grain sizes of the raw materials are responsible for this difference. The more pronounced 'glassiness' implies, for energies below about 100 mK, a higher density of states of tunneling systems in the ⁸⁸Sr⁴⁸TiO₃ sample than in nat-SrTiO₃.

Having ruled out nuclear moments to cause the magnetic field dependence we may ask whether electronic magnetic moments play any role. SQUID-magnetometer measurements revealed that our ⁸⁸Sr⁴⁸TiO₃-material contains about 6 times more ferromagnetic and two orders of magnitude more paramagnetic impurities than our SrTiO₃ with natural isotopic composition. From previous experiments [7] it has been concluded that magnetic impurities have no influence on the dielectric behavior but recent theoretical work again suggested a possible effect by Fe³⁺ impurities [8].

At this point, we still have no satisfying explanation for the magnetic field dependence of the low

frequency dielectric properties of glasses or glassy ceramics. Our experiments, however, show clearly that nuclear quadrupole moments can't be the origin of these effects at least in SrTiO₃ ceramics.

- [1] P.W. Anderson, B.I. Halperin, C.M. Varma, *Phil.Mag.* **25**, 1 (1972), W.A. Phillips, *J. Low Temp. Phys.* **7**, 351 (1972).
- [2] P. Strehlow, M. Wohlfahrt, A.G.M. Jansen, R. Haueisen, G. Weiss, C. Enss, S. Hunklinger, *Phys. Rev. Lett.* **84**, 1938 (2000); R. Haueisen, G. Weiss, *Physica B* **316/317**, 555 (2002).
- [3] A. Würger, A. Fleischmann, C. Enss, *Phys. Rev. Lett.* **89**, 237601 (2002).
- [4] S. Ludwig, C. Enss, P. Strehlow, S. Hunklinger, *Phys. Rev. Lett.* **88**, 075501 (2002).
- [5] D. Bodea, A. Würger, *J. Low Temp. Phys.* **136**, 39 (2004).
- [6] K. Kiefer, R. Haueisen, G. Weiss, *J. Low Temp. Phys.* **147**, 517 (2007).
- [7] M. Wohlfahrt, P. Strehlow, C. Enss, S. Hunklinger, *Europhys. Lett.* **56**, 690 (2001).
- [8] A. Borisenko, *J. Phys.: Condens. Matter* **19**, 416102 (2007).

¹ Institut für Werkstoffe der Elektrotechnik, KIT 76128 Karlsruhe

Low frequency acoustic measurements of amorphous $\text{Zr}_{59}\text{Ti}_3\text{Cu}_{20}\text{Ni}_8\text{Al}_{10}$

C. Adler, T. Peichl, U. Kühn¹, G. Weiss

The low temperature thermal and acoustic behavior of glasses, dielectric or metallic, is dominated by two-level systems which can be explained by the tunneling of small groups of atoms between two almost equivalent sites. Specific distributions of the relevant parameters are suggested by the well established tunneling model [1].

Acoustic measurements of various superconducting metallic glasses demonstrate that conduction electrons not only drastically change the dynamics of tunneling systems compared to insulating glasses where only phonons are important but also seem to influence the apparent density of states of the tunneling systems [2, 3]. These early experiments suffered from the fact that metallic glasses were only available as thin splats quenched from the liquid phase. The advent of bulk metallic glasses (BMG) considerably facilitates acoustic experiments and ultrasonic measurements in the 50 MHz range on the glassy alloy $\text{Zr}_{41.2}\text{Ti}_{13.8}\text{Cu}_{12.5}\text{Ni}_{10}\text{Be}_{22.5}$ essentially confirmed the older results [4].

In order to quantify rigorously the influence of conduction electrons on the dynamics and finally on the density of states of the tunneling systems measurements on the same sample are desirable over a wide frequency range. Our experiments on the BMG $\text{Zr}_{59}\text{Ti}_3\text{Cu}_{20}\text{Ni}_8\text{Al}_{10}$ aim in this direction and here we present first results of vibrating reed measurements at frequencies around 1.1 kHz [5]. Another important advantage of this alloy is that it becomes superconducting below 1.3 K which allows to separate electron and phonon effects.

In our experiments, we measured relative changes of sound velocity, deduced from the reed's resonant frequency, and internal friction using a special sample shape and sample holder to minimize uncontrollable losses of the clamping.

In figure 1 the relative changes of the sound velocity with temperature are plotted. At very low temperatures, due to resonant interaction, the tunneling model predicts the sound velocity to increase with temperature [6]. Obviously, this is below the temperature range of our experiment. However, a short rise and a shallow maximum around 75 mK is noticeable. It is followed by a slow decrease which in terms of the tunneling model is due to relaxation processes where the tunneling systems relax via interaction with thermal phonons. Above 200 mK the sound velocity decreases more steeply and then lev-

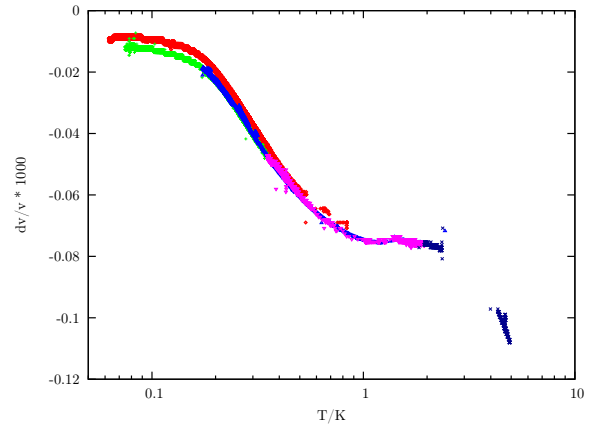


Figure 1: Relative changes of sound velocity at low temperatures, compiled from different measurements. Respective data are identically normalized and thus illustrate the excellent repetitive accuracy across different runs.

els off around 1 K. At the superconducting transition $T_C \approx 1.3$ K (as determined by a susceptibility measurement) we observe a little cusp before the sound velocity decreases rapidly above a few K.

Relaxation of the tunneling systems via interaction with electrons additional to phonons should lead to a faster reduction of the sound velocity above $\approx T_C/2$. However, in contrast to our new and also previous [2, 3] measurements it is predicted that the steepest slope is right below T_C and a kink to a considerably smaller or even positive slope should occur at T_C due to the rapidly closing energy gap at the transition from the superconducting to the normal conducting state [2, 7]. The discrepancy between this prediction and the experiment is not yet fully understood. Kagan and Prokof'ev [8] offered a possible explanation by introducing a modified density of states of the tunneling systems and including renormalization effects due to the interaction with electrons. However, to date their idea has not been evaluated numerically far enough to prove its correctness.

Figure 2 shows the internal friction at low temperatures. In general, the behavior of the internal friction is consistent with earlier experiments [2, 3] and in fact quite similar to a previous measurement of another multi-component Zr based, however splat cooled, glassy metal $\text{Zr}_{65}\text{Al}_{7.5}\text{Cu}_{27.5}$ [9]. From the lowest measured temperatures to 200 mK internal

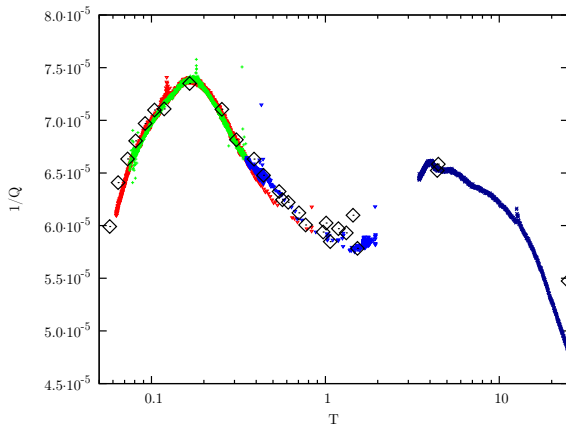


Figure 2: Internal friction versus temperature. Data stem from frequency sweeps at fixed temperatures and evaluation of the resonance curves of the reed (diamonds) or from tracking changes of the amplitude at the resonance frequency during slow temperature variations.

friction increases and relaxation of the tunneling systems is caused by one-phonon processes. The subsequent maximum can be interpreted as the beginning of a plateau which is predicted by the tunneling model and found in experiments on dielectric glasses [6]. It is explained by the broad distribution of the relevant model parameters. We like to note that in this temperature range the internal friction and the slope of the relative variation of the sound velocity agree quantitatively yielding a numerical value of $C \approx 10^{-4}$ where $C = 2Q^{-1}/\pi$ in the plateau range. C contains the density of states of the tunneling systems and their squared deformation potential. In dielectric glasses C is usually larger by about a factor of 6.

The measured values for both the internal friction and sound velocity confirm the deviations from the tunneling model found by previous measurements. The deviations can be explained by the influence of conducting electrons, which not only drastically change the dynamics of tunneling systems but also seem to influence the apparent density of states of tunneling systems.

The obvious deviation from a plateau found in our measurement demonstrates severe shortcomings of the standard model. The strong reduction of the internal friction above 200 mK coincides with the rapid decrease of the sound velocity. It marks the temperature where thermally excited quasi-particles start to play a role for the dynamics of the tunneling systems but also for their effective density of states. Again, the modifications suggested by Kagan and Prokof'ev [8] offer a semi-quantitative explanation.

Above T_C , around 4 K the internal friction has another maximum. As in other glasses, this is caused by tunneling systems relaxing via multi-phonon-processes or thermal activation. There are, however, remarkable differences: Compared to other glasses, this maximum is much smaller and occurs at considerably lower temperatures. This can only be explained by limiting the density of states of the tunneling systems and, the limit has to be at much lower energies in the BMG $Zr_{59}Ti_3Cu_{20}Ni_8Al_{10}$ than in other, particularly dielectric glasses. There is also a noticeable difference to the splat cooled $Zr_{65}Al_{7.5}Cu_{27.5}$ [9] where the internal friction is overall bigger by almost factor 2 and the high temperature roll off occurs at a higher temperature. These last notes might be related to the largely different cooling rates during solidification of the two chemically similar glasses.

In summary, the measured values and temperature dependencies of both the internal friction and sound velocity of the BMG $Zr_{59}Ti_3Cu_{20}Ni_8Al_{10}$ confirm the deviations from the tunneling model found by previous measurements of other superconducting metallic glasses. The deviations might be explained by the influence of conducting electrons, which not only drastically change the dynamics of tunneling systems but also seem to influence the apparent density of states of tunneling systems.

- [1] P.W. Anderson, B.I. Halperin, C.M. Varma, *Phil.Mag.* **25**, 1 (1972), W.A. Phillips, *J. Low Temp. Phys.* **7**, 351 (1972).
- [2] P. Esquinazi, H.M. Ritter, H. Neckel, G. Weiss, S. Hunklinger, *Z. Phys. B - Cond. Matt.* **64**, 81 (1986).
- [3] F. Lichtenberg, H. Raad, W. Morr, G. Weiss, *Phonons 89*, eds. S. Hunklinger, W. Ludwig, G. Weiss (World Scientific, Singapore, 1990) p.471.
- [4] E.V. Bezuglyi, A.L. Gaiduk, V.D. Fil, S. Zherlitsyn, W.L. Johnson, G. Bruls, B. Lathi, B. Wolf, *Phys. Rev. B* **62**, 6656 (2000)
- [5] Clemens Adler, Diplomarbeit, Universität Karlsruhe, 2009
- [6] see e.g. J. Classen, C. Enss, C. Bechinger, G. Weiss, S. Hunklinger, *Ann. Physik* **3**, 315 (1994).
- [7] J.L. Black, P. Fulde, *Phys. Rev. Lett.* **43**, 453 (1979)
- [8] Yu Kagan, N.V. Prokof'ev, *Solid State Comm.* **65**, 1385 (1988)
- [9] Wolfgang Mohr, Diplomarbeit, Universität Karlsruhe, 2001

¹ Dr. Uta Kühn, Institut für Metallische Werkstoffe, Abt. Metallphysik, Leibniz-Institut für Festkörper- und Werkstofforschung, Dresden

Test of a ultra-high vacuum sub-Kelvin scanning tunneling microscope with high energy resolution

L. Zhang, R. Dehm, W. Wulfhekel

For study of nanoscopic structures, an instrument with high lateral resolution and high energy resolution for electronic states is needed. A usual solution for this requirement is a scanning tunneling microscope (STM) working at cryogenic temperatures. For surface science studies of atomically clean structures, the STM needs to be operated in ultra high vacuum (UHV). Commercially available STMs working in UHV use normally He-bath cryostat and work at 4.2 K. The energy resolution of inelastic scanning tunneling spectroscopy (ISTS) at Temperature T is limited to $5.4 k_B T$ [1] which is only about 1.9 meV at 4.2 K. For studying magnetic excitations of single atoms and molecules we need higher energy resolution. Thus we developed a new type of UHV sub-Kelvin STM that can work at 500 mK using He^3 (930mK using He^4) and has a vibrational level below 300 fm at the STM tip.

The UHV chambers includes a preparation chamber and a cryostat chamber which contains an entirely homebuilt cryostat and the STM-head. The first cooling stage of the cryostat is a bath cryostat of liquid N_2 at 77 K which has a standing time of 105 hours for 20 liters liquid nitrogen. The second cooling stage is a bath liquid He^4 cryostat at 4.2 K which has a standing time of 260 hours for 10 liters liquid helium. The last cooling stage consists of a He^3 Joule-Thomson cryostat in which He^3 gas is injected at >1.5 bar, precooled with heat exchangers to 4.2 K and then further cooled by free expansion through a capillary into the He^3 cryostat. In test experiments of the Joule-Thomson expansion using He^4 , the STM temperature reached 1.1 K during filling the Joule-Thomson cryostat and 930 mK after stopping the Joule-Thomson expansion.

Figure 1 shows the structure of the homebuilt STM head which was designed as small and compact as possible in order to reduce the mechanical vibration. The microscope body is made of copper and copper beryllium. The approach mechanism is based on the design by Pan et al. [2]. A 6 mm piezo tube is used as STM scanner which has a maximum scan range of $2 \mu\text{m} * 2 \mu\text{m}$ and a z-range of 200 nm at voltages of ± 280 V.

The STM is operated by commercial control electronics and software [3]. An analog lock-in amplifier is used for performing scanning tunneling spectroscopy (STS). The STM tip and sample are connected to a commercial preamplifier mounted outside

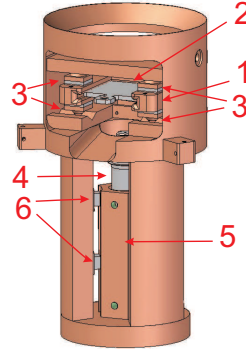


Figure 1: STM-head, 1: sample; 2: sample-holder; 3: piezo for coarse motion in x-direction; 4: tip and scanner; 5: scanner-holder; 6: Piezo for coarse motion in z-direction.

the UHV via shielded twisted-pair cables. To avoid high frequency noise, the STM bias voltage is low-pass filtered with a cutoff frequency of 50 KHz.

We used an in situ prepared Au single crystal to calibrate the STM and to check the mechanical stability. We bombarded the sample with Ar and annealed it at 730 K to get an atomic clean surface. High-quality STM images were obtained on this surface. The x-y calibration of the STM scanner was done by measuring the reconstructions and the z calibration was performed on step edges on the surface. Atomic resolution on a large length scale of Au(111) was achieved at 4.2 K. (see Figure 2). The cross section of this Topography shows an in-line z-noise level of below 1 pm and a between-lines z-noise level of below 5 pm. A main z-noise source in this case is bubbling liquid nitrogen. It could be considerably reduced by letting the liquid nitrogen run out or pumping the nitrogen vapor to let the nitrogen freeze. In case of frozen nitrogen the noise spectrum is below $8 \text{ fA}/\sqrt{\text{Hz}}$ which almost approaches the limit of I-V converter. A topography of Au (111) surface (Figure 3) was taken at 930 mK with an empty LN_2 cryostat. Its line section demonstrates a z-noise of about 200 fm.

For some studies on isolators, semiconductors or magnetic molecules a tunneling current of several nA could damage the sample. Due to the low noise and high mechanical stability this STM is able to investigate these frangible samples with a tunneling current

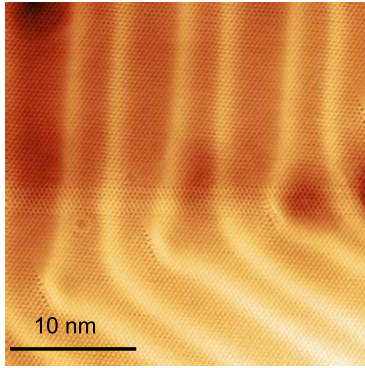


Figure 2: Atomic resolution of Au(111) at 4.2 K.

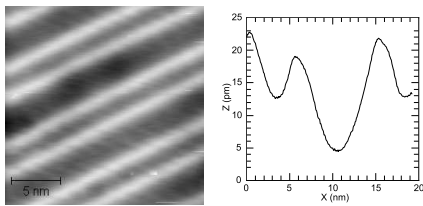


Figure 3: (a) A topography of Au (111); (b) line section of (a) which demonstrates a z-noise of about 200 fm.

of several pA. STM topography of the Au(111) surface at atomic resolution in constant-current mode with a setpoint of 1 pA and a bias of 1 mV is shown in Figure 4.

Due to the design of the cryostat and the high thermal conductance of the STM body, the thermal drift in STM measurements is negligible. Fig 5 shows three STM images of the same single Co atom on Au (111) which were taken at 30 mins, 100 mins and 170 mins after the STM reached 1.1 K. The drift speed was blew 10 pm per hour.

To demonstrate the high energy resolution of our

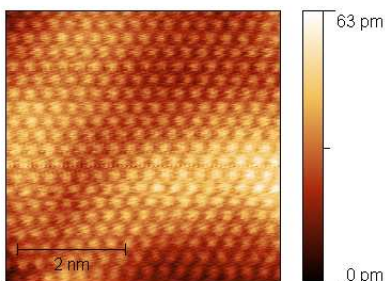


Figure 4: A topography of Au (111) with setpoint of 1 pA and bias of 1 mV.

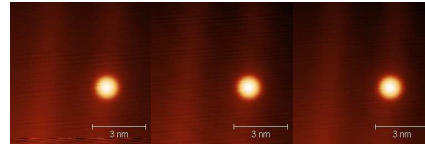


Figure 5: STM images of the same atom demonstrating no observable drift. (a) 30 mins after STM reached 1.1 K; (b) 100 mins after STM reached 1.1 K; (c) 170 mins after STM reached 1.1 K;

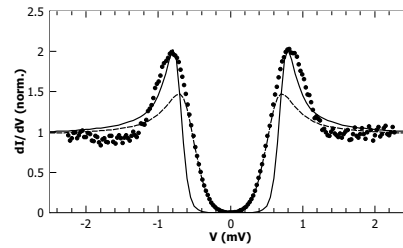


Figure 6: STS of Nb tip on Cu (100). dashed line: fitting curve with a fit temperature of 1.15 K reproducing the energy gap; solid line: fitting curve with a fit temperature of 650 mK reproducing the quasi particle states.

STM we performed STS measurements on in situ prepared Cu (100) using a superconducting Nb tip that has a superconducting phase transition at approximately 9.2 K. The Nb tip was etched in a 1:1:1 admixture of HF, H₃PO₃, HNO₃ from Nb wire and was bombarded with Ar and annealed at approx. 1800 K to remove the oxide. Figure 6 shows a dI/dV curve measured at base temperature. Using conventional BCS theory we can fit the superconducting energy gap which is clearly resolved in STS. The curve was fitted by adjusting the energy gap Δ and the Temperature of the Fermi function. The fit result is shown in Fig. 6 with the dashed line revealing a fit temperature of $T_{fit}=1.15$ K which is close to the temperature read from the cernox sensor on the STM head. This result indicated our energy resolution of STS is limited by the thermal limit of $3.4 kT_{fit}=0.34$ meV for dI/dV curves and $5.4 kT_{fit}=0.54$ meV for dI²/d²V curves.

Due to the good performance of the cryostat and the STM, the design of the machine has been licensed to industrial partners and is already on the market.

- [1] J. Klein *et al.*, Phys. Rev. B **7**, 2336 (1973)
- [2] S. H. Pan *et al.*, Bull. Am. Phys. Soc. **37**, 167 (1992)
- [3] Specs GmbH, www.specs-zurich.com

Imaging the resistive states in thin NbN narrow strips using a low temperature laser scanning microscope

A.Lukashenko, A.Zhuravel¹, K.И'ин², M.Siegel² and A.V.Ustinov

In many applications of weak superconductivity, structures made of narrow thin superconducting films represent the most frequently used device layout. One of the most sensitive radiation sensors is a superconducting single photon detector (SSPD) [1 – 4]. The response of such detectors is based on radiation induced heating of electrons. The mechanism of the response is the current assisted creation of a normal conducting hot spot due to absorption of an energy quantum. To reach the ultimate sensitivity of these devices, it is necessary to use ultra-thin superconducting films.

Homogeneous distribution of the supercurrent density over the strip cross-section is an important factor for the detector operation. It can be achieved in the absence of magnetic vortices for narrow strips with the width $W \ll \lambda$, where λ is the magnetic field penetration depth. Abrikosov vortices cannot enter the superconducting strip less than 4.4ξ in width (ξ is the coherence length) [5]. Particularly, SSPDs made from niobium nitride thin films (which is actually the most popular material for such detectors), should be narrower than 50 nm in order to exclude nucleation of vortices.

A typical operation regime for SSPDs is when the device is biased by the direct current close to the critical current value. The homogeneity of the critical current distribution along the strip also plays a very important role. Information about the spatial distribution of the local superconducting parameters over the sample helps to improve the thin film technology and increase SSPD sensitivity.

In order to visualize the resistive states in thin NbN narrow strips we used a home-built low temperature laser scanning microscope (LSM) [6].

The principle of low temperature LSM technique is similar to that of low temperature scanning electron microscopy (LTSEM) [7] and based on mapping a sample voltage response as a function of the position of a focused laser beam (or electron beam, in case of LTSEM) on its surface. The LSM method requires a much simpler experimental setup than LTSEM, offers similar or better spatial resolution (of the order of $1\ \mu\text{m}$), generates less electromagnetic interference, and is inherently insensitive to magnetic fields. The major effect of the laser beam on the sample during LSM imaging is local heating (bolometric response). There is also an additional (nonbolometric) contribution to the LSM response. In this case the light di-

rectly breaks Cooper pairs, creating nonequilibrium quasiparticles. The spatial resolution of the bolometric response is limited by the thermal healing length. The signal-to-noise ratios are greatly enhanced by modulating the power of the laser at some relatively low frequency f (typically, between 1 and 100 kHz) and measuring the response by a lock-in amplifier. The NbN films were deposited onto sapphire substrates, their thickness d was varied in the range from 4 to 10 nm.

Visualization of the resistive states and measurements of $R(T)$ and IV curves of the samples were performed in an optical cryostat by four-probe method. Figure 1 demonstrates $R(T)$ dependence of NbN sample 208a-7 which is a thin film strip $30\ \mu\text{m}$ in length and $0.4\ \mu\text{m}$ in width.

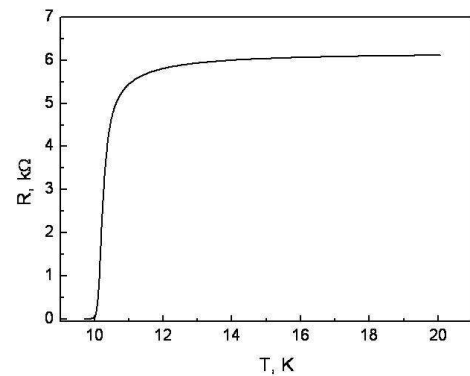


Figure 1: $R(T)$ dependence of sample 208a-7.

Typical $I - V$ curves at different temperatures are shown on the Fig. 2.

Every sample was cooled down below its critical temperature and biased at a dc current $I_{\text{bias}} \geq I_c$. Keeping the bias current fixed, we scanned the sample surface by a focused laser beam (beam spot is about $1\ \mu\text{m}$ in diameter) and measured the resulting voltage δV change across the sample as a function of the laser beam coordinates. In order to decrease noise and improve spatial resolution we used a lock-in technique. Figure 2 shows that with decreasing of temperature the $I - V$ curves become hysteretic. To visualize the resistive states of the samples we maintained the temperature in the range between 8 K and 10 K.

LSM image obtained by measuring the intensity

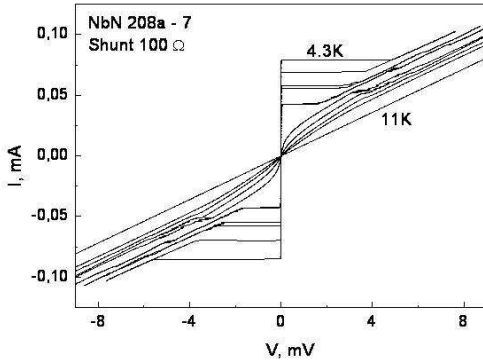


Figure 2: Series of I-V curves of the sample 208a-7 taken in the temperature range 4.3K - 11K.

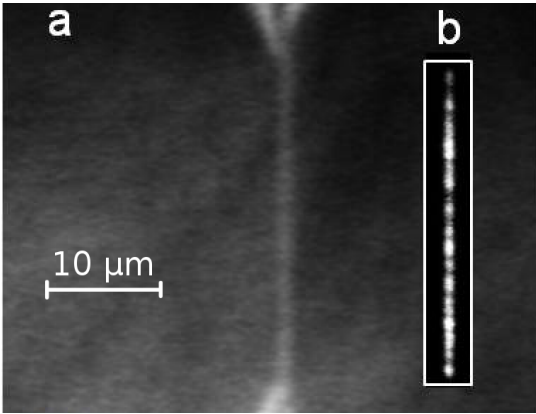


Figure 3: a) Optical LSM image of the sample 208a-7. The width of the stripe is $0.4 \mu\text{m}$, the length of the sample between the voltage pads is $30 \mu\text{m}$. Thickness of NbN film is 4 nm . b) Voltage response of the sample measured in the resistive state

of laser light reflected from the surface of one of the samples is shown in Fig.3a. Figure 3b demonstrates a voltage response of the sample measured in the resistive state at bias current $I_b = 60 \mu\text{A}$, $T = 8.5 \text{ K}$, laser power $W = 7 \mu\text{W}$, modulation frequency of the laser beam 94 kHz .

Black areas on the Fig. 3b correspond to the lower voltage response δV and white ones correspond to higher voltage response. As one can see from the Fig. 3b, the spatial distribution of the voltage response along the length of the sample is not homogeneous. In other words, the local superconducting properties of the sample (critical current and/or critical temperature) have different values at different locations.

To measure the local values of the critical current we stabilize the temperature at some value below T_c , where the $I - V$ curve is not hysteretic. Then we focus a laser beam at a certain point on the sample surface, increase bias current and measure the voltage response. After this we shift a laser beam to another position and repeat the measurements. In such a way, we can determine the moments when the response appears and measure the spatial distribution of the critical current I_c .

Two curves $\delta V(I_b)$ in Fig.4a are related to two different positions of the laser beam. The locations where the measurements were done are shown by two arrows on a Fig.3b. Difference in I_c in this case is $5 \mu\text{A}$, which corresponds to about 8% of mean I_c for this particular sample.

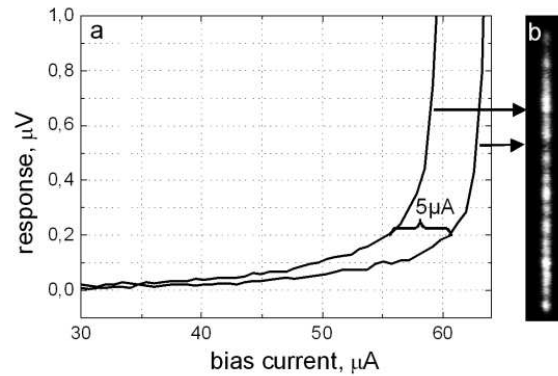


Figure 4: $\delta V(I_b)$ dependence for the sample 208a-7 measured at two different positions of the laser beam. b) Voltage response of the sample at $I_b = 60 \mu\text{A}$.

- [1] N.K.Sherman, Phys.Rev.Lett. **8**, 438, (1962).
- [2] A.D.Semenov et al., Physica C **351**, 349, (2001).
- [3] G.Gol'tsman et al., Appl.Phys.Lett., **79**, 705, (2001).
- [4] A.Semenov et al., Eur.Phys.J., **B47**, 495, (2005).
- [5] K.K.Likharev, Rev.Mod.Phys. **51**, 101, (1979).
- [6] D.Abraimov et al., Appl. Phys. Lett. **85**, 2568, (2004).
- [7] R.Gross, D.Koelle, Rep. Prog. Phys. **57**, 651, (1994).
- [8] K.П'ин et al., J. Low.Temp.Phys. **151**, 585, (2008)

¹ B. Verkin Institute for Low Temperature Physics & Engineering, Kharkov Ukraine ² Institut für Mikro- und Nanoelektronische Systeme, KIT, Karlsruhe, Germany

Photon count imaging of NbN single photon detectors

P. Jung, A. Lukashenko, A. Zhuravel¹, M. Hofherr², S. Wünsch², K. Ilin², M. Siegel², and A. V. Ustinov

Superconducting Nanowire Single Photon Detectors (SNSPD) have been extensively studied throughout the past years. Since most of these studies did not explicitly investigate the spacial properties of the detectors, our goal here was to employ the *laser scanning microscope (LSM)* to measure spatial uniformity of the *detection efficiency*. Information gained from such experiments can then in turn be used to improve the detector (i.e. by modifying it's geometry) and, moreover, to get an insight into the basic mechanism of optical photon absorption.

The studied devices are thin (approx. 5 nm) NbN

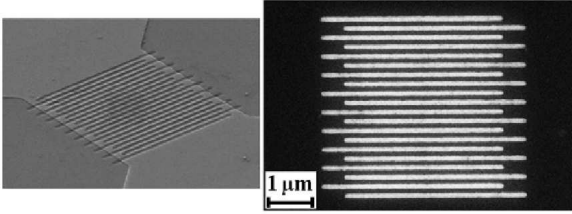


Figure 1: SEM (left) and TEM (right) images of a detector [1]

films which are e-beam patterned into a $4 \times 4 \mu\text{m}$ meander structure. The lines are typically about 100 nm wide, see Fig. 1.

When biased at a current close to their critical

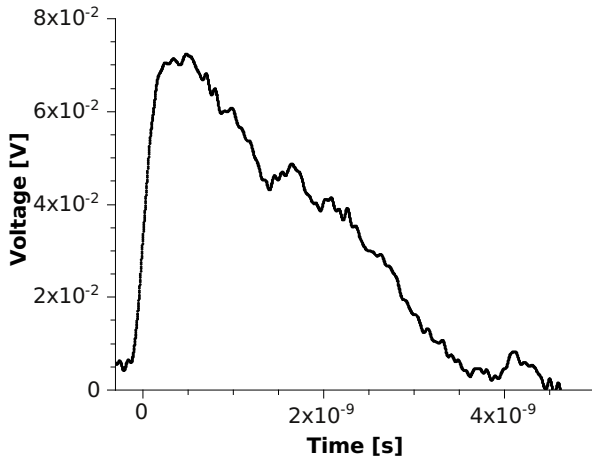


Figure 2: Profile of a dark counted pulse at $I_b = 0.75I_c$

current, these structures are sensitive to incident optical photons. Photon absorption leads to a small reduction in the number of Cooper pairs, which is enough to locally suppress superconductivity. If the energy of the incoming photon is high enough (this is typically true for photons with $\lambda < 1000 \text{ nm}$) it can break some Cooper pairs and thereby create a normal conducting region. The behaviour of this normal zone is then governed by the current driven through the sample. The current in turn is controlled by the resistance of the normal zone, the inductance of the sample and the bias current. The typical temporal evolution of the zone is to extend along the line up to a maximum, then shrink, and finally vanish, all this in less than a nanosecond. To understand the electrical response of the system, we follow the simplified approach, that the detector can be electronically modeled as an inductance (corresponding to the meander's kinetic inductance) and a time dependent resistor. The output of the system is a voltage pulse that is typically few nanoseconds long (Fig. 2). Apart from high energy photons such pulses can also be triggered by less energetic photons [4] (but with a lower probability), as well as by thermodynamic fluctuations or current noise [2]. These non-photon induced pulses are commonly referred to as dark counts. Their count rates, and therefore the ratio of dark counts to photon counts are strongly dependent on the bias current (see Fig. 3).

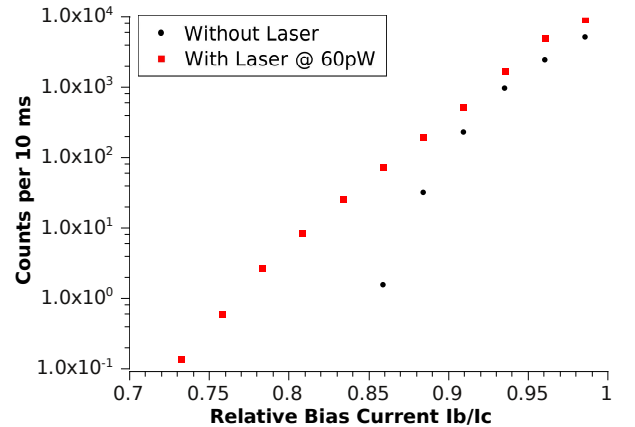


Figure 3: Dependence of the maximum measured count rate versus the reduced bias current.

In our experiment, the detector is embedded in a readout circuit (Fig. 4) consisting of a shunting resistor R_0 and a bias-tee used to decouple the dc bias line from the high frequency line. The sample is placed inside a 4.2 K optical cryostat. The voltage pulse is transferred through the RF-path of the bias-tee and amplified with a series of room temperature amplifiers. The resulting output can then be investigated using an oscilloscope or sent to a pulse counter which counts the number of pulses over a set time. The detector itself is situated below an optical window in the cryostat through which a $\lambda = 655$ nm laser is focused onto the sample plane. The coordinates of the focused spot can be controlled through two positioning mirrors.

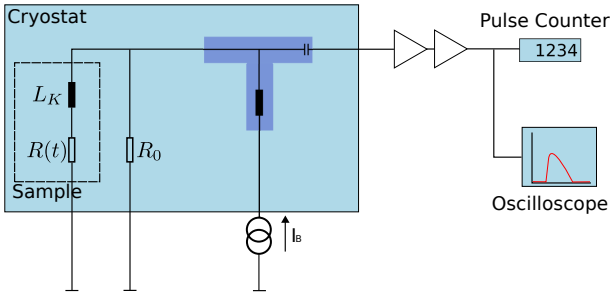


Figure 4: Schematics of the electrical part of the experiment. The sample is modeled as an inductance in series with a resistance dependent on the current state of the detector.

To achieve optimal conditions for single photon counting we had to shield the optical window against residual light. The low detection efficiency for infrared photons was very helpful in this case since it reduced our efforts to visual (higher energy) light. The laser beam power had to be high enough to provide a decent contrast against the dark counts but as low as possible to reduce the bolometric effects. Using this technique we were able to acquire images of the count rate over the position of the laser beam. (Fig. 5). The sample response appears here as rather uniform. These images represent a convolution of the actual spatial response of the detector and the well known *point spread function* of the laser beam. Although the deconvolution is possible, some information is lost due to the pixel quantization and image borders. The existing deconvolution algorithms tend to produce rather limited results. Despite the limited spatial resolution, which is about

$1\ \mu\text{m}$, our technique is well suited to identify weak areas on the detector such as constrictions. To extract more physical information, it is essential to improve the spatial resolution of the microscope or resort to larger or specially designed samples.

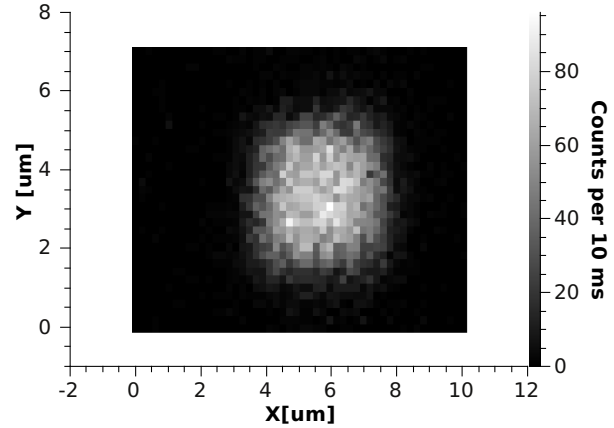


Figure 5: Response map of a $4 \times 4\ \mu\text{m}$ detector scanned with a step size of 200 nm and biased at $I_b = 0.88I_c$. The gray scale represents the number of pulses per 10ms. Meander lines extend from top to bottom while the scanning direction is from left to right.

The detector we investigated so far did not show any obvious signs of defects. The results suggest that there is some influence of the geometrical features (i.e. the bends) which need to be investigated more closely. The maximum measured detection efficiency is about 1-2%, which is comparable to previous results. We note, however, that this number is well below the calculated values for NbN meanders of this geometry [3].

- [1] A. Semenov et al., Supercond. Sci. Technol. **20**, 919 (2007)
- [2] A. Engel et al., phys. stat. sol. (c) **2**, No. 5, 1668 (2005)
- [3] A. Semenov et al., J. of Mod. Optics **56**, 345 (2009)
- [4] A. Semenov et al., Physica C **468**, 627 (2008)

¹ B. Verkin Institute for Low Temperature Physics & Engineering, Kharkov Ukraine ² Institut für Mikro- und Nanoelektronische Systeme, KIT, Karlsruhe, Germany

Diploma theses

Adler, Clemens	Niederfrequente akustische Messungen an amorphem $\text{Zr}_{59}\text{Ti}_3\text{Cu}_{20}\text{Ni}_8\text{Al}_{10}$
Aslan, Ferhat	Dielektrische Eigenschaften von $^{88}\text{Sr}^{48}\text{TiO}_3$ bei tiefen Temperaturen
Berg, Oliver	Punktkontaktspektroskopie an undotiertem und dotiertem BaFe_2As_2
Bögle, Rainer	Korrektur von suszeptibilitätsverursachten geometrischen Verzerrungen in der Echtzeit bewegungskorrigierten fMRT
Bork, Annika	Ladungs- und Spintransport durch einzelne Moleküle
Gerstl, Stefan	Magnetische Anregungen von Gadoliniumatomen auf Pt(111)- und Cu(111)-Oberflächen
Hundermark, Axel	Electron transport across silicon nanocrystals
Wolf, Michael	Spezifische Wärme und magnetokalorischer Effekt am magnetfeldinduzierten Quantenphasenübergang in $\text{CeCu}_{5.7}\text{Au}_{0.3}$

Doctoral dissertations

Arac, Erhan	Magnetic anisotropy and magnetic after-effect in ferromagnetic strained LaCoO_3 thin films
Bagrets, Nadezda	Pressure and concentration tuning of magnetic order in the heavy-fermion systems $\text{CePt}_{1-x}\text{Ni}_x$ and $\text{CePd}_{1-x}\text{Ni}_x\text{Al}$
Balashov, Timofey	Inelastic scanning tunneling spectroscopy: magnetic excitations on the nanoscale
Brauer, Jacob	Lokaler und nichtlokaler Transport in Normalleiter-Supraleiter-Heterostrukturen
Drotziger, Sandra	Korrelierte Elektronensysteme unter hohem Druck: itineranter Ferromagnetismus in CoSi_2 und Supraleitung in $\text{Ba}(\text{Fe}_{1-x}\text{Co}_x)_2\text{As}_2$
Marquardt, Christoph W.	Elektrolumineszenz organischer Moleküle nach Kontaktierung mit Kohlenstoff-Nanoröhren
Marz, Michael	Spektroskopische Untersuchungen an Supraleitern mittels Punktkontaktspektroskopie und Rastertunnelmikroskopie
Sauter, Markus	Untersuchungen eindimensionaler Strukturen auf vizinalen Si(111): Au-Oberflächen mit Rastertunnelmikroskopie und -spektroskopie

Long-term guests

T. Golikova, Institute of Solid State Physics, Chernogolovka, Russia	22.08.2009 - 23.10.2009 and 07.12.2009 - 23.12.2009	DFG
M. Gorodilin, cole Centrale Paris, France	16.06.2009 - 31.08.2009	SCOPE
A. Nateprov, Institute of Applied Physics, Kishinev Moldova	04.05.2009 - 03.08.2009	DFG
A. Shcherbakova, Ioffe Physical-Technical Institute, St. Petersburg, Russia	21.09.2009 - 20.12.2009	DFG
S. Suga, Osaka University, Japan	12.03.2009 - 21.09.2009	JSPS / A. v. Humboldt-Stiftung
A. P. Zhuravel, B. Verkin, Institute for Low Temperature Physics and Engineering, Ukraine	01.02.2009 - 30.04.2009 and 26.09.2009 - 17.10.2009	BMBF

Teaching activities

Summer term 2009

Prof. Dr. A. Ustinov	Lecture	Physik II (Elektrodynamik)
Prof. Dr. A. Ustinov, Dr. G. Fischer	Tutorial	Physik II
Prof. Dr. W. Wulfhekel, Dr. T. Yamada	Lecture	Oberflächenphysik
Prof. Dr. W. Wulfhekel, Dr. R. Hoffmann-Vogel	Tutorial	Oberflächenphysik
Prof. Dr. C. Klingshirn, Dr. C. Sürgers	Lab course	Physikalisches Fortgeschrittenen Praktikum

Prof. Dr. A. Ustinov, Dr. H.-J. Simonis	Lab course	Physikalisches Anfängerpraktikum für Chemiker, Bio- und Geowissenschaftler und Technomathematiker
Prof. Dr. W. Wulfhekel, Dr. H.-J. Simonis	Lab course	Physikalisches Anfängerpraktikum für Chemieingenieure, Verfahrenstechniker, Bioingenieure und Wirtschaftsingenieure
Prof. Dr. A. Ustinov, Dr. J. Lisenfeld, Dr. A. Lukashenko, Dr. S. Poletto	Seminar	Hauptseminar: Superconductivity
Prof. Dr. H. v. Löhneysen, apl. Prof. Dr. B. Pilawa, Dr. D. Beckmann, Dr. V. Fritsch	Seminar	Hauptseminar: Magnetismus
Prof. Dr. H. v. Löhneysen, Prof. Dr. A. Ustinov, Prof. Dr. G. Weiß, Prof. Dr. W. Wulfhekel	Seminar	Institutsseminar
Prof. Dr. H. v. Löhneysen, Prof. Dr. G. Weiß, Prof. Dr. A. Ustinov, Prof. Dr. W. Wulfhekel, Dr. K.-P. Bohnen	Seminar	Gemeinsames Seminar Universität/Forschungszentrum über Festkörperphysik
Prof. Dr. H. v. Löhneysen	Seminar	Seminar über aktuelle Fragen der Festkörperphysik
apl. Prof. Dr. G. Goll	Seminar	Seminar über aktuelle Arbeiten
Prof. Dr. A. Ustinov	Seminar	Seminar on Quantum Circuits
Prof. Dr. W. Wulfhekel	Seminar	Seminar zur Oberflächenphysik

Winter term 2009/10

Prof. Dr. A. Ustinov	Lecture	Physik V (Festkörperphysik)
Prof. Dr. A. Ustinov, Dr. G. Fischer	Tutorial	Physik V
Prof. Dr. W. Wulfhekel	Lecture	Elektronische Eigenschaften von Festkörpern I
Prof. Dr. W. Wulfhekel, Dr. R. Hoffmann-Vogel	Tutorial	Elektronische Eigenschaften von Festkörpern I
apl. Prof. Dr. G. Goll	Lecture	Modern physics (KSOP)

apl. Prof. Dr. G. Goll, Dr. V. Fritsch	Tutorial	Modern physics (KSOP)
Prof. Dr. C. Klingshirn, Dr. C. Sürgers	Lab course	Physikalisches Fortgeschrittenen Praktikum
Prof. Dr. A. Ustinov, Dr. F. Hartmann	Lab course	Physikalisches Anfängerpraktikum für Chemiker, Bio- und Geowissenschaftler und Technomathematiker
Prof. Dr. W. Wulfhekel, Prof. Dr. G. Weiß, Dr. M. Lukas, Dr. T. Yamada	Seminar	Hauptseminar: Rastersondenmethoden
Prof. Dr. A. Ustinov, Dr. P. Bushev, Dr. R. Danneau, Dr. H. Rotzinger	Seminar	Hauptseminar: Physics of Noise
Prof. Dr. H. v. Löhneysen, Prof. Dr. A. Ustinov, Prof. Dr. G. Weiß, Prof. Dr. W. Wulfhekel	Seminar	Institutsseminar
Prof. Dr. H. v. Löhneysen, Prof. Dr. G. Weiß, Prof. Dr. A. Ustinov, Prof. Dr. W. Wulfhekel, Dr. K.-P. Bohnen	Seminar	Gemeinsames Seminar im KIT von Physikalischem Institut und Institut für Festkörperphysik über Festkörperphysik
Prof. Dr. H. v. Löhneysen	Seminar	Seminar über aktuelle Fragen der Festkörperphysik
apl. Prof. Dr. G. Goll	Seminar	Seminar über aktuelle Arbeiten
Prof. Dr. A. Ustinov	Seminar	Seminar on Quantum Circuits
Prof. Dr. G. Weiß	Seminar	Seminar über Fragen der Festkörperphysik
Prof. Dr. W. Wulfhekel	Seminar	Seminar zur Oberflächenphysik

Seminar talks at Physikalisches Institut

12.01.2009	R. Danneau	Shot noise in graphene: from large strips to nanoribbons
19.01.2009*	W. Cui	Fabrication and measurement of single charge devices in the normal and superconducting regime
26.01.2009	H. P. Oepen	Investigation of the magnetic structure in ferromagnetic thin film systems
02.02.2009*	E. Arac	Magneto-elastic coupling and magnetic reversal in LaCoO_3 thin films
09.02.2009	K. Hasselbach	Vortex coalescence, vortex chains and crossing vortices in the anisotropic spin-triplet superconductor Sr_2RuO_4
18.03.2009	S. Singh	Studies on interface magnetic moments in multilayer samples by neutron and x-ray reflectometry
20.04.2009*	J. Brauer	Experimental investigation of nonlocal electronic transport in superconducting heterostructures
27.04.2009	B. Koslowski	Scanning tunneling spectroscopy: Towards a quantitative analysis and deconvolution of the density of states of tip and sample
04.05.2009*	A. Soon	Understanding surface nanostructures on metal surfaces: An ab initio thermodynamics approach
11.05.2009	V. Geshkenbein	Münchhausen effect: Tunneling in an asymmetric SQUID
18.05.2009*	R. Eder	Photoelectron spectra of transition metal oxides
25.05.2009	M. Marz	Point-contact spectroscopy on 122 iron pnictide superconductors
08.06.2009	H. B. Weber	Electron transport in epitaxially grown graphene
15.06.2009*	N. Bagrets	Quantum criticality in $\text{CeNi}_x\text{Pt}_{1-x}$ and $\text{CePd}_{1-x}\text{Ni}_x\text{Al}$ heavy fermion systems
17.06.2009	S. Suga	Photoelectron spectroscopy from 8 eV to 8 keV: Kondo resonance, surface-bulk problem, 3D bulk fermiology and nucleus recoil effects on photoelectron emission
22.06.2009	J. Fransson	Detection of spin moments and spin inelastic electron tunneling spectroscopy using spin-polarized scanning tunneling microscope
29.06.2009*	S. Drotziger	Pressure dependent magnetization measurements on CoS_2 and on $\text{Ba}(\text{Fe}_{1-x}\text{Co}_x)_2\text{As}_2$
06.07.2009	M. Morgenstern	Scanning tunneling spectroscopy at low temperature: Electron systems and oscillating graphene

13.07.2009*	C. Marquardt	Molecule nanotube hybrides
20.07.2009	S. Lenhart	Bottom up surface structuring by dip-pen nanolithography
19.10.2009*	A. V. Kimel	Femtosecond magneto-optics and opto-magnetism
26.10.2009	L. Ozyuzer	Terahertz wave emission from intrinsic Josephson junctions of high- T_c superconductors
02.11.2009*	U. Stockert	Towards Ettingshausen refrigeration: The Nernst effect in CeNiSn
09.11.2009	A. Kemp	Entanglement of a superconducting flux qubit with a harmonic resonator and two level fluctuators
16.11.2009*	M. Przybylski	Oscillatory magnetic anisotropy originating from quantum well states in Fe films
23.11.2009	K. Arutyunov	Quantum tunneling in superconducting nanowires
30.11.2009*	H. van Kempen	Cold focused beams of conduction electrons
07.12.2009	S. Frolov	Spin interactions in nanowire few electron quantum dots
14.12.2009*	F. Lefloch	Current noise measurements in hybrid superconducting nanostructures
21.12.2009	P. Fusik	Arbeitssicherheit

* Gemeinsames Seminar über Festkörperphysik von Universität und Forschungszentrum

Publications

- T. Balashov, T. Schuh, A. F. Takacs, A. Ernst, S. Ostanin, J. Henk, I. Mertig, P. Bruno, T. Miyamachi, S. Suga, W. Wulfhekel
Magnetic Anisotropy and Magnetization Dynamics of Individual Atoms and Clusters of Fe and Co on Pt(111), Phys. Rev. Lett. **102** (2009) 257203
- V. Fritsch and H. v. Löhneysen
Magnetic order of CeNi_xGa_{4-x}, J. Phys.: Conf. Ser. **150** (2009) 042033
- D. Fuchs, L. Dieterle, E. Arac, R. Eder, P. Adelman, V. Eyert, T. Kopp, R. Schneider, D. Gerthsen, H. v. Löhneysen
Suppression of the ferromagnetic state in LaCoO₃ films by rhombohedral distortion, Phys. Rev. B **79** (2009) 024424, 1-9
- F. Hardy, P. Adelman, T. Wolf, H. v. Löhneysen, C. Meingast
Large anisotropic uniaxial pressure dependencies of T_c in single crystalline Ba(Fe_{0.92}Co_{0.08})₂As₂, Phys. Rev. Lett. **102** (2009) 187004, 1-4
- F. Hardy, C. Meingast, V. Taufour, J. Flouquet, H. v. Löhneysen, R. A. Fisher, N. E. Phillips, A. Huxley, J. C. Lashley
Two magnetic Grüneisen parameters in the ferromagnetic superconductor UGe₂, Phys. Rev. B **80** (2009) 174521
- T. Irisawa, T. K. Yamada and T. Mizoguchi
Spin polarization vectors of field emitted electrons from Fe/W tips, N. J. Phys. **11** (2009) 113031
- Ch. Kaiser, G. Weiss, T. W. Cornelius, M. E. Toimil-Molaes and R. Neumann
Low temperature magnetoresistance measurements on bismuth nanowire arrays, J. Phys.: Condens. Matter **21** (2009) 205301
- M. Klein, J. Kroha, H. v. Löhneysen, O. Stockert, F. Reinert
Echo of the quantum phase transition of CeCu_{6-x}Au_x in XPS: Breakdown of Kondo screening, Phys. Rev. B **79**, (2009) 075111
- W. Knafo, C. Meingast, A. V. Boris, P. Popovich, N. N. Kovaleva, P. Yordanov, A. Maljuk, R. K. Kremer, H. v. Löhneysen, B. Keimer
Ferromagnetism and lattice distortions in the perovskite YTiO₃, Phys. Rev. B **79** (2009) 054431
- W. Knafo, C. Meingast, S. Skarya, N. H. van Dijk, Y.-K. Huang, H. Rakoto, J.-M. Broto, H. v. Löhneysen
Critical scaling of the magnetization and magnetostriction in the weak itinerant ferromagnet UIr, J. Phys. Soc. Jpn. **78** (2009) 043707
- J. Lisenfeld, C. Mueller, J. H. Cole, A. Lukashenko, A. Shnirman and A. V. Ustinov
Rabi spectroscopy of a strongly driven qubit-fluctuator system, (2009) arXiv:0909.3425
- I. Marzoli, P. Tombesi, G. Ciaramicoli, G. Werth, P. Bushev, S. Stahl, F. Schmidt-Kaler, M. Hellwig, C. Henkel, G. Marx, I. Jex, E. Stachowska, G. SzaWiola, A. Walaszyk
Experimental and theoretical challenges for the trapped electron quantum computer, J. Phys. B **42** (2009)154010

- C. Meingast, Q. Zhang, T. Wolf, F. Hardy, K. Grube W. Knafo, P. Adlemann, P. Schweiss, H. v. Löhneysen *Resistivity of $Mn_{1-x}Fe_xSi$ single crystals: Evidence for quantum critical behavior*, Nato Science for Peace and Security Series B (2009) 261-266
- E. Moyen, M. Macé, G. Agnus, A. Fleurence, T. Maroutian, F. Houzé, A. Stupakiewicz, L. Masson, B. Bartelien, W. Wulfhekel, P. Beauvillain, and M. Hanbücken *Metal-rich Au-silicide nanoparticles for use in nanotechnology*, Appl. Phys. Lett. **94** (2009) 233101
- C. Pérez León, C. Sürgers, M. Mayor, M. Marz, R. Hoffmann, H. v. Löhneysen *STM investigation of large π -conjugated oligomers and tetrahydrofuran codeposited on Cu(111) by pulse injection* J. Phys. Chem. C **113** (2009) 14335-14340
- J. Pfeiffer, T. Gaber, D. Koelle, R. Kleiner, E. Goldobin, M. Weides, H. Kohlstedt, J. Lisenfeld, A. K. Feofanov, and A. V. Ustinov *Escape Rate Measurements and Microwave Spectroscopy of 0 , π , and 0 - π ferromagnetic Josephson Tunnel Junctions*, (2009) arXiv:0903.1046
- S. Poletto, F. Chiarello, M. G. Castellano, J. Lisenfeld, A. Lukashenko, C. Cosmelli, G. Torrioli, P. Carelli, and A. V. Ustinov *Coherent oscillations in a superconducting tunable flux qubit manipulated without microwaves*, N. J. Phys. **11**, (2009) 013009 , arXiv:0809.1331
- S. Poletto, F. Chiarello, M. G. Castellano, J. Lisenfeld, A. Lukashenko, P. Carelli, and A. V. Ustinov *A tunable rf SQUID manipulated as flux and phase qubit*, Phys. Scr. T **137** (2009) 014011, arXiv:0910.4562v1
- V. Saxena, A. K. Chauhan, N. Padma, D. K. Aswal, S. P. Koiry, Shashwati Sen, R. B. Tokas, S. K. Gupta, C. Sürgers, J. V. Yakhmi *Poly(3-hexylthiophene) based field effect transistors with gate SiO_2 dielectric modified by multilayers of 3-aminopropyltrichlorosilane*, Thin Sol. Films **517** (2009) 6124
- C. Sürgers, K. Potzger, G. Fischer *Magnetism of carbon doped Mn_5Si_3 and Mn_5Ge_3 films*, J. Chem. Sci. **121** (2009) 173

Scientific and technical staff

Prof. Dr. Hilbert v. Löhneysen

Bagrets, Nadezda, Dr.
 Drotziger, Sandra, Dr.
 Fritsch, Veronika, Dr.
 Hoffmann-Vogel, Regina, Dr.
 Pérez León, Carmen, Dr.
 Sauter, Markus, Dr.
 Berg, Oliver, Dipl.-Phys.
 Hamann, Andreas, Dipl.-Phys.
 Montbrun, Richard, Dipl.-Phys.
 Müller, Marc, Dipl.-Phys.
 Stöffler, Dominik, Dipl.-Phys.
 Tomanic, Tihomir, Dipl.-Phys.
 Wolf, Michael, Dipl.-Phys.
 Zaum, Sebastian, Dipl.-Phys.
 Kittler, Wolfram, cand. phys.

Prof. Dr. Alexey Ustinov

Buschev, Pavel, Dr.
 He, Ming, Dr.
 Lisenfeld, Jürgen, Dr.
 Lukashenko, Oleksandre, Dr.
 Poletto, Stefano, Dr.
 Rotzinger, Hannes, Dr.
 Fedorov, Kirill, Dipl.-Phys.
 Feofanov, Alexey, Dipl.-Phys.
 Jerger, Markus, Dipl.-Phys.
 Wirth, Tobias, Dipl.-Phys.
 Zimmer, Jochen, Dipl.-Phys.
 Butz, Susanne, cand. phys.
 Dörling, Bernhard, cand. phys.
 Grabovskij, Grigorij, cand. phys.
 Jung, Philipp, cand. phys.
 Schwemmer, Christian, cand. phys.
 Skwierwaski, Piotr, cand. phys.

Prof. Dr. Georg Weiß

Adler, Clemens, Dipl.-Phys.
 Aslan, Ferhat, Dipl.-Phys.
 Peichl, Torben, Dipl.-Phys.
 Wirner, Frank, Dipl.-Phys.

Prof. Dr. Wulf Wulfhekel

Balashov, Timofey, Dr.
 Miyamachi, Toshio, Dr.
 Nahas, Yasmine, Dr.
 Yamada, Toyo Kazu, Dr.

Bork, Annika, Dipl.-Phys.
 Gerstl, Stefan, Dipl.-Phys.
 Schmaus, Stefan, Dipl.-Phys.
 Schuh, Tobias, Dipl.-Phys.
 Gerhard, Lukas, cand. phys.
 Holzberger, Simon, cand. phys.
 Kramczynski, Detlef, cand. phys.
 Schackert, Michael, cand. phys.
 Vu Chi, Dung, cand. phys.
 Zeier, Klaus, cand. phys.
 Zhang, Lei, cand. phys.

apl. Prof. Dr. Bernd Pilawa

apl. Prof. Dr. Gernot Goll

Marz, Michael, Dr.
 Bouvron, Samuel, Dipl.-Phys.

Permanent scientific staff

Fischer, Gerda, Dr., Akad. Oberrätin
 Sürgers, Christoph, Dr., Akad. Oberrat

Professors emeriti

Dormann, Elmar, Prof. Dr.
 Hasse, Jörg, Prof. Dr.

Secretary

Baatz, Steffi
 Schelske, Birgit

Technical support

Aydin, Orhan, technician
 Behrens, Lars, computer assistance
 Hügler, Cornelia, sample preparation
 Odenwald, Ilse, crystal growth

Helium liquifier

Hartlieb, Franz

Electronics workshop

Jehle, Roland
 Opfer, Ulrich
 Opolony, Christine

Mechanical workshop

Binkert, Erwin
Dehm, Reinhold
Fey, Heinzpeter
Giesinger, Willi
Hummel, Marco
Knecht, Stefan
Masur, Jessica
Pech, Martin
Rose, Jens
Sacan, Daniel
Seringer, Steffen
Zink, Bernhard

Apprentice machinist workshop

Barner, Björn
Greif, Janek
Hergt, David
Schöffel, Patrick
Kalugin, Michael
Schindele, Fabian
Schmidt, Dustin
Weinmann, Tobias

Cover design: C. Sürgers

